Precipitation Strengthening of Aluminum by Transition Metal Aluminides

by

Yangyang Fan

A Dissertation

Submitted to the Faculty

of the

WORCESTER POLYTECHNIC INSTITUTE

in partial fulfillment of the requirements for the

Degree of Doctor of Philosophy

in

Materials Science and Engineering

April, 2015

APPROVED:

_____

Professor Makhlouf M. Makhlouf, Advisor
Director of Advanced Casting Research Center

_____

George F. Fuller Professor Richard D. Sisson Jr.,
Director of Manufacturing and Materials Engineering

Abstract

A castable alloy, i.e., one that flows easily to fill the entire mold cavity and also has resistance to hot tearing during solidification, must invariably contain a sufficient amount of a eutectic structure. For this reason, most traditional aluminum casting alloys contain silicon because the aluminum-silicon eutectic imparts to the alloy excellent casting characteristics. However, the solidus temperature in the Al-Si system does not exceed 577°C, and the major alloying elements (i.e., zinc, magnesium, and copper) used with silicon in these alloys further lower the solidus temperature. Also, these elements have high diffusivity in aluminum and so, while they enhance the room temperature strength of the alloy, they are not useful at elevated temperatures. Considering nickel-base super alloys, whose mechanical properties are retained up to temperatures that approach 75% of their melting point, it is conceivable that castable aluminum alloys can be developed on the same basis so that they are useful at temperatures approaching 350°C.

A castable aluminum alloy intended for high temperature applications must contain a eutectic structure that is stable at temperatures higher than 600°C, and must contain second phase precipitate particles that are thermodynamically stable at the service temperature. Transition metal trialuminides with the general chemical formula Al_xTM_y in which TM is

a transition metal, are excellent candidates for both the eutectic structure and the precipitate particles. In this research, the use of transition metals in the constitution of aluminum casting alloys is investigated with emphasis on the morphology, crystallography, and mechanisms of formation of the various phases.

ACKNOWLEDGEMENTS

First of all a most gratitude is dedicated to my advisor, teacher, mentor, and friend Prof. Makhlouf M. Makhlouf, not only for his knowledgeable instructions but also for his sustained encouragement throughout my studies in WPI.

I would like to extend my deepest gratitude to the department head Prof. Richard D. Sisson, and director of MPI Prof. Diran Apelian. You are always helpful and willing to give chance to the young people.

Very special thanks to Dr. Libo Wang and Dr. Lance Wu who taught me about casting techniques; Dr. Boquan Li who shared his knowledge about transmission microscopy with me; Mr. Adam Graham in Harvard University who helped me solve numerous problems on TEM.

I would also like to thank to my "tea party group". Without your companion every afternoon, it would be what a boring journey.

Last and most importantly, I would like to dedicate this dissertation to my parents. Without your selfless help, I will never finish this journey.

Table of Contents

Chapter 1

Introduction

BACKGROUND

Considering nickel-base superalloys, whose mechanical properties are retained up to temperatures that approach 75% of their melting point, it is conceivable that castable aluminum alloys can be developed on the same basis so that they are useful at temperatures approaching 350°C. Most of the traditional aluminum casting alloys are based on the aluminum-silicon eutectic system because of its excellent casting characteristics, including good fluidity and resistance to hot tearing. Unfortunately, the solidus in this system does not exceed 577°C and so it cannot be part of an alloy intended for high temperature applications. Moreover, the major alloying elements in traditional aluminum casting alloys (i.e., zinc, magnesium, and copper) have high diffusivity in the aluminum solid solution. Therefore, while these elements enhance the room temperature strength of the alloy, they compromise its thermal stability. A castable aluminum alloy intended for high temperature applications must contain a eutectic structure that is stable at

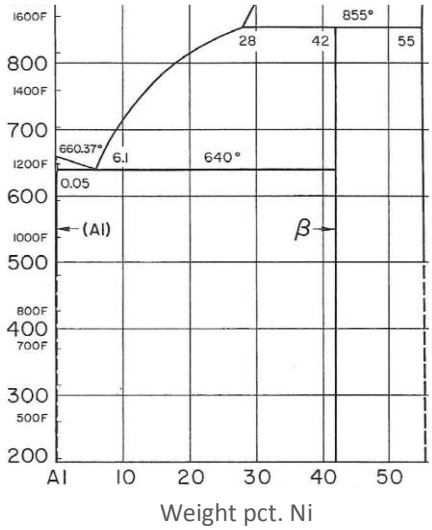

Fig. 1 Portion of the Al-Ni phase diagram

temperatures higher than 600°C and must contain second phase precipitate particles that are thermodynamically stable at the service temperature. Transition metal trialuminides with the general chemical formula Al_3X, in which X is a transition metal from the 3A-8A group, are excellent candidates for both the eutectic structure and the precipitate particles. Therefore, it is envisioned that an aluminum alloy for high temperature applicatiuons should be based on the Al-Al_3Ni system. As shown in Fig. 1 [1], nickel forms with aluminum a series of nickel aluminides; one of them is Al_3Ni (ß in the diagram). Aluminum forms a eutectic with Al_3Ni at 6.1 wt% nickel. The melting point of the Al-Al_3Ni eutectic is 640°C and the volume of the Al_3Ni phase in the eutectic is relatively large (about 9.7 wt%). In order to improve the high temperature tensile strength of the alloy, other transition metals, specifically, manganese, zirconium, and vanadium, are added to the Al-Al_3Ni eutectic composition so that upon artificially aging the alloy, transition metal trialuminides form in the α-aluminum phase of the eutectic and significantly strengthen it. The Al_3Ni eutectic phase provides a combination of good mechanical properties at room and elevated temperatures, a high solidus temperature that ensures thermal stability, and a narrow solidification range that guarantees good casting characteristics. Manganese, zirconium, and vanadium allow a

substantial precipitation strengthening effect that remains significant up to about 350°C.

RESEARCH OBJECTIVE

The objective of this work is to lay the necessary foundation for the design of aluminum alloys for use at temperatures approaching 350°C.

THESIS ORGANIZATION

The remainder of this document is a series of manuscripts to be submitted to various journals each representing a chapter of the dissertation as follows:

Chapter II contains a journal article titled "The Al-Al_3Ni Eutectic Reaction: crystallography and mechanism of formation".

Abstract: The characteristics of the Al-Al_3Ni eutectic structure are examined with emphasis on its morphology and crystallography. Based on these examinations, the mechanism of formation of this technologically important eutectic is postulated. It is found that a thin shell of α-Al forms coherently around each Al_3Ni fiber. The excellent thermal stability of the Al-Al_3Ni eutectic may be attributed to the presence of this coherent layer

Chapter III contains a journal article titled "Precipitation Strengthening

in Al-Ni-Mn Alloys".

Abstract: Precipitation hardening eutectic and hypoeutectic Al-Ni alloys by manganese is investigated with focus on the effect of the alloys' chemical composition and solidification cooling rate on microstructure and tensile strength. Within the context of the investigation, a mathematical model is developed and used to calculate the strengthening increment contributed by each of the phases present in the aged alloy. The model predictions agree well with measured values and suggest that the larger part of the alloy's yield strength is due to the Al_3Ni eutectic phase, this is closely followed by contribution from the Al_6Mn particles, which precipitate predominantly within grain boundaries.

Chapter IV contains a journal article titled "Precipitation Strengthening in Aluminum-Zirconium-Vanadium Alloys".

Abstract: $Al_3(Zr_{1-x}V_x)$Atom probe tomography (APT) and aberration corrected HRTEM were used to study the co-precipitation and coarsening mechanisms of $Al_3(Zr_{1-x}V_x)$ precipitates formed in Al-Zr alloys with various V contents. Also, the strengthening mechanism that is operative in properly aged Al-Zr-V alloys are determined, and the antiphase boundary (APB) energies between the aluminum matrix and the Al_3Zr and $Al_3(Zr_{1-x}V_x)$ precipitates were indirectly determined.

Chapter V contains a journal article titled "The Effect of Introducing the

Al-Ni Eutectic Composition into Al-Zr-V Alloys on Microstructure and Tensile Properties".

Abstract: Adding the Al-6Ni eutectic structure to an Al-0.4Zr-0.4V alloy completely replaces the typical dendritic structure of the alloy by an Al-Al_3Ni eutectic structure. After aging the Al-6Ni-0.4Zr-0.4V alloy at 400°C for 32 hours, which is an optimum heat treatment for this alloy, its yield strength reaches a maximum of 187 MPa. The increased yield strength comes from the eutectic Al_3Ni phase and the $Al_3(Zr_x,V_{1-x})$ precipitates. Theoretical calculations suggest that about 36% of the yield strength is contributed by the $Al_3(Zr_x,V_{1-x})$ precipitate and about 50% is contributed by the Al_3Ni eutectic phase.

Chapter VI contains a journal article titled "Stabilizing the $Al_{12}Mn$ Precipitates in Al-Mn Alloys by Alloying with Tungsten".

Abstract: The Al-Mn-W system has considerable potential as basis for lightweight aluminum alloys that are intended for use at temperatures approaching 350°C. In this ternary system, aluminum, manganese, and tungsten co-precipitate to form the meta-stable $Al_{12}(Mn_{(1-x)}W_x)$ phase, which is thermally stable and will not coarsen when held at elevated temperatures for extended periods of time. This enhanced thermal stability of the $Al_{12}(Mn_{(1-x)}W_x)$ phase in comparison to the $Al_{12}Mn$ phase which forms in binary Al-Mn alloys is explained in terms of the Gibbs

free energy of the two phases. It is shown that co-precipitating tungsten with aluminum and manganese lowers the Gibbs free energy of the precipitated phase and by so doing it slows down its coarsening rate and enhances its thermal stability.

References

[1] Aluminum Binary Alloy Phase Diagrams, Alloy Phase Diagrams, Vol 3, ASM Handbook, ASM International, 1992, pp. 2.4–2.56.

[2] Y.Y Fan, MS Thesis, Precipitation Strengthening of Aluminium by Transition Metal Aluminides, Worcester Polytechnic Institute, 2012, p. 36.

Chapter 2

The Al-Al_3Ni Eutectic Reaction: crystallography and mechanism of formation

Yangyang Fan and Makhlouf M. Makhlouf[1]

Department of Mechanical Engineering, Worcester Polytechnic Institute

Worcester, MA 01609, USA

Keywords: polyphase microstructure, eutectic phase transformation; eutectic solidification; nickel aluminide

ABSTRACT

The characteristics of the Al-Al_3Ni eutectic structure are examined with emphasis on its morphology and crystallography. Based on these examinations, the mechanism of formation of this technologically important eutectic is postulated. It is found that a thin shell of α-Al forms coherently around each Al_3Ni fiber. The excellent thermal stability of the Al-Al_3Ni eutectic may be attributed to the presence of this coherent layer.

INTRODUCTION

The Al-Al_3Ni eutectic reaction has been the subject of much interest over the past few decades [1-3]. The intense interest is understandable in light of the potential role that the Al-Al_3Ni eutectic structure can play in

[1] Corresponding author. Tel.: +1 508 831 5647; fax: 508 831 5993; e-mail: mmm@wpi.edu.

thermally stable shape casting alloys, and also in light of its potential for making aligned fiber composite materials for high strength applications. Recently, Dan, Georgeta, and Angel critically analyzed the Al-Ni binary phase diagram and concluded that the system contains two eutectic reactions, three peritectic reactions, and one peritectoid reaction [4]. In this publication we highlight the important characteristics of the Al-Al_3Ni eutectic structure that results from the reaction: $L \leftrightarrow Al + Al_3Ni$ with emphasis on the mechanism of its formation, its morphology, and its crystallography.

2. MATERIALS AND PROCEDURES

High purity aluminum (99.999) and Al-20 wt. % Ni master alloy were used to constitute an alloy of the eutectic composition. Specimens used for scanning electron microscopy (SEM) were sectioned from castings made in a copper mold, mounted in Bakelite and prepared for microscopy by standard metallographic methods. When needed, the specimens were etched with 5 pct. hydrofluoric acid. Specimens used for transmission electron microscopy (TEM) were produced by thinning foils of the alloy to perforation by means of a twinjet electro-polisher operating at 15 volts and utilizing a solution of 20 volume pct. perchloric acid in methanol maintained at -30°C. A JOEL-7000F scanning electron microscope and a JOEL-2010F transmission electron microscope were employed to perform

the microscopy.

3. RESULTS AND DISCUSSION

The microstructure of the Al-Al_3Ni eutectic is shown in Fig. 1. The Al_3Ni phase appears as long thin rods with an average diameter of about 100 nm and a length that varies between 1 and 10 μm. The Al_3Ni rods within any given grain are well aligned, which suggests that they have a specific orientation relationship with the α-Al matrix. The Wulff construction may be used to deduce the growth direction of the Al_3Ni fibers in the Al-Al_3Ni eutectic.

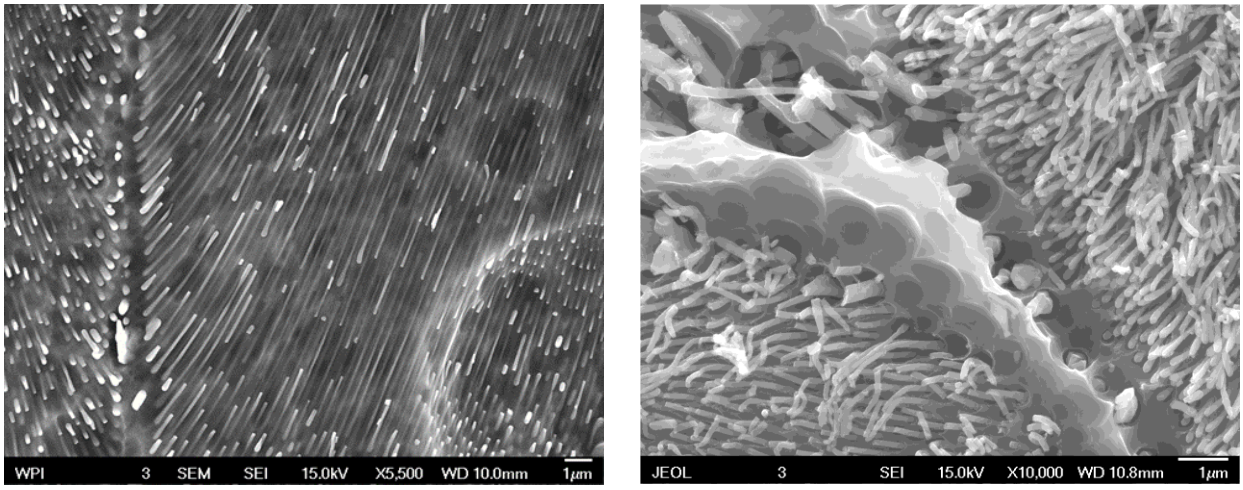

(a) (b)

Fig. 1 Microstructure of the Al-Al_3Ni eutectic. (a) The Al_3Ni fibers within a given grain are well aligned, which suggests that they have a specific orientation relationship with the surrounding α-Al matrix. (b) Deep-etched sample showing the fibrous morphology of the Al_3Ni eutectic phase.

The Al_3Ni crystal lattice is shown schematically in Fig. 2 and the atomic positions in the crystal lattice are given in Table 1 [5].

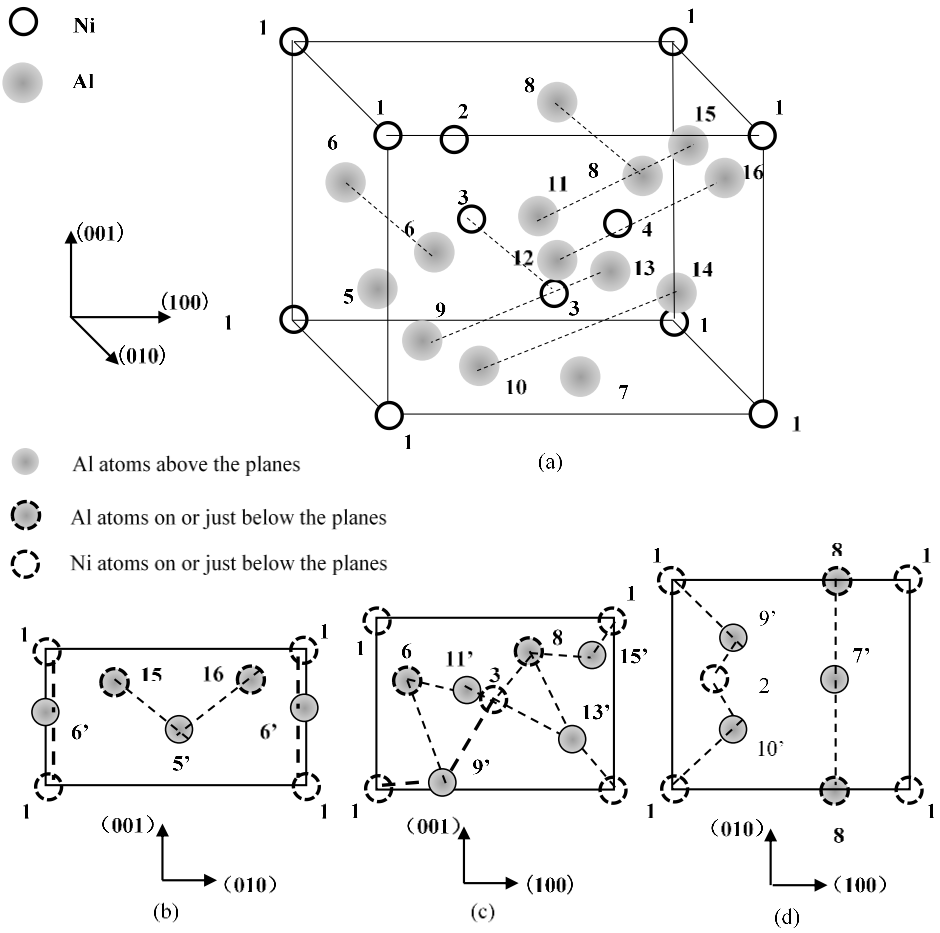

Fig. 2 Schematic representation of the Al_3Ni crystal lattice showing the positions of Al and Ni atoms.

Table 1. Atom positions in the Al_3Ni crystal.

Atom	Coordination number		
	x	y	z
Ni	0.000	0.000	0.000
Ni	0.262	0.500	0.890
Ni	0.500	0.000	0.390
Ni	0.762	0.500	0.500
Al	0.120	0.500	0.360
Al	0.142	0.000	0.530
Al	0.620	0.500	0.030
Al	0.642	0.000	0.860
Al	0.305	0.197	0.089
Al	0.305	0.803	0.089
Al	0.457	0.303	0.598
Al	0.457	0.697	0.589
Al	0.805	0.197	0.301
Al	0.805	0.803	0.301
Al	0.957	0.303	0.801
Al	0.957	0.697	0.801

In this crystal structure each Ni atom is surrounded by nine Al atoms and each Al atom is surrounded by three Ni atoms. Table 2 shows the surface energies of the low index planes in Al_3Ni. These energies were calculated by the Born-Stern method [6], which states that the surface energy σ of an (*hkl*) plane is given by

$$\sigma = \frac{\sum \varepsilon_{ij}}{2S_{(hkl)}} \quad (1)$$

In Eq. (1), $\sum \varepsilon_{ij}$ is the total binding energy on the (*hkl*) plane and $S_{(hkl)}$ is the surface area of the (*hkl*) plane. Al_3Ni has the Pnma crystal structure with lattice parameters a = 0.66115 nm, b = 0.73364 nm, and c = 0.48118 nm [7].

Table 2. Calculated surface energy of low index planes in the Al_3Ni crystal.

Plane (*hkl*)	Area (nm^2)	Number of nearest neighbors on plane	Total binding energy (ev)	Surface energy (ev/nm^2)
(100)	0.35304	4 Al-Ni and 2 Al-Al	2.62	3.71
(010)	0.31684	6 Al-Ni and 4 Al-Al	4.04	6.38
(001)	0.48508	4 Al-Ni and 2 Al-Al	2.62	5.40

The first order approximation is used to calculate the total binding energy on the low index planes, i.e., only the cohesive energy between nearest neighbors is considered in this calculation. In order to be nearest neighbors, the distance between two Ni atoms must be less than 0.3884 nm and the distance between an Al atom and a Ni atom must be less than 0.27746 nm [5]. Fig. 2(b)-(d) shows that there are four Al-Ni nearest neighbors on the (001) plane; there are six Al-Ni nearest neighbors and

four Al-Al nearest neighbors on the (010) plane; and there are four Al-Ni nearest neighbors and two Al-Al nearest neighbors on the (001) plane. The Al-Ni bond energy is equal to 0.6 ev [8], and the Al-Al bond energy is equal to 0.11 ev [7]. With this information, the total binding energy for each one of these planes is calculated and summarized in Table 4. Knowing that the surface area of the (100), (010), and (001) planes equals $b\times c$, $a\times c$, and $a\times b$, respectively; then Eq. (1) is used to calculate the surface energy of each of these planes and the results are shown in Table 2. It is clear that for Al_3Ni, the surface energy of the (010) plane is significantly higher than the surface energy of any one of the other low index planes. Therefore, it is concluded that the Al_3Ni fibers in the Al-Al_3Ni eutectic preferentially grow along the <010> direction.

Fig. 3(a) is a TEM photomicrograph of the Al-Al_3Ni eutectic structure. In making this micrograph, the foil was carefully tilted so that the zone axis of the Al_3Ni fibers lies parallel to its growth direction; i.e., parallel to the <010> direction. This alignment caused the Al_3Ni fibers to appear as ellipses, and the select area diffraction pattern (SADP) shown in Fig. 3(b) was produced from this tilted foil. A second SADP can be distinguished in Fig. 3(b) and it is contributed by the α-Al matrix. The zone axis of the α-Al phase is indexed as <321> so that the orientation relationship is: Al_3Ni <010> // Al <321>; Al_3Ni (102)//Al $(\bar{1}11)$; Al_3Ni (602) is about 3° misaligned to the α-Al $(\bar{2}4\bar{2})$. This orientation relationship is slightly

different from that reported by B. Cantor [9].

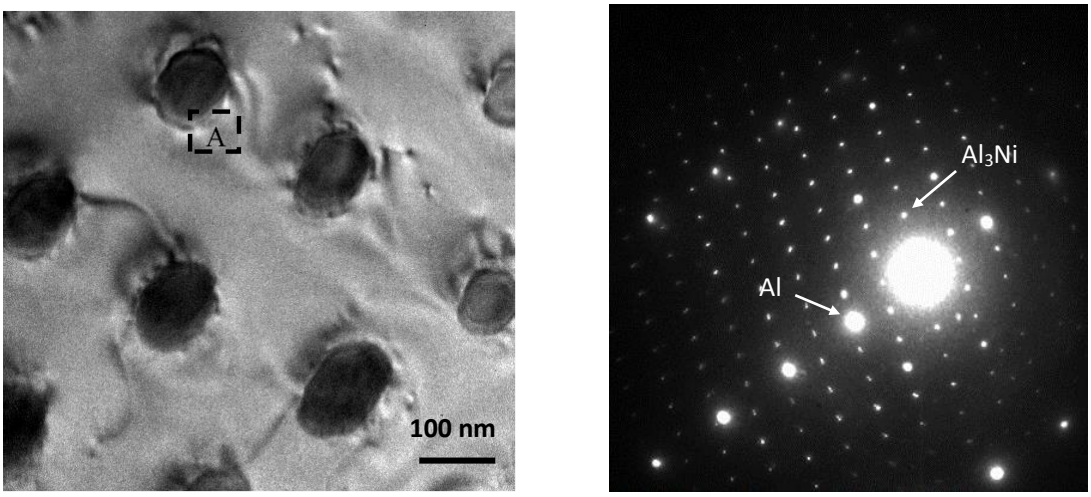

(a) (b)

Fig. 3 (a) TEM photomicrograph of the Al-Al_3Ni eutectic structure with the foil tilted so that the zone axis of the Al_3Ni fibers lies parallel to its growth direction thus causing the Al_3Ni fibers to appear as dark ellipses. (b) Select area diffraction pattern (SADP) produced from the tilted foil used to make the micrograph in (a).

Fig. 4 is a high resolution TEM (HRTEM) photomicrograph taken at the location marked 'A' in Fig. 4. In this micrograph, the Al_3Ni phase is clearly distinguished from the α-Al phase by means of Z contrast. Careful examination of Fig. 4 shows that there is a thin layer of α-Al (≈ 3 nm) sandwiched between each Al_3Ni fiber and the surrounding α-Al phase. This thin layer of α-Al is orientated differently from the rest of the α-Al phase. Based on d-spacing measurements, the α-Al shell is indexed as (100). The d-spacing of the surrounding α-Al is 0.233 nm and is consistent with the $(\bar{1}11)$ plane. Fig. 4 also shows that part of the Al_3Ni is coherent with this thin α-Al layer and the coherency relation is Al_3Ni (101) // Al (100). These observations are used to postulate the following model for the evolution of the eutectic Al-Al_3Ni structure.

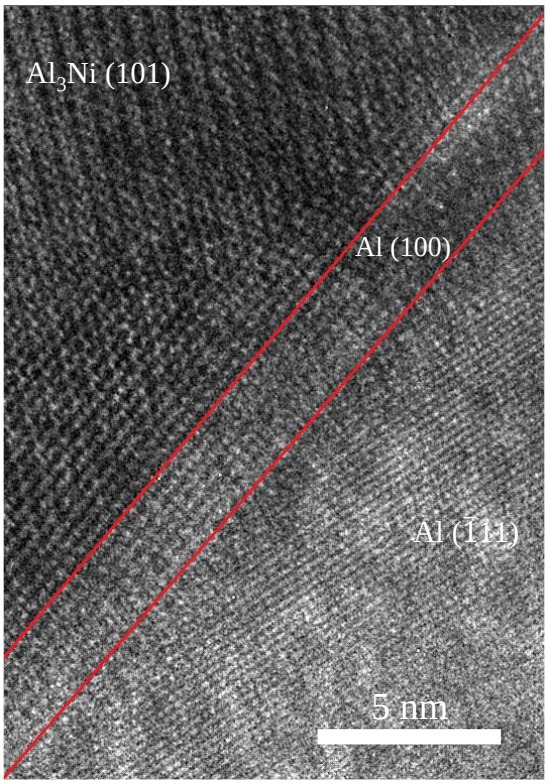

Fig.4 High resolution TEM (HRTEM) photomicrograph taken at the location marked 'A' in Fig. 3. In this micrograph, the Al_3Ni phase is clearly distinguished from the α-Al phase by means of Z contrast. There is a thin layer of α-Al (≈ 3 nm) sandwiched between the Al_3Ni fiber and the surrounding α-Al phase.

First, it is submitted that the Al-Al_3Ni eutectic is abnormal. In abnormal binary eutectics, there is a large difference in the rates of nucleation and growth of the two phases and as a result of this difference, the coupling of the crystallization process of the two phases is much weaker than in normal eutectics. Also, in an abnormal binary eutectic, one phase is always present in a much smaller quantity than the other phase, and the eutectic particles of the minor phase usually take the form of plates or fibers that are surrounded by mantles of the major phase. However, the envelopment of the minor phase by the mantle of the major phase is not complete. Therefore, in Al-Al_3Ni eutectic solidification, the two phases are not equals in determining the mode of solidification, one must

dominate (i.e., lead) the other. Since the Al-Al_3Ni eutectic occurs at 6.1 wt. % Al_3Ni, Al_3Ni fibers lead and become partially covered with a mantle of α-Al (the aluminum-rich terminal solid solution). The Al_3Ni phase dominates in determining the eutectic structure. It not only nucleates easily, but it grows rapidly and projects ahead of the eutectic α-Al phase into the liquid and by doing so, it depletes its immediate surroundings of Ni and causes significant undercooling of the α-Al phase.

Next, a thin shell (≈ 3 nm) of α-Al forms coherently around the Al_3Ni fiber driven by the large undercooling experienced by the α-Al phase closest to the Al_3Ni fiber. This α-Al shell surrounds the Al_3Ni fiber, which can grow only along its preferred growth direction. Finally, the rest of the α-Al phase follows the growing Al_3Ni – α-Al '*composite*' rod and solidifies forming a stacking fault on the α-Al shell. Because the mismatch between Al_3Ni (101) and α-Al (100) is only about 3.9%, the interface between the α-Al shell and the Al_3Ni fiber is coherent, and as such, it effectively protects the Al_3Ni fiber from coarsening.

Under normal solidification conditions, the eutectic α-Al mantle does not overtake the growing edge of the Al_3Ni fiber, and as the rate of heat extraction from the solidifying material increases, the eutectic Al_3Ni fibers that are projecting ahead of their α-Al mantles at the solid/liquid interface grow rapidly into the super-cooled liquid. Since a large temperature gradient is quickly established along these fibers, the

probability of eutectic α-Al nucleating on these fibers is high and α-Al mantles develop rapidly around them. The growth of the Al_3Ni fibers stops only when the rate of heat extraction becomes large enough to permit rapid growth of the α-Al mantles so that they overtake the Al_3Ni fibers, as shown in Fig. 8. The α-Al mantles surround the Al_3Ni – α-Al '*composite*' rods, and eutectic solidification beyond this stage requires the re-nucleation of the Al_3Ni phase. Growth of the α-Al mantles creates the required regions of high Ni concentration to assist this re-nucleation of the Al_3Ni phase.

4. CONCLUSIONS

1) Because the volume fraction of the Al_3Ni phase in the Al-Al_3Ni binary eutectic is less than 0.28 (it is 0.097), the typical Al-Al_3Ni eutectic is a fibrous structure.

2) Although the Al-Al_3Ni eutectic consists of one faceted phase (Al_3Ni) and one non-faceted phase (α-Al), the eutectic morphology is regular and resembles that of a non-faceted – non-faceted eutectic.

3) The growth behavior of the Al_3Ni fibers is anisotropic, and the growth axis is always approximately aligned with the [010] direction of the Al_3Ni crystal lattice.

4) The Al_3Ni phase dominates in determining the eutectic structure, and once it is formed, a thin shell (≈ 3 nm) of coherent α-Al forms around it. The rest of the α-Al phase follows the growing Al_3Ni – α-Al '*composite*' rod and solidifies forming a stacking fault on the α-Al shell.

5) The excellent thermal stability of the Al-Al_3Ni eutectic may be attributed to the existence of a thin coherent layer of α-Al surrounding each Al_3Ni fiber. The low energy interface between the α-Al shell and the Al_3Ni phase mitigates coarsening of the Al_3Ni fibers.

REFERENCES

1. B.J. Bayles, J.A. Ford, and M.T. Salkind, Trans, Met. Soc., 239 (1967) 844.
2. D. Jaffrey G. Chadwick, Metal. Trans., 1 (1970) 3389.
3. H.E. Cline, Acta Met., 19 (1971) 481.
4. B. Dan, C. Georgeta, and A. Angel, Metalurgia International, 11 (2006) 36.
5. G. Cubiotti, E.E. Krasovskii, O.V. Slobodyan, Y. N. Kucherenko, and V.N. Antonov, J. Phys. Condens. Matter, 7 (1995) 4865.

6. A. Pimpinelli, Physics of Crystal Growth, Cambridge University Press, 1998.

7. W.B. Pearson, Handbook of Lattice Spacing and Structures of Metals and Alloys, Pergamon Press, 1967.

8. D. Hackenbracht, and J. Kübler, J. Phys. F Metal Phys., 10, (1980) 427.

9. B. Cantor, G.A. Chadwick, J. Mater. Sci., 10 (1975) 578.

Chapter 3

Precipitation Strengthening in Al-Ni-Mn Alloys

Yangyang Fan[1] Kai Huang[2] and Makhlouf M. Makhlouf[3]

Department of Mechanical Engineering, Worcester Polytechnic Institute

Worcester, MA 01609, USA

[1]fyang@wpi.edu, [2]khuang@wpi.edu, [3]mmm@wpi.edu

Keywords: precipitation hardening, aluminum alloys, Al_6Mn, Al_3Ni.

ABSTRACT

Precipitation hardening eutectic and hypoeutectic Al-Ni alloys by manganese (from 2 wt.% to 4 wt.%) is investigated with focus on the effect of the alloys' chemical composition and solidification cooling rate on microstructure and tensile strength. Within the context of the investigation, a mathematical model is developed and used to calculate the strengthening increment contributed by each of the phases present in the aged alloy. The model predictions agree well with measured values and suggest that the larger part of the alloy's yield strength is due to the Al_3Ni eutectic phase, this is closely followed by contribution from the Al_6Mn particles, which precipitate predominantly within grain boundaries.

NOMENCLATURE

A_o	Average area fraction of *O* phase
b	Burgers vectors, for aluminum b = 0.286 nm [1]
D_o	The spacing between two adjacent Al_3Ni eutectic on the slip plane
f_{Al_3Ni}	Volume fraction of the Al_3Ni phase
f_{Al_6Mn}	Volume fraction of the Al_6Mn phase
f_o	Volume fraction of the *O* phase
G	Shear modulus on the slip plane, for aluminum G = 26.2 GPa [1]
l	Average major axis of the Al_6Mn ellipsoid, l = 350 nm
m_{Ni}	Mass fraction of nickel
m_{Mn}	Mass fraction of manganese
M	Taylor factor (M = 3.06) [2]
$M_{Al_{60}Mn_{11}Ni_4}$	Molecular mass of the *O* phase ($g.mol^{-1}$)
M_{Mn}	Atomic mass of manganese ($g.mol^{-1}$)
M_{Ni}	Atomic mass of nickel ($g.mol^{-1}$)
R	Average radius of the Al_3Ni eutectic
t	Average minor axis of the Al_6Mn ellipsoid, t = 200 nm
θ	Angle between the Al_3Ni eutectic and the slip plane of the dislocations in aluminum
ν	Poisson's ratio, for aluminum ν = 0.362 [3]
ρ_{Al}	Density of Al = 2.71 $g.cm^{-3}$

ρ_{Al_6Mn}	Density of the Al_6Mn phase = 3.3 g.cm^{-3} [4]
ρ_o	Density of the *O* phase = 3.62 g.cm^{-3} [4]
σ_{Al}	Yield strength of pure aluminum = 28 MPa [5]
$\Delta\sigma_{Al_3Ni}$	Yield strength that is contributed by the Al_3Ni phase (MPa)
$\Delta\sigma_{Al_6Mn}$	Yield strength that is contributed by the Al_6Mn phase (MPa)
$\Delta\tau_{edge}$	Shear strength increment due to particle looping by edge dislocations
$\Delta\tau_{screw}$	Shear strength increment due to particle looping by screw dislocations
φ_{Mn}	Mass of manganese in aluminum solid solution per unit volume of solid alloy (g.cm^{-3})

INTRODUCTION

It has been shown that aluminum alloys that contain appreciable amounts of the aluminum-nickel eutectic structure exhibit excellent fluidity and very good resistance to hot-tearing [6]. Moreover the Al_3Ni eutectic phase, which is typically in the form of thin fibers, adds significant strength to aluminum by the well-known Orowan looping mechanism [7]. Furthermore, the Al_3Ni eutectic are chemically and thermally stable, and resist coarsening up to 500°C [8]. For these reasons, alloys based on this eutectic system are potential replacements for traditional aluminum alloys in high temperature applications. The yield strength of this binary eutectic does not exceed 100 MPa at room temperature and 50 MPa at 300°C [9], which falls short of the current requirements of many engineering applications. Hence, it is necessary to add to aluminum and nickel other strength inducing alloying elements – preferably ones that allow precipitation hardening by thermally stable precipitates. Many of the currently available age-hardenable aluminum alloys are precipitation hardened by Al_2Cu, and/or Mg_2Si precipitates. However, because of the high diffusivity of copper, magnesium, and silicon in aluminum, and the low thermal stability of the Al_2Cu and Mg_2Si phases, these precipitates tend to coarsen and dissolve in the aluminum matrix when the alloy is used at temperatures exceeding 250°C [10]. Al_6Mn precipitates, which can form in aluminum by aging at

temperatures between 400- 450°C, are stable at significantly higher temperatures [11], and are thus an attractive alternative. This is mainly because the diffusivity in aluminum of manganese is much smaller than that of copper, magnesium, and silicon (e.g., at 450°C, $D_{Mn} = 2.16\times10^{-6}$ m^2/s, $D_{Cu} = 8.21\times10^{-6}$ m^2/s, $D_{Mg} = 6.18\times10^{-6}$ m^2/s, and $D_{Si} = 8.81\times10^{-6}$ m^2/s) [12]. Consequently, Al_6Mn precipitates coarsen at a much slower rate than Al_2Cu and Mg_2Si precipitates. For example, at 240°C, the coarsening kinetics constant of Al_2Cu is 690 nm^3/s compared to 0.00234 nm^3/s for Al_6Mn at 500°C [13]. Unfortunately, because the equilibrium solubility of manganese in solid aluminum is small (max. solubility = 1.2 wt. pct. at 659°C [14]), the maximum volume fraction of Al_6Mn precipitate that may form in aluminum by a typical heat treatment regimen is only 5.8%. Consequently, the strengthening increment attained by the presence of the Al_6Mn phase in aluminum is limited. However, the volume fraction of Al_6Mn precipitate may be significantly increased by adopting a non-traditional heat treatment regimen in which the molten alloy is cast at a high enough cooling rate so that a supersaturated solid solution of manganese in aluminum is obtained directly from the melt. In this non-traditional heat treatment scenario a homogenization step is not required, and the supersaturated solid solution that is produced can be made to contain much more manganese than is possible by traditional heat treatment because the solubility of

manganese in liquid aluminum is much higher than in solid aluminum [11]. Rapid cooling preserves as nearly intact as possible the solid solution formed at the melting temperature.

The work reported herein concerns precipitation strengthening in the Al-Ni-Mn system when this non-traditional heat treatment method is used to form an *ultra*-super saturated solid solution of manganese in aluminum, which – upon aging – leads to precipitation of an unusually high volume fraction of Al_6Mn particles.

Three different phases contribute to the strength of the Al-Ni-Mn alloy. These are the α-Al phase, the Al_3Ni phase, and the Al_6Mn phase[2], and the strength of the alloy may be expressed as a linear sum of the strengthening increments contributed by these three phases, as shown in (1),

$$\sigma_{Total} = \sigma_{Al} + \Delta\sigma_{Al_3Ni} + \Delta\sigma_{Al_6Mn} \quad (1)$$

Since the solubility of manganese and nickel in solid aluminum is negligible, then the yield strength of the α-Al phase may be assumed equal to the yield strength of pure aluminum, so that [5]

$$\sigma_{Al} = 28\ \text{MPa} \quad (2)$$

The Al_3Ni eutectic are approximately 100 nm in diameter and several micrometers in length so they tend to strengthen the α-Al phase by the

[2] It is assumed that the solidification cooling rate is fast enough that formation of primary *O* phase is negligible.

Orowan looping mechanism. Hence, the increment increase in shear strength due to looping may be calculated from (3) in the case of edge dislocations looping the fibers and (4) in the case of screw dislocations [15]

$$\Delta\tau_{edge} = \frac{2A}{bD_0} \tag{3}$$

where $A = \frac{Gb^2}{4\pi}\ln(\frac{\pi R}{2b})$

and $$\Delta\tau_{screw} = \frac{1}{\sqrt{1-\nu}}\Delta\tau_{edge} \tag{4}$$

Because the Al_3Ni eutectic are perfectly orientated within each grain [16], then D_o in Eq. (3) may be related to f_{Al_3Ni} and $\cos\theta$ as shown in Eq. (5)

$$D_o = \frac{\left(\frac{\sqrt{\pi}R}{\sqrt{f}} - 2R\right)}{\cos\theta} \tag{5}$$

Fig.1 sketches the Al_3Ni eutectic growth direction and slip plane in aluminum. Because the growth direction of Al_3Ni is not exactly normal to the slip plane, the effective distance between Al_3Ni eutectic, D_o is increased if projecting Al_3Ni eutectic on the slip plane, and this increment can be determined by the angle between the growth direction of Al_3Ni and slip plane, as Eq. 5 shown. A major orientation relationship between aluminum and the Al_3Ni eutectic in the Al-Al_3Ni eutectic is <010>Al_3Ni // <321> Al [7, 17]. Therefore cos θ is calculated as follows

$$\cos\theta = \frac{(321)(111)}{|321||111|} = 0.926$$

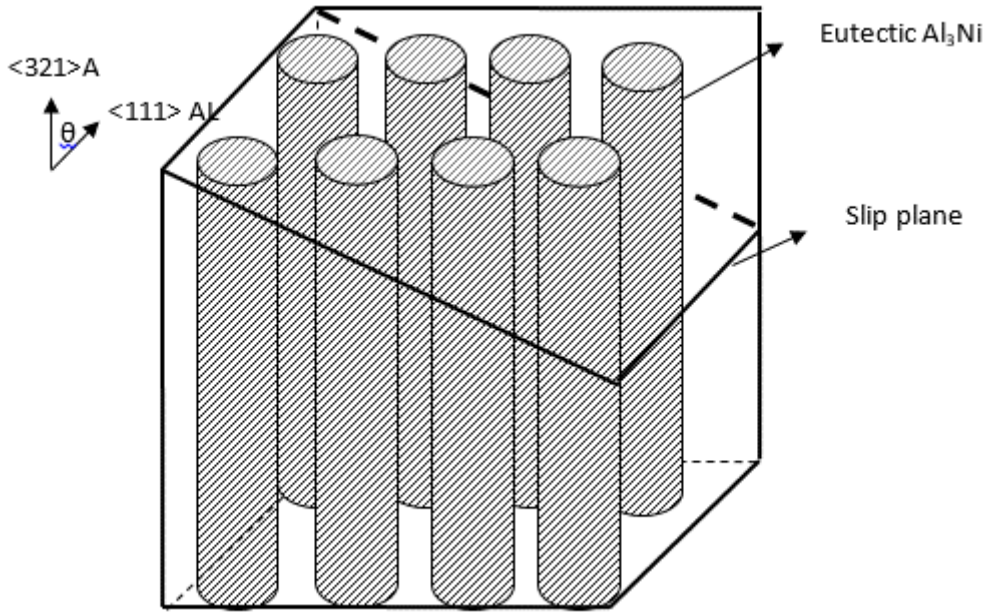

Fig. 1 The sketch of the growth direction of eutectic Al_3Ni phase and slip plane.

The Taylor factor is then used to convert the increment increase in shear stress obtained in (3) and (4) to increment increase in yield strength [2]

$$\Delta\sigma = M\Delta\tau$$

Using (3) – (5), the additional yield strength due to fiber looping by edge dislocations is

$$\Delta\sigma_{edge} = M\frac{Gbcos\theta}{2\pi(\sqrt{\pi}\frac{R}{\sqrt{f}}-2R)}ln(\frac{R}{b}) \quad (6)$$

and due to fiber looping by screw dislocations is

$$\Delta\sigma_{screw} = \frac{1}{\sqrt{1-\nu}}\Delta\sigma_{edge} \quad (7)$$

Assuming an equal number of screw and edge dislocations is present in the alloy, and assuming that the growth directions of the Al_3Ni eutectic are equally favored, then the strengthening increment due to the Al_3Ni

eutectic phase is

$$\Delta\sigma_{Al_3Ni} = \frac{M\left(1+\frac{1}{\sqrt{1-\nu}}\right)}{2}\frac{0.926Gb}{2\pi\left(\sqrt{\pi}\frac{R}{\sqrt{f_{Al_3Ni}}}-2R\right)}\ln\left(\frac{R}{b}\right) \quad (8)$$

The Al_6Mn precipitate particles in α-Al tend to be ellipsoidal in shape [18], therefore their contribution to yield strength may be calculated by (9)

$$\Delta\sigma_{Al_6Mn} = M\frac{0.81Gb}{2\pi(1-\nu)}\left(\frac{1+{}^{l}/_{\lambda}}{\lambda}\right)\ln\left(\frac{t}{b}\right) \quad (9)$$

where $\lambda = \sqrt{\frac{lt}{f_{Al_6Mn}}}$

Substituting (2), (8), and (9) into (1) gives the yield strength of the Al-Ni-Mn alloy as

$$\sigma = 28\,MPa + \frac{M\left(1+\frac{1}{\sqrt{1-\nu}}\right)}{2}\frac{0.926Gb}{2\pi\left(\sqrt{\pi}\frac{R}{\sqrt{f_{Al_3Ni}}}-2R\right)}ln\left(\frac{R}{b}\right) + M\frac{0.81Gb}{2\pi\sqrt{1-\nu}}\left(\frac{l+\sqrt{\frac{lt}{f_{Al_6Mn}}}}{\frac{lt}{f_{Al_6Mn}}}\right)ln\left(\frac{t}{b}\right) \quad (10)$$

Equation (10) suggests that the yield strength of the Al-Ni-Mn alloy depends to a large extent on the size and volume fraction of the of the Al_3Ni eutectic and Al_6Mn precipitate particles, which in turn depend on the chemical composition of the alloy and its cooling rate during solidification.

This paper focuses on precipitation strengthening in the Al-Ni-Mn system, and examines the interaction between the alloys' chemical composition, its cooling rate from the melt, and the resulting microstructure and yield strength.

MATERIALS AND PROCEDURES

Six alloy compositions in the Al-Ni-Mn system were constituted from pure aluminum ingots (99.999% purity), Al-20wt% Ni, and Al-25wt% Mn master alloys. The alloys were melted in an induction furnace in clean silicon carbide crucibles coated with boron nitride. The melts were degassed with high purity argon gas by means of a rotating impeller degasser for 30 minutes, and they were poured at approximately 800°C. Casting was performed in a brass mold and also in a water chilled copper mold. The water chilled copper mold produces standard sub size tensile specimens with a uniform cooling rate of about 90°C/s. The brass mold has a cone shape, and provides specimens with a range of cooling rates between 90°C/s at its narrowest end and 3.8°C/s at its widest end[3]. The specimens were aged in an electric furnace and were cooled from the aging temperature to room temperature in air. The chemical compositions of the alloys and the isothermal aging schedules employed

[3] Here the cooling rate ≡ the measured average cooling rate between 820°C and 660°C.

are shown in Table I.

Specimens used for scanning electron microscopy (SEM) were mounted in Bakelite and prepared for analysis by standard metallographic methods. When needed, the specimens were etched with 5 vol.% hydrofluoric acid. The measurements of the area fractions of phases in SEM pictures were performed by using Image J software. Specimens used for transmission electron microscopy (TEM) were produced by thinning foils of the alloy to perforation by means of a twinjet electro-polisher (Fischione Instruments, model 120) operating at 12 volts and utilizing a solution of 20 vol.% perchloric acid in methanol maintained at -20°C. A JOEL-7000F scanning electron microscope and a JOEL-2010F transmission electron microscope were employed to perform the microscopy. X-ray diffraction was performed with a diffractometer (PANalytical, Emperion model) in order to identify the various phases present in the alloys.

Tensile properties of the alloys were measured by means of a Universal Testing machine (Instron model 5500R) at an extension rate of 0.05 in/min. A 1-inch gage length extensometer (MTS model 634.25E-24) was used to measure extension. The tensile tests were performed on the 1" sub-size (ASTM E8-04) rectangular specimens. At least 5 specimens were used for each measurement and the results were averaged and the

standard deviations were calculated. Fracture of all specimens took place within the gage length and specimens with severe porosity and/or oxides that would affect the results were excluded.

Table I. Nominal chemical composition and heat treatment of the alloys.

#	Composition (wt. %)	Casting Condition	Heat Treatment
1	Al-6Ni-4Mn	Brass mold	None
		Water chilled mold	Aged at 450°C for times between 0.5 to 64 hours
		Water chilled mold	Aged at 400°C for times between 0.5 to 64 hours
2	Al-6Ni-3Mn	Brass mold	None
		Water chilled mold	Aged at 450°C for 1 hour
3	Al-6Ni-2Mn	Brass mold	None
		Water chilled mold	Aged at 450°C for 1 hour
4	Al-4Ni-4Mn	Brass mold	None
		Water chilled mold	Aged at 450°C for 1 hour
5	Al-4Ni-3Mn	Brass mold	None
		Water chilled mold	Aged at 450°C for 1 hour
6	Al-4Ni-2Mn	Brass mold	None
		Water chilled mold	Aged at 450°C for 1 hour

RESULTS AND DISCUSSION

Fig. 2 shows SEM photomicrographs of the as-cast microstructure of Al-6Ni-4Mn and Al-4Ni-4Mn alloys cooled at 5°C/s. The phases present in both of these slowly cooled alloys are eutectic α-Al, eutectic Al_3Ni, and primary $Al_{60}Mn_{11}Ni_4$ – which is usually referred to as the *O* phase [19].

In addition to these three phases, the Al-4Ni-4Mn alloy contains primary α-Al dendrites.

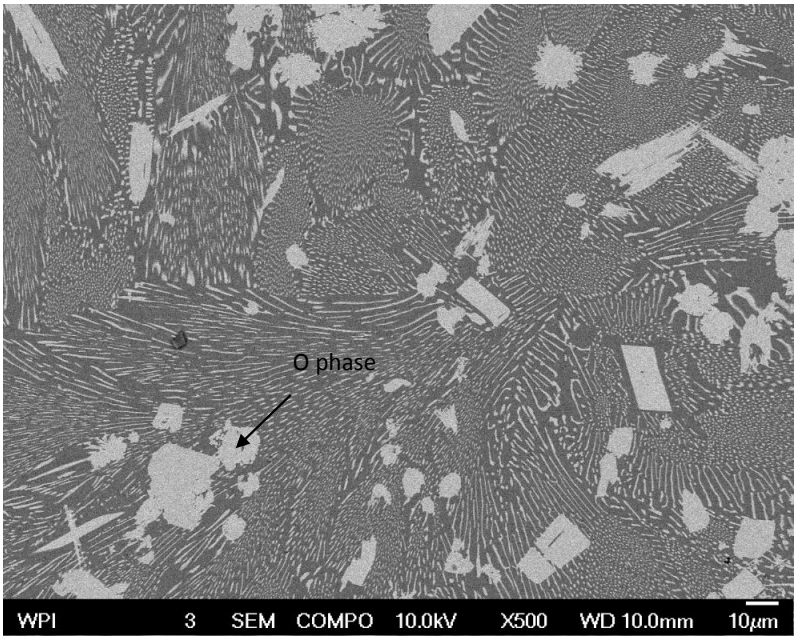

(a)

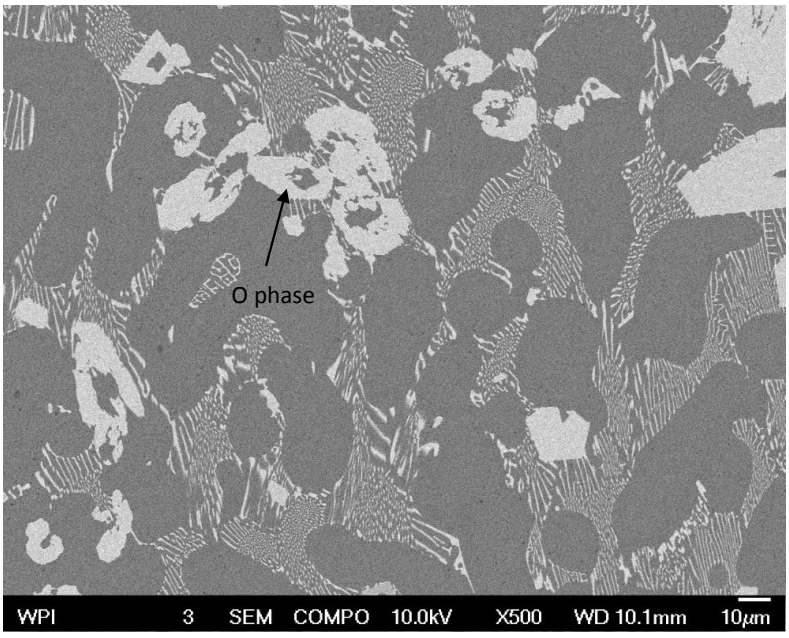

(b)

Fig. 2 SEM photomicrograph showing the as-cast microstructure of (a) Al-6Ni-4Mn alloy, and (b) Al-4Ni-4Mn alloy. Both alloys were cast with 5°C/s cooling rate.

Fig. 3 shows an x-ray diffraction pattern of the Al-6Ni-4Mn alloy and confirms the presence of all three phases in this alloy composition. The eutectic Al_3Ni phase is an orthorhombic intermetallic compound with lattice parameters a = 0.66 nm, b = 0.74 nm, and c = 0.48 nm [4]. The O phase is also an orthorhombic intermetallic compound and has lattice parameters a = 2.38nm, b = 1.25nm, and c = 7.55nm [19].

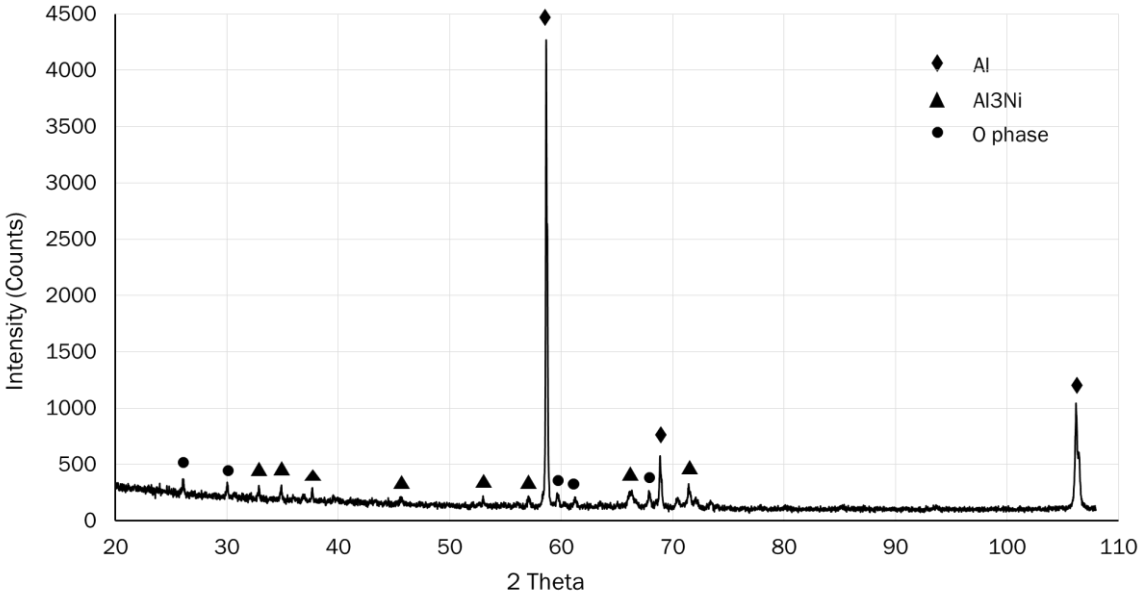

Fig. 3 X-ray diffraction pattern of as-cast Al-6Ni-4Mn alloy cast with 5°C/s cooling rate.

S. Balanetskyy [19] investigated the Al-rich corner of the Al-Ni-Mn ternary phase diagram, and suggested that a $\kappa - (Al_{80.3}Ni_{17.5}Mn_{2.2})$ phase forms in Al-4Ni-Mn alloys. However both x-ray and SEM examinations did not indicate formation of this phase under the conditions of this investigation.

Effect of cooling rate on alloy microstructure – The eutectic α-Al and eutectic Al_3Ni phases are present in all the alloys of Table I, but as Fig. 4 shows, the *O* phase is not present in all alloys for all cooling rates. For example, it is not present in the Al-4Ni-2Mn alloy solidified with any of the cooling rates used in this work, nor is it present in the Al-6Ni-2Mn alloy solidified with cooling rates higher than 50°C/s and the Al-4Ni-3Mn alloy solidified with cooling rates higher than 70°C/s.

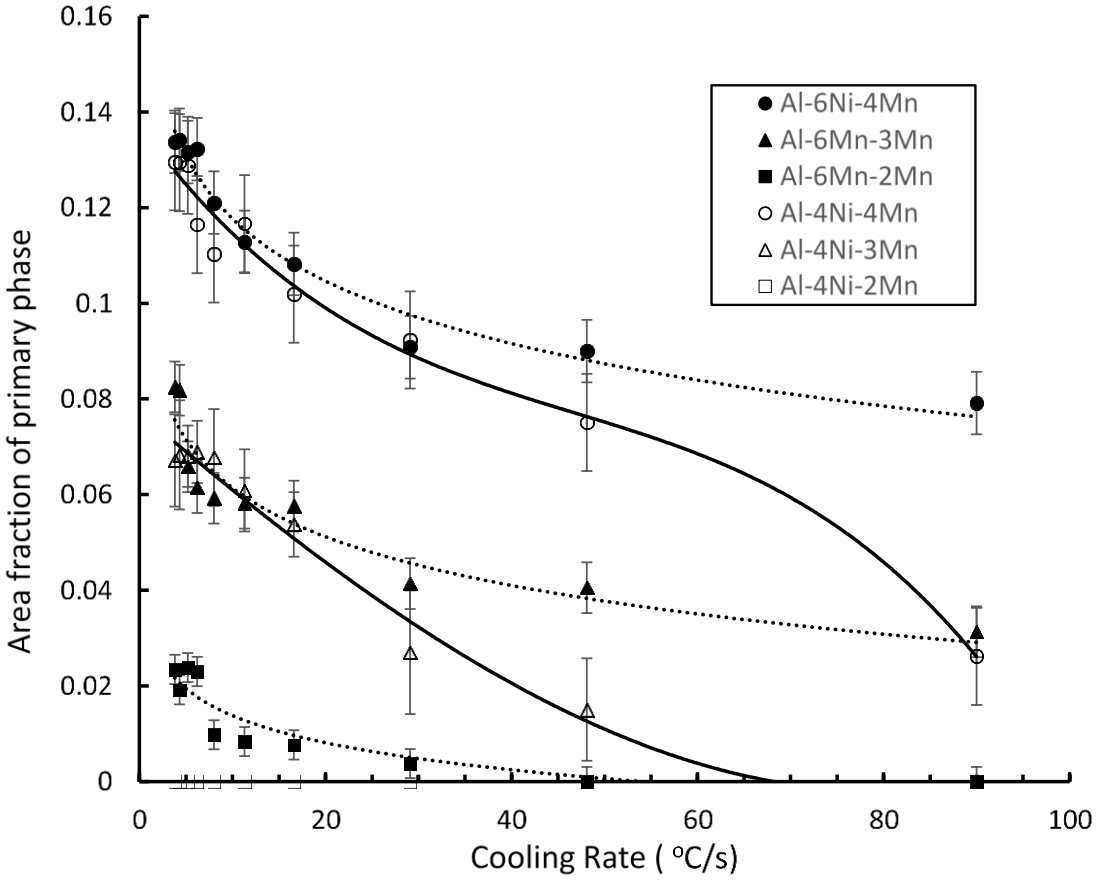

Fig. 4 Measured area fraction of *O* phase as a function of cooling rate.

Fig. 5 is a TEM photomicrograph of the Al-6Ni-4Mn alloy. It shows that in addition to affecting the presence (or absence) of the *O* phase in the

alloy's microstructure, the cooling rate during solidification also affects the morphology of the eutectic Al_3Ni phase. At the high cooling rate (90°C/s), the eutectic Al_3Ni phase is in the form of fibers approximately 100 nm in diameter that are perfectly oriented within each grain. On the other hand, at the low cooling rate (5°C/s), the fibers are coarser and exhibit obvious perturbations in radius along their length.

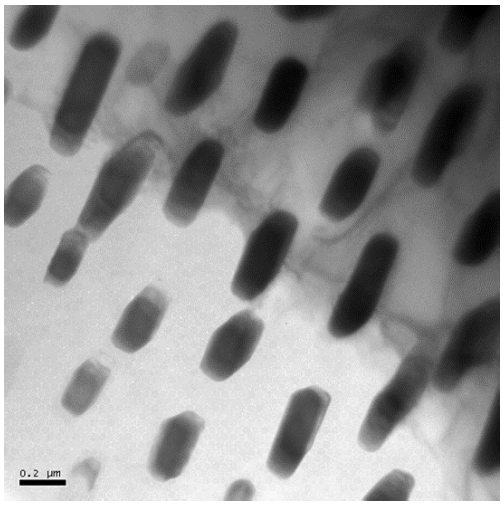

(a)

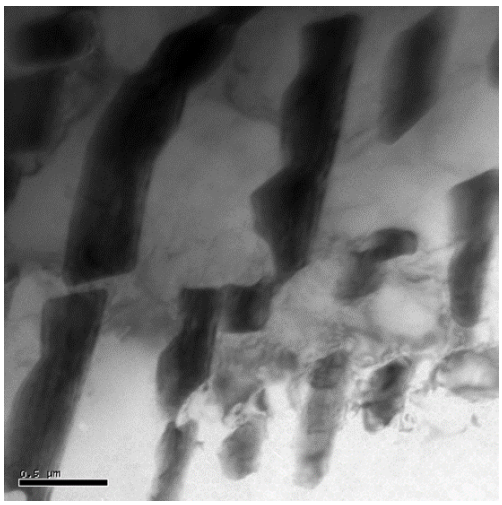

(b)

Fig. 5 TEM photomicrograph showing the as-cast microstructure of Al-6Ni-4Mn alloy, (a) cast with 90°C/s cooling rate, and (b) cast with 5°C/s cooling rate.

Effect of chemical composition on alloy microstructure – Fig. 6 shows SEM photomicrographs of various Al-Ni-Mn alloys and illustrates the effect of alloy composition on the microstructure of the alloy. The chemical composition of the Al-Ni-Mn alloy affects predominantly the amount of *O* phase present in the alloy's microstructure. Fig. 6, together with Fig. 4, demonstrate that a higher Ni and/or higher Mn content enhances formation of the *O* phase. The *O* phase is rich in Mn (14.55 wt.% Mn) [19], so its formation in excess deprives the supersaturated solid solution of this element and by doing so it limits precipitation strengthening by Al_6Mn precipitate particles. Moreover, the *O* phase is rich in Ni (5.3 wt. % Ni), so its formation reduces the amount of Al_3Ni eutectic that form by the eutectic reaction.

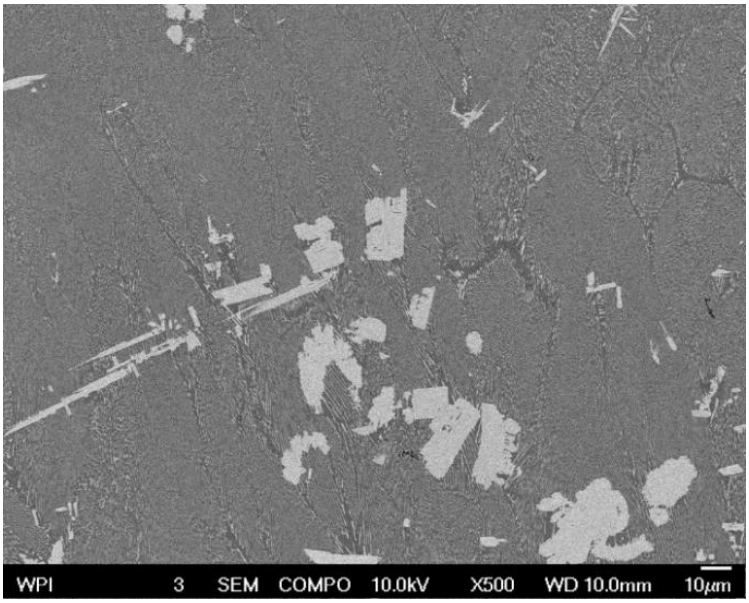

(a)

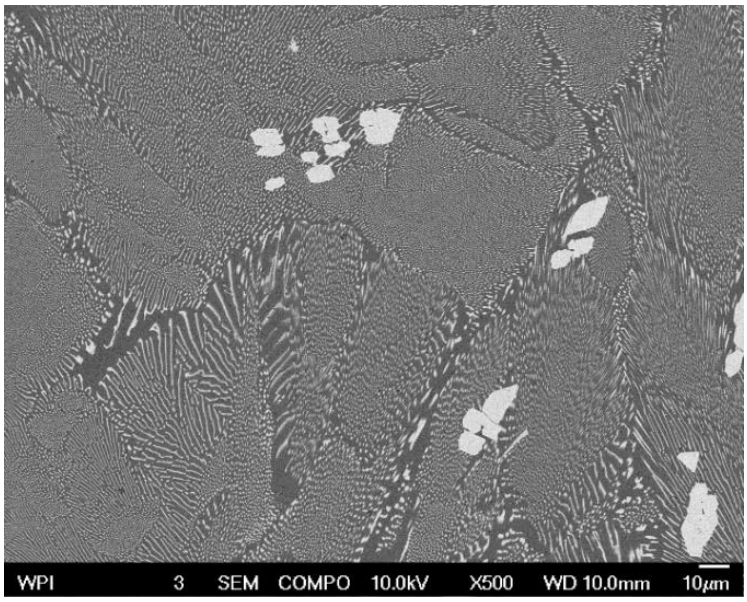
WPI 3 SEM COMPO 10.0kV X500 WD 10.0mm 10μm

(b)

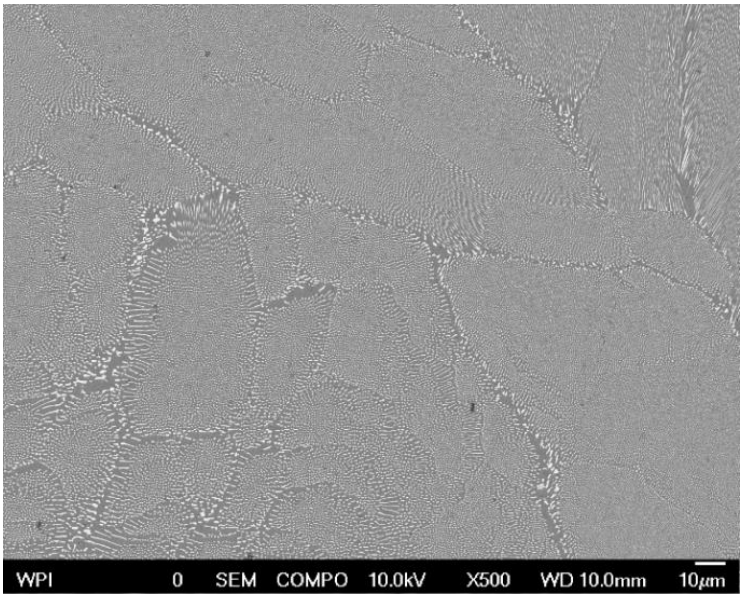
WPI 0 SEM COMPO 10.0kV X500 WD 10.0mm 10μm

(c)


WPI 3 SEM COMPO 10.0kV X500 WD 10.1mm 10μm

(d)

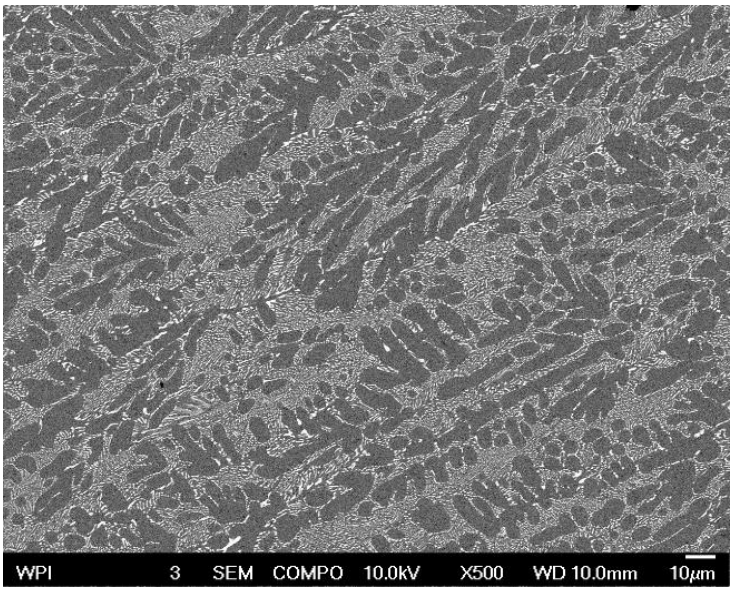
WPI 3 SEM COMPO 10.0kV X500 WD 10.0mm 10μm

(e)

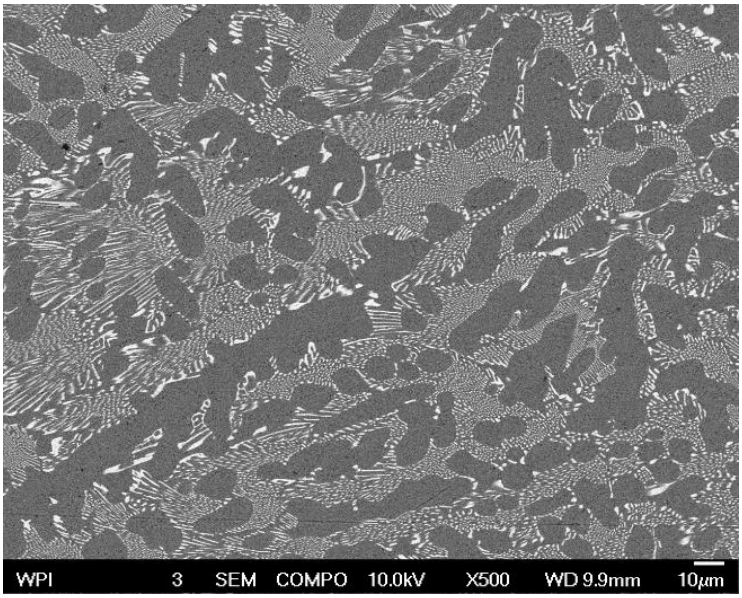

(f)

Fig. 6 SEM photomicrographs of Al-Ni-Mn alloys cast with 90°C/s cooling rate. (a) Al-6Ni-4Mn, (b) Al-6Ni-3Mn, (c) Al-6Ni-2MN, (d) Al-4Ni-4Mn, (e) Al-4Ni-3Mn, (f) Al-4Ni-2Mn.

Solidification sequence in Al-Ni-Mn alloys – Since formation of the *O* phase may be suppressed by employing a high cooling rate, then the *O* phase must be a primary phase. However, if the alloy is cooled *rapidly* from the pouring temperature (800°C) to the eutectic temperature, the *O* phase does not have sufficient time to nucleate and grow in the liquid. Fig. 7 is a schematic depiction based on the information presented in Fig. 4 and shows a non-equilibrium phase diagram for the Al-Ni-Mn system. This simple schematic illustrates the correct choice of cooling rates during solidification in order to ensure complete introduction of manganese into supersaturated solid solution during solidification. Neither the primary α-Al phase nor the primary Al_3Ni phase are present

in Al-6Ni-Mn alloys, therefore these alloys lie in an Al-Al_3Ni eutectic trough. Extrapolation of this eutectic trough in the direction of the Al-Ni binary composition leads to the Al-6.1Ni eutectic point. Al-4Ni-Mn alloys, on the other hand, do form the primary α-Al phase prior to forming the Al-Ni eutectic structure. The presence of *O* phase in the microstructure depends to a large extent on the cooling rate during solidification. The dashed lines in Fig. 7 indicate the limiting cooling rate for formation of *O* phase in the different alloy compositions; and the *O* phase forms on the concave side of these dashed lines. Obviously, a higher cooling rate during solidification allows introduction of more Mn in solid solution; i.e., the dashed lines move towards the Mn rich region of the diagram with increasing cooling rate.

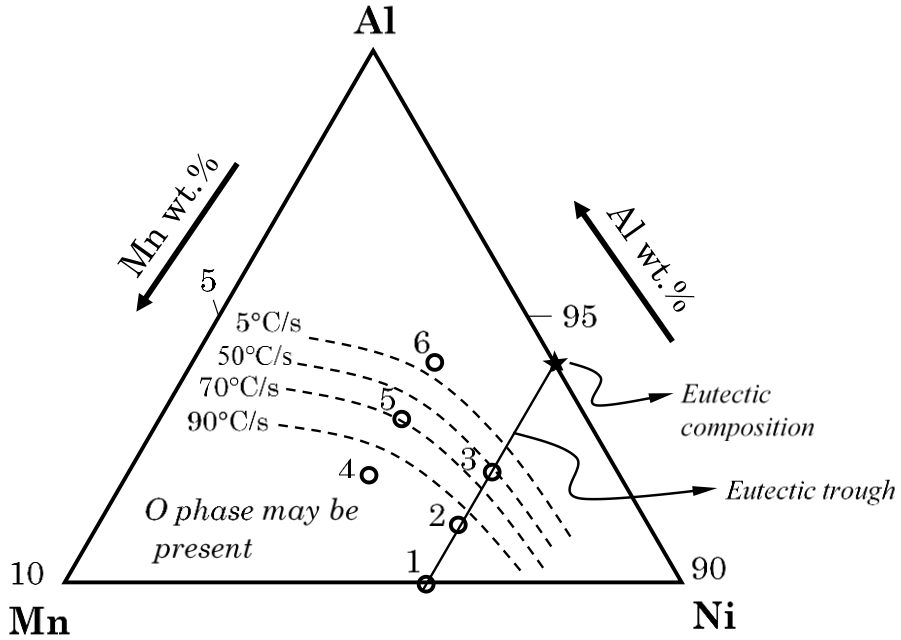

Fig. 7 A schematic depiction of a non-equilibrium phase diagram for the Al-Ni-Mn system. Alloy 1 is Al-6Ni-4Mn alloy; alloy 2 is Al-6Ni-3Mn alloy; alloy 3 is A-6Ni-2Mn alloy; alloy 4 is Al-4Ni-4Mn alloy; alloy 5 is Al-4Ni-3Mn alloy; and alloy 6 is Al-4Ni-2Mn alloy.

Precipitation strengthening in Al-Ni-Mn alloys – Fig. 8 shows the response of Al-6Ni-4Mn alloy that is solidified with 90°C/s cooling rate to aging at 400°C and 450°C. The maximum yield strength is attained after 1.5 hours at the 400°C aging temperature and after 1.0 hour at the 450°C aging temperature. As illustrated in Fig. 4, the fast solidification cooling rate mitigates formation of the *O* phase and thus it allows a relatively large fraction of the Mn to be retained in an *ultra*-supersaturated solid solution with Al. The as-cast yield strength of Al-6Ni-4Mn alloy is measured to be about 140 Mpa. Subsequent aging of the alloy causes Mn-containing precipitates to form in the alloy and almost double its yield strength.

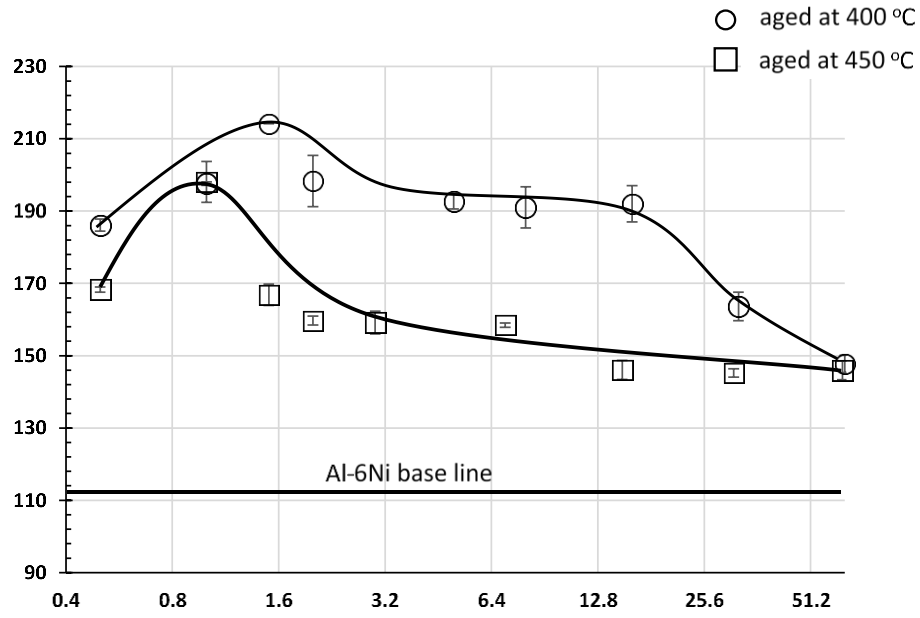

Fig. 8 Variation of the yield strength with aging time for Al-6Ni-4Mn alloy solidified with 90°C/s cooling rate and aged at 400°C and 450°C.

Fig. 9 shows SEM photomicrographs of the Al-6Ni-4Mn alloy solidified with 90°C/s cooling rate and it clearly demonstrates the effect of aging on the microstructure of this alloy. The strength-inducing precipitates form along the grain boundaries. Fig. 10 is a composite TEM micrograph of the Al-6Ni-4Mn sample solidified with 90°C/s cooling rate and aged at 450°C for 2 hours. The photomicrograph on the right side of the dashed line is taken within a grain boundary and the photomicrograph on the left side of the dashed line is taken within a grain. The particles in the grain boundary have an elliptical cross section with an average major axis equal to 350 nm and an average minor axis equal to 200 nm. A selected area diffraction pattern (SADP) taken from these particles is shown in Fig. 11 and confirms that they are indeed Al_6Mn precipitates that are aligned with the [111] zone axis and have an orthorhombic crystal structure with lattice parameters a = 0.76 nm, b = 0.65 nm, and c = 0.89 nm. Energy dispersive spectroscopy (EDS) was used to measure the concentration of Mn across several grains in as-cast alloy samples of Table I (Fig. 12). The measurements did not reveal any severe segregation of Mn in the neighborhood of grain boundaries, which suggests the following plausible scenario for why precipitation of the Al_6Mn particles occurs at the grain boundaries preferentially to within the grains.

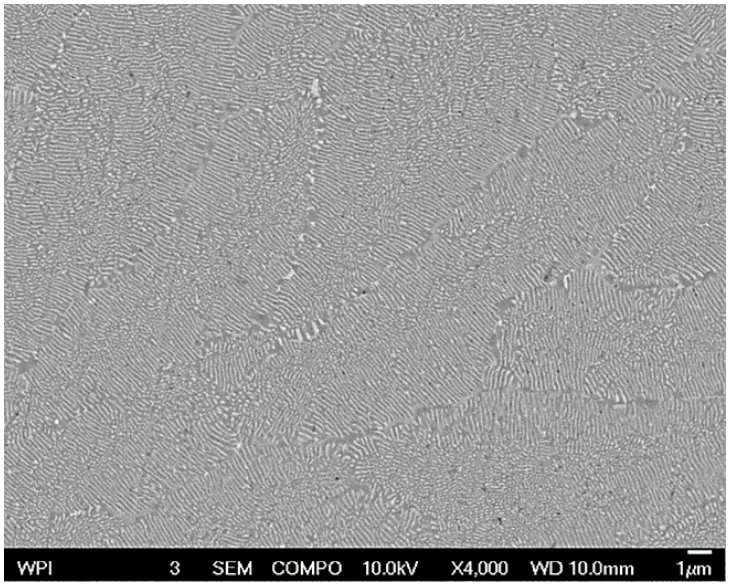

(a)

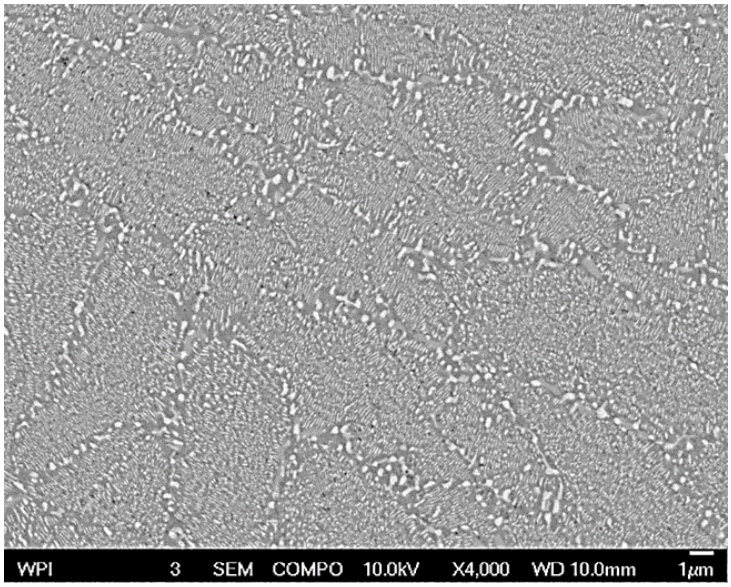

(b)

Fig. 9 SEM photomicrograph of the Al-6Ni-4Mn sample solidified with 90°C/s cooling rate. (a) as-cast microstructure, and (b) aged at 450°C for 2 hours.

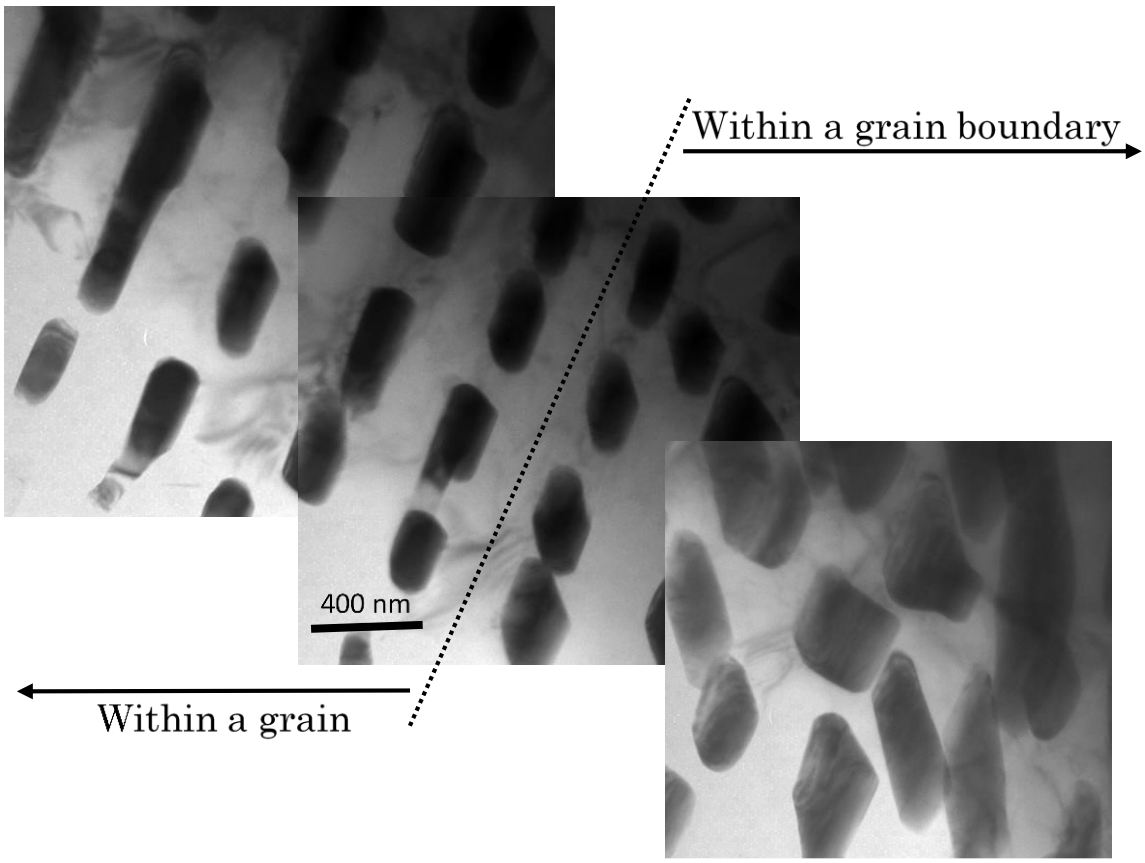

Fig. 10 Composite TEM micrograph of the Al-6Ni-4Mn sample solidified with 90°C/s cooling rate and aged at 450°C for 2 hours.

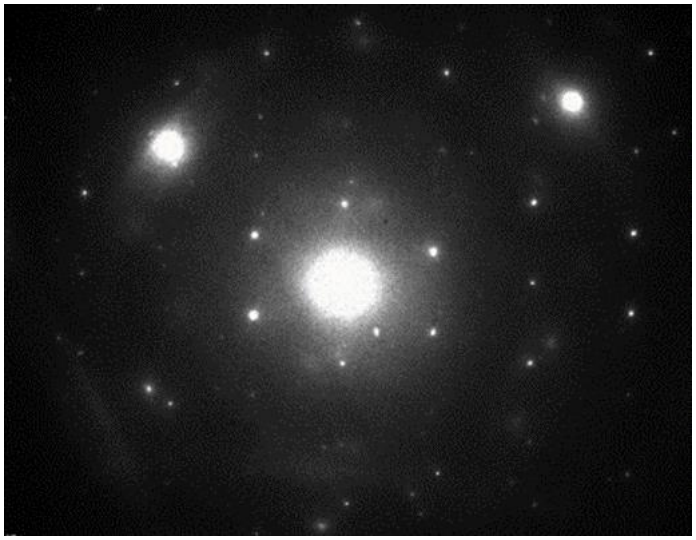

Fig. 11 Selected area diffraction pattern (SADP) from particles in the grain boundary of an Al-6Ni-4Mn sample solidified with 90°C/s cooling rate and aged at 450°C for 2 hours. The particles are Al_6Mn aligned with the [111] zone axis.

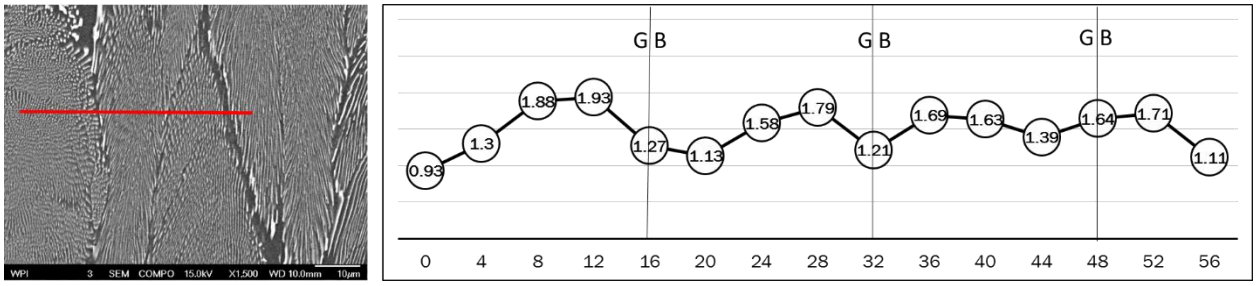

(a)

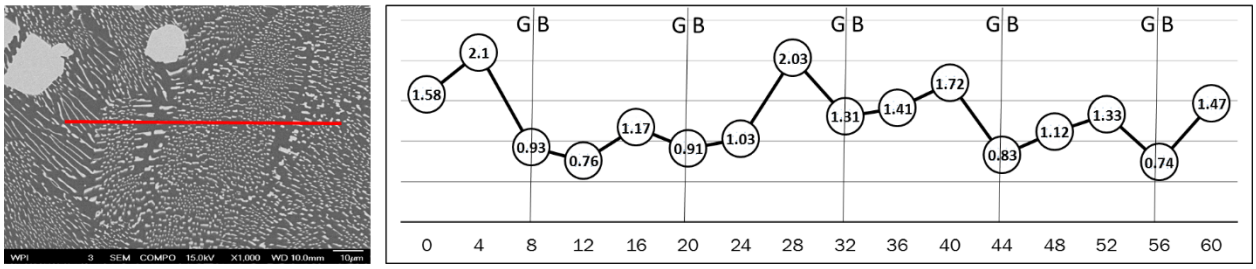

(b)

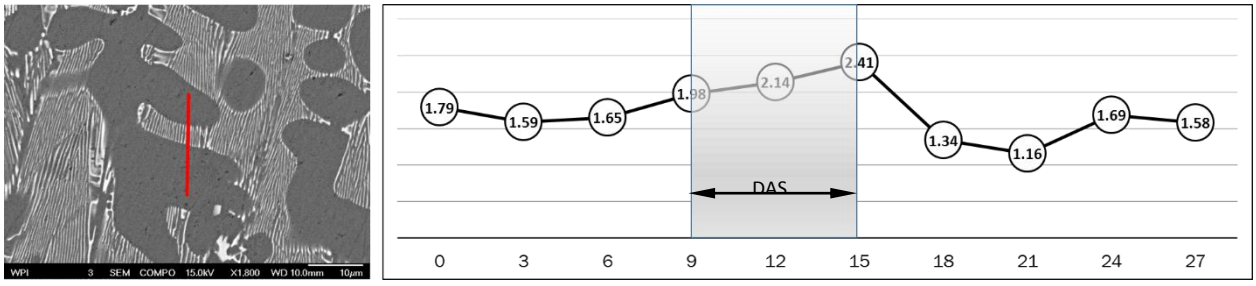

(c)

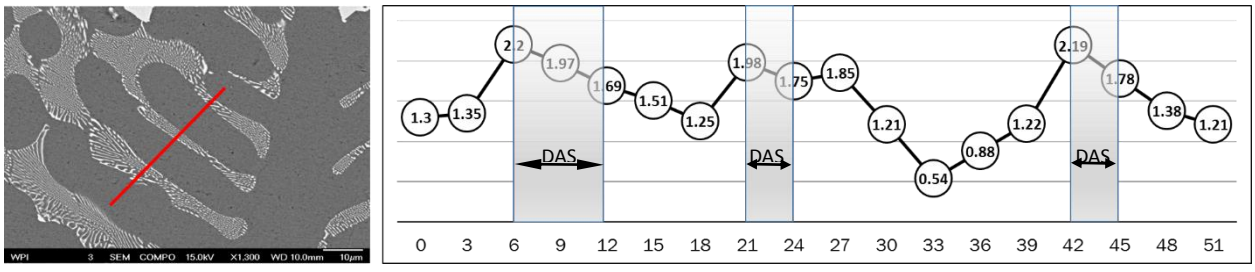

(d)

Fig. 12 Manganese concentration in wt% in the neighborhood of typical grain boundaries of as-cast (a) Al-6Ni-4Mn alloy cooled at 90°C/s, (b) Al-6Ni-4Mn alloy cooled at 5°C/s,
(c) Al-4Ni-4Mn alloy cooled at 90°C/s, and (d) Al-4Ni-4Mn alloy cooled at 5°C/s. Shaded regions on the plots locate space between dendrite arms (i.e., DAS).

Thermodynamics dictate that the energy barrier for heterogeneous nucleation (i.e., nucleation on grain boundaries) is lower than the energy barrier for homogeneous nucleation (i.e., nucleation within grains) [20]. Nucleation at grain boundaries is especially favored when the chemical driving force is low and, at the same time the ratio between the grain boundary energy and that of the nucleus/bulk interface is high. After the Al_6Mn nucleus has formed, and given the fact that the self-diffusion coefficient at grain boundaries is usually higher than in the bulk, the Mn atoms will rapidly migrate towards the Al_6Mn nucleus within the grain boundary. The relatively high precipitate density at the grain boundaries may be explained by considering the effect of a high flux of vacancies into and along the grain boundary on the nucleation rate. Quenched-in vacancies that form due to the fast cooling rate from the melt temperature greatly increases the rate at which atoms diffuse at the aging temperature and, apart from dislocations, the main sinks for these excess vacancies are the grain boundaries. This high vacancy flux could increase the nucleation rate of precipitates through its effect on the rate at which single atoms add onto the critical nucleus (i.e., the frequency factor). The fact that Al_6Mn precipitates form in the grain boundaries is particularly important because the precipitates appreciably modify the response of the alloy to various stimuli, including heat. Susceptibility of the alloy to corrosion is also affected as the areas neighboring the

precipitate particles become depleted in Mn and therefore they constitute local electrochemical cells. Grain boundary precipitation has been observed in many aluminum alloys, e.g., Al-Cu [21], and Al-Zn-Mn [22]. Fig. 12 shows that coring occurs in the hypoeutectic alloys, particularly when they are solidified with a slow cooling rate (e.g., 5°C/s); and, although chemical compositions measured by EDS are generally not precise, it is evident that irrespective of alloy composition, more Mn is retained in the super saturated solid solution when the alloy is solidified with a high cooling rate (e.g., 90°C/s).

Close examination of the alloy's microstructure near grain boundaries shows that the eutectic Al_3Ni extend to within a few nanometers from the grain boundary (Fig. 13). Although technically speaking this is not a precipitate free zone (PFZ) since the Al_3Ni eutectic are a product of a eutectic reaction and not a precipitation reaction, the consequences are similar to those attributed to a PFZ; i.e., the lack of a PFZ may significantly increase the yield strength of a precipitation hardened alloy [23]. In the alloys of Table I, the regions neighboring the grain boundaries are strengthened by the eutectic Al_3Ni.

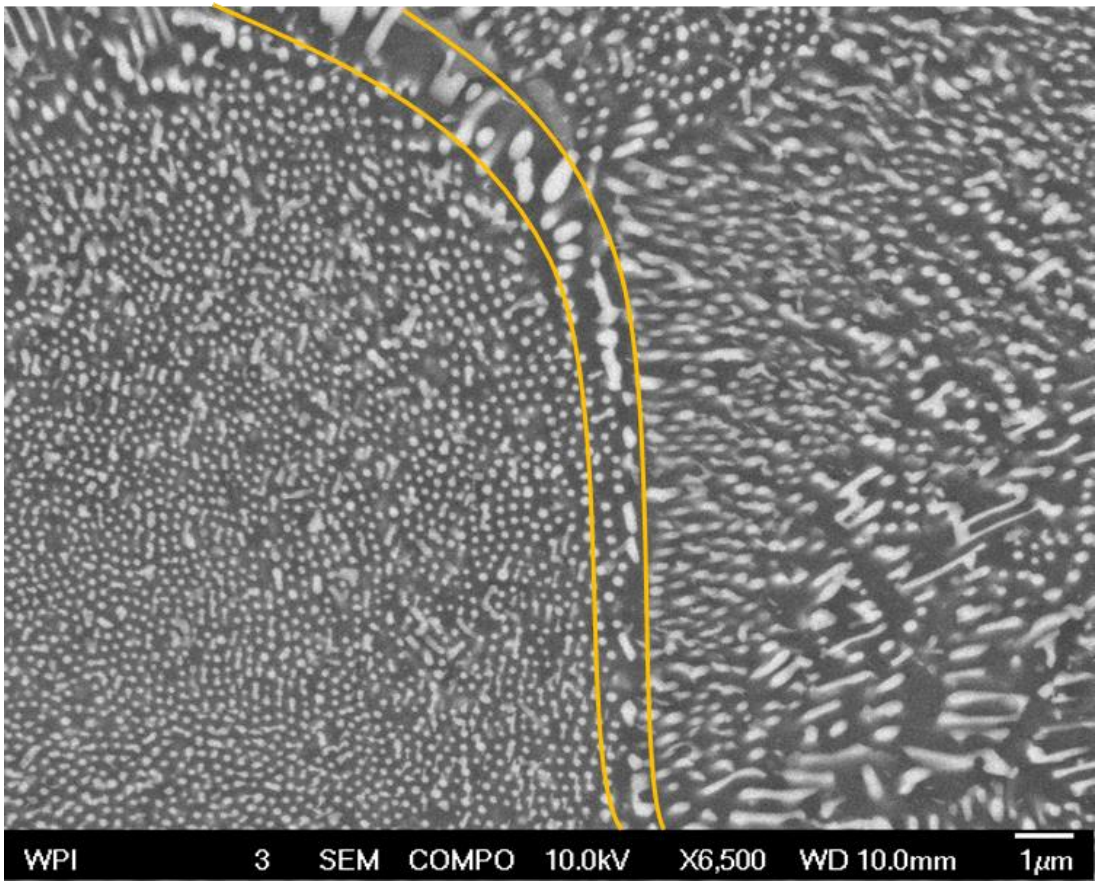

Fig. 13 High magnification photomicrograph of Al-6Ni-4Mn alloy cooled at 90°C/s. Lines delineate two adjacent grains.

The room temperature yield strength of alloys with the compositions shown in Table I, solidified with 90°C/s cooling rate and aged at 450°C for 1 hour was measured. The results are presented in Table II. Also shown in Table II is the yield strength of Al-6Ni-4Mn alloy solidified with 90°C/s cooling rate, aged at 450°C for 1 hour, and measured at 300°C[4]. As expected, the room temperature yield strength of Al-Ni-Mn alloys decreases with decreasing Mn content; and, for the same Mn content, the yield strength of Al-6Ni-*x*Mn alloys is higher than that of Al-4Ni-*x*Mn

[4] Samples were soaked at 300°C in an electric box furnace for 100 hours and then pulled at 300°C.

alloys. This is attributed mainly to the larger volume fraction of Al_3Ni eutectic in the Al-6Ni-*x*Mn alloys. Al-Ni-Mn alloys in general have excellent elevated temperature tensile properties as demonstrated by the Al-6Ni-4Mn alloy, which has a 130MPa yield strength at 300°C compared to 124 MPa at 260°C for die cast A390 aluminum alloy [10].

Table II 0.2% offset yield strength of alloys with the compositions shown in Table I.

Alloy Composition (wt. %)	Temperature (°C)	0.2% offset Yield strength (MPa)
Al-6Ni-4Mn	25	198
Al-6Ni-3Mn	25	169
Al-6Ni-2Mn	25	163
Al-4Ni-4Mn	25	153
Al-4Ni-3Mn	25	149
Al-4Ni-2Mn	25	131
Al-6Ni-4Mn	300	130

It can be deduced from Fig. 4 that a maximum of three phases may be present in the as-cast Al-Ni-Mn alloys of this study; namely (i) the supersaturated α-Al phase, (ii) the Al_3Ni phase, and (iii) the *O* phase. The Ni and Mn contents of the alloy are divided among these 3 phases. So, applying a mass balance yields

$$m_{Ni} = \frac{\rho_o f_o \frac{4M_{Ni}}{M_{Al_{60}Mn_{11}Ni_4}} + \rho_{Al_3Ni} f_{Al_3Ni} \frac{M_{Ni}}{M_{Al_3Ni}}}{\rho_o f_o + \rho_{Al_3Ni} f_{Al_3Ni} + \rho_{Al}(1 - f_o - f_{Al_3Ni})} \tag{11}$$

from which

$$f_{Al_3Ni} = \frac{\rho_o f_o \frac{4M_{Ni}}{M_{Al_{60}Mn_{11}Ni_4}} - m_{Ni}\rho_o f_o - m_{Ni}\rho_{Al} + f_o m_{Ni}\rho_{Al}}{m_{Ni}\rho_{Al_3Ni} - m_{Ni}\rho_{Al} - \rho_{Al_3Ni}\frac{M_{Ni}}{M_{Al_3Ni}}} \tag{12}$$

and

$$m_{Mn} = \frac{\rho_o f_o \frac{11 M_{Mn}}{M_{Al_{60}Mn_{11}Ni_4}} + \varphi_{Mn}}{\rho_o f_o + \rho_{Al_3Ni} f_{Al_3Ni} + \rho_{Al}(1 - f_o - f_{Al_3Ni})} \quad (13)$$

from which

$$\varphi_{Mn} = m_{Mn}\left[\rho_o f_o + \rho_{Al_3Ni} f_{Al_3Ni} + \rho_{Al}\left(1 - f_o - f_{Al_3Ni}\right)\right] - \rho_o f_o \frac{11 M_{Mn}}{M_{Al_{60}Mn_{11}Ni_4}} \quad (14)$$

where f_o may be determined from area fraction measurements.

Upon aging, the yield strength of the Al-Ni-Mn alloy derives from its volume fraction of Al_3Ni eutectic (f_{Al_3Ni}) and volume fraction of Al_6Mn precipitate particles(f_{Al_6Mn}). f_{Al_3Ni} is calculated from (12), and φ_{Mn} is calculated from (14) and then used in (15) to calculate f_{Al_6Mn} by assuming that all the Mn content of the alloy is consumed in forming the Al_6Mn phase,

$$f_{Al_6Mn} = \varphi_{Mn} * \frac{M_{Al_6Mn}}{M_{Mn}} / \rho_{Al_6Mn} \quad (15)$$

Fig. 14 shows the change in volume fraction of the Al_3Ni eutectic and the Al_6Mn precipitate particles with solidification cooling rate. It is calculated by employing the appropriate values for the various parameters in (12) and (15), respectively.

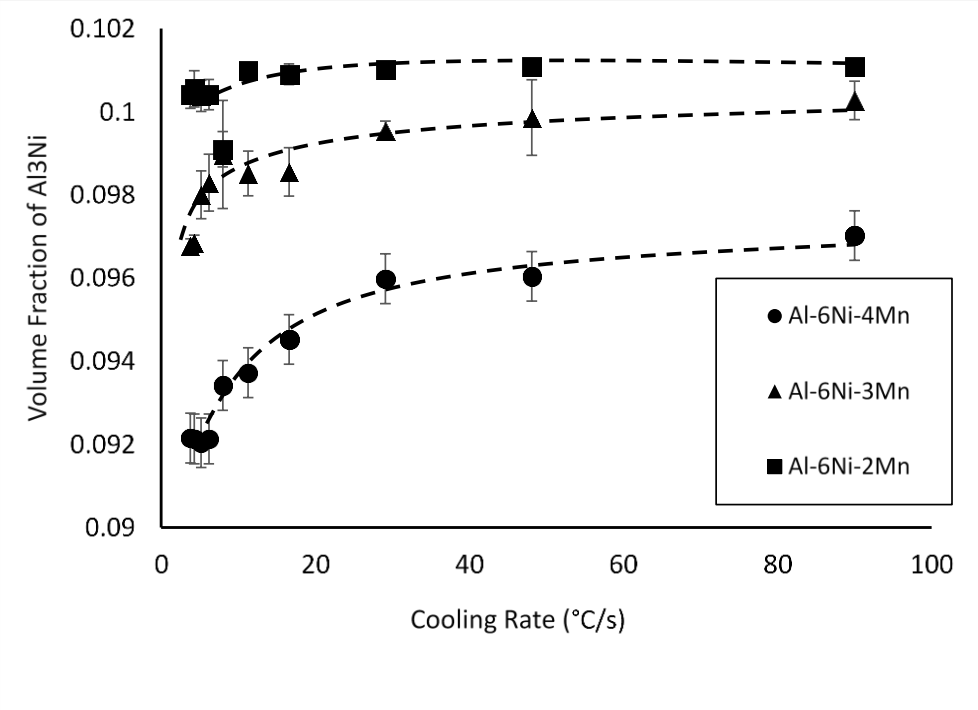
0.102
0.1
0.098
0.096
0.094
0.092
0.09
Volume Fraction of Al3Ni
0
20
40
60
80
100
Cooling Rate (°C/s)
Al-6Ni-4Mn
Al-6Ni-3Mn
Al-6Ni-2Mn

(a)

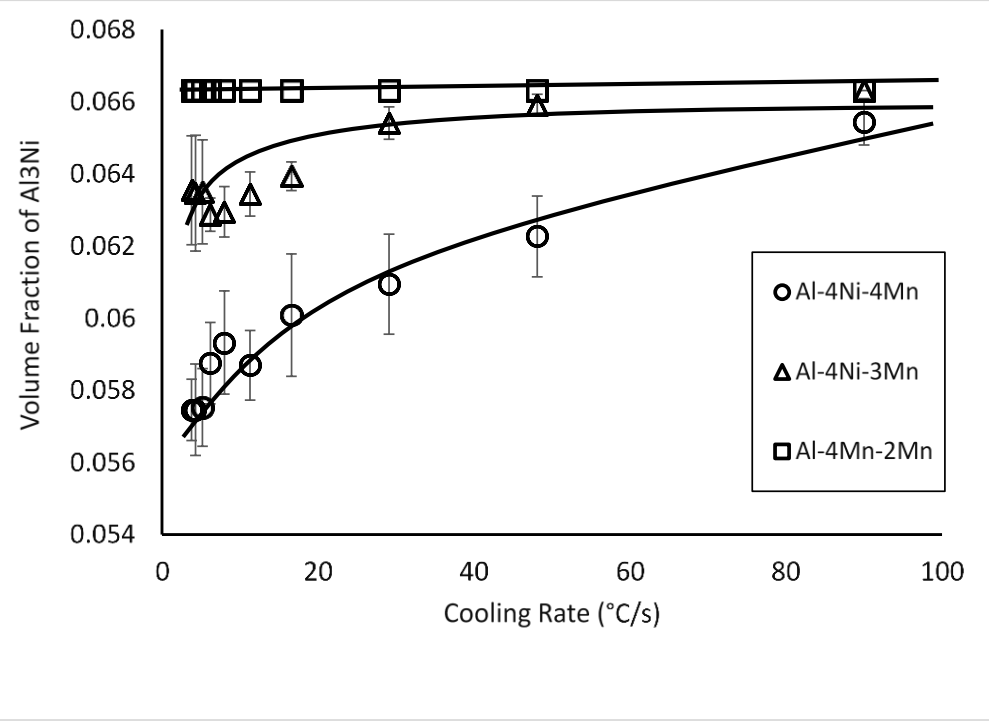
0.068
0.066
0.064
0.062
0.06
0.058
0.056
0.054
Volume Fraction of Al3Ni
0
20
40
60
80
100
Cooling Rate (°C/s)
Al-4Ni-4Mn
Al-4Ni-3Mn
Al-4Mn-2Mn

(b)

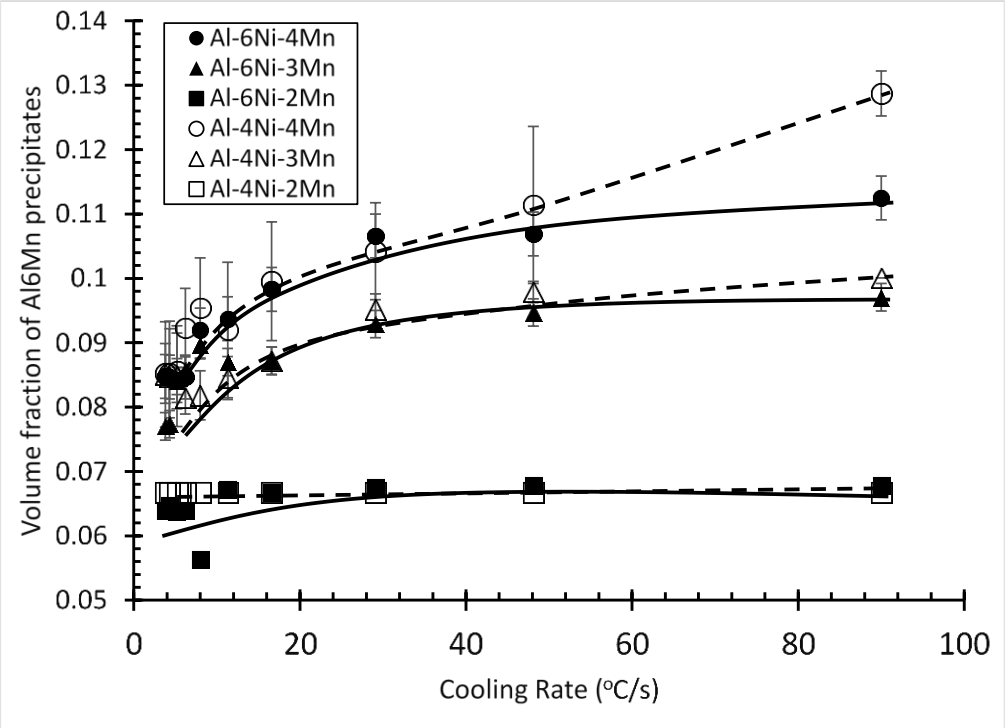

(c)

Fig. 14 Calculated curves showing the change in volume fraction with solidification cooling rate due to (a) the Al_3Ni fibers in Al-6Ni-*x*Mn alloys, (b) the Al_3Ni fibers in Al-4Ni-*x*Mn alloys, (c) the Al_6Mn precipitate particles in Al-6Ni-*x*Mn and Al-4Ni-*x*Mn alloys.

Similarly, Fig. 15 shows the change in yield strength increment with solidification cooling rate due to the presence of the Al_3Ni eutectic and Al_6Mn precipitate particles, respectively. These curves are calculated by employing the appropriate values for the various parameters in (8) and (9), respectively together with the average measured values for the radius of the Al_3Ni eutectic (50 nm), the major and minor axes of the Al_6Mn particle (350 nm and 200 nm, respectively). Fig. 16 shows the change in total yield strength of the various Al-Ni-Mn alloys of this study with solidification cooling rate. It is calculated by employing the

appropriate values for the various parameters in (10). Close examination of Fig. 16 reveals that the volume fraction of the Al_3Ni eutectic is the most important strengthening factor in Al-Ni-Mn alloys. All the Al-6Ni-*x*Mn alloys have higher yield strength than Al-4Ni-*x*Mn alloys do. Moreover, a higher Mn content (4 wt.% vs. 3 wt.%) is more desirable for alloy strength, but only when solidification cooling rate > 16°C/s for Al-6Ni-*x*Mn alloys, and > 30°C/s for Al-4Ni-*x*Mn alloys. A lower Mn content (2 wt.%) produces alloys with inferior yield strength with all the solidification cooling rates investigated, and this is true for both Al-6Ni-*x*Mn and Al-4Ni-*x*Mn alloys.

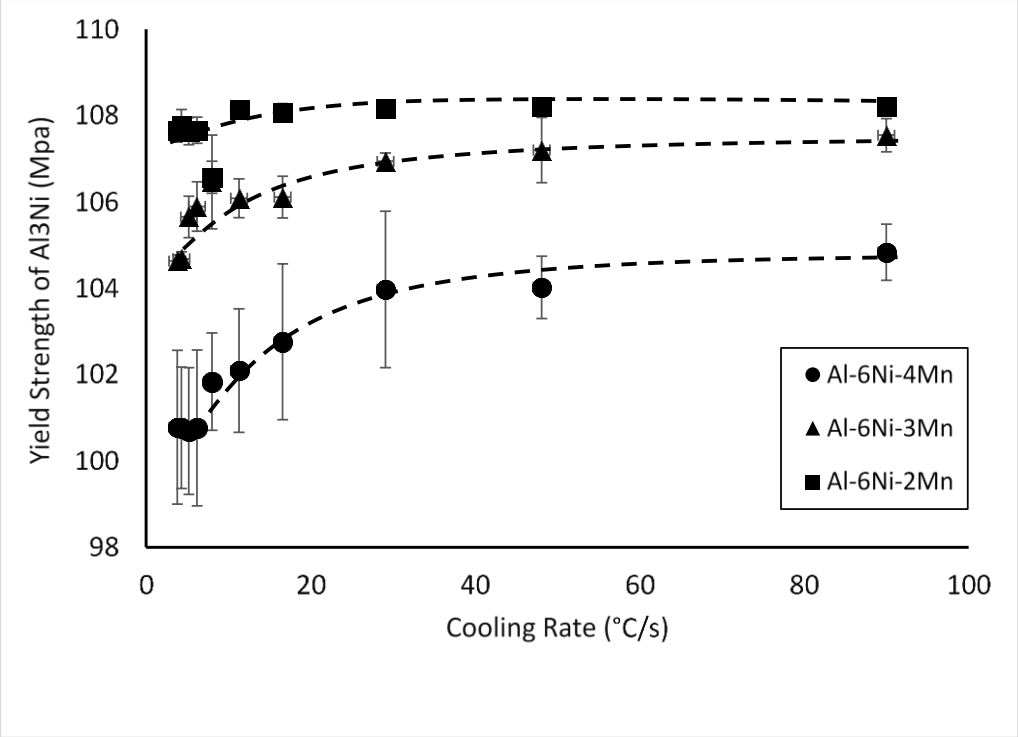

(a)

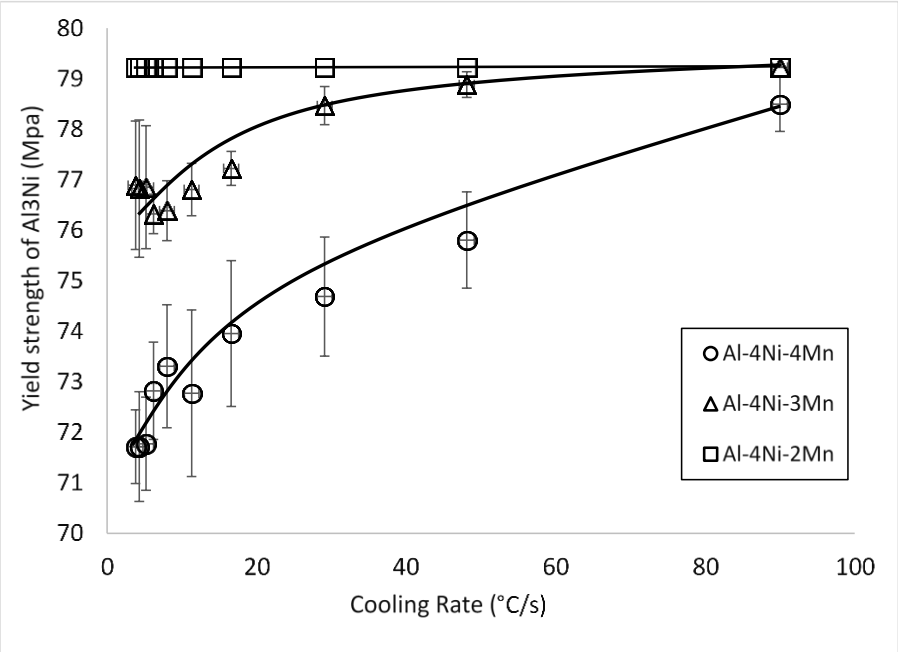

(b)

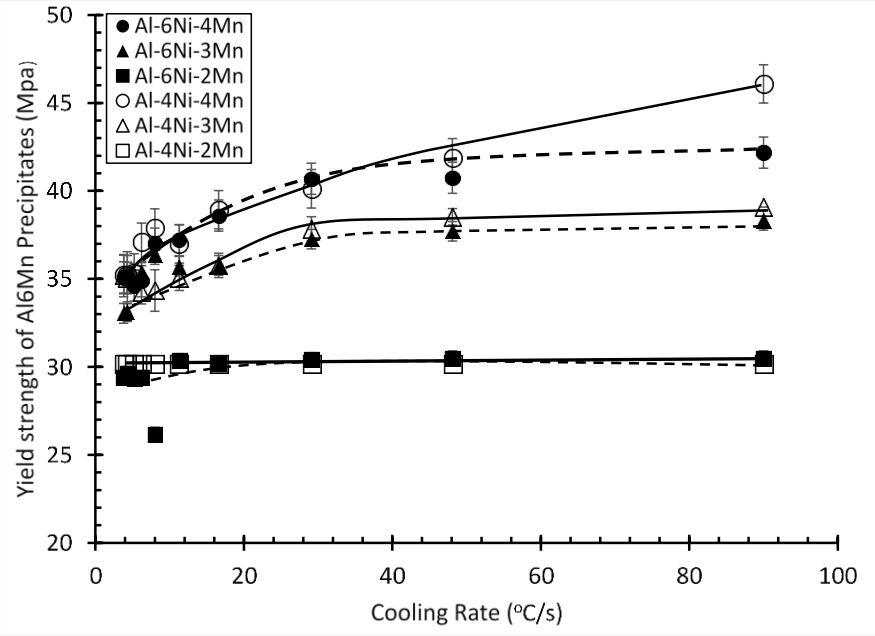

(c)

Fig. 15 Calculated curves showing the change in yield strength of the alloys with solidification cooling rate due to (a) the Al_3Ni fibers in Al-6Ni-*x*Mn alloys, (b) the Al_3Ni fibers in Al-4Ni-*x*Mn alloys, (c) the Al_6Mn precipitate particles in Al-6Ni-*x*Mn
And Al-4Ni-*x*Mn alloys.

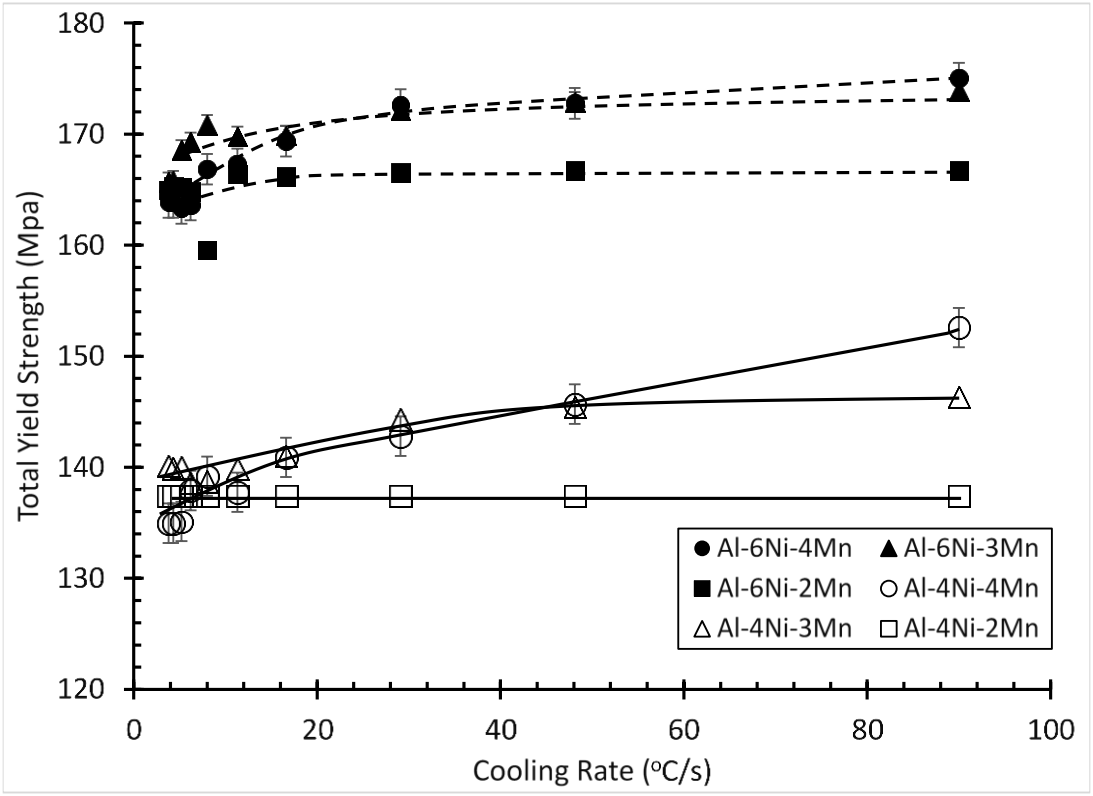

Fig. 16 Calculated curves showing the change in total yield strength of the alloys with solidification cooling rate.

Table III shows the measured and calculated yield strengths for the Al-Ni-Mn alloys of this study. The calculated values for yield strength are very close to the measured values, which validates the model equations. An important simplifying assumption was made when applying the model equations and it may have contributed to the small discrepancy between the measured and the calculated values: Variations in the nucleation and growth kinetics of the Al_6Mn precipitate particles with the manganese and/or nickel content of the alloy was neglected, as a result the Al_6Mn precipitate particles are taken to be of the same average size irrespective of alloy composition. The somewhat large difference

(14%) between the measured and calculated yield strength of the Al-6Ni-4Mn alloy may be attributed to the significant amount of *O* phase that forms in this alloy and is not accounted for in the mathematical model.

Table III. Measured and calculated yield strength values of alloys with the compositions depicted in Table I.

Alloy Composition (wt. %)	Measured yield strength (MPa)	Calculated yield strength (MPa)
Al-6Ni-4Mn	198	175.0
Al-6Ni-3Mn	169	173.9
Al-6Ni-2Mn	163	166.7
Al-4Ni-4Mn	153	152.6
Al-4Ni-3Mn	149	146.3
Al-4Ni-2Mn	131	137.4

CONCLUSIONS

1) Because the equilibrium solubility of manganese in solid aluminum is small, the maximum volume fraction of Al_6Mn precipitate that may form in aluminum by a typical heat treatment regimen is limited; consequently, the strengthening increment attained by the presence of the Al_6Mn phase is limited. A 'non-traditional' heat treatment regimen is proposed whereby the molten alloy is cast at a high cooling rate (~90°C/s) so that an ultra-supersaturated solid solution of manganese in aluminum is obtained directly from the melt. In alloys with the eutectic composition (i.e., Al-6Ni-*x*Mn alloys), the fast cooling preserves the homogeneous solid solution formed at the melting

temperature. However, in hypoeutectic alloys (e.g., Al4Ni-*x*Mn alloys), some coring occurs, particularly in the slowly cooled (5°C/s) alloys.

2) A high cooling rate during solidification suppresses formation of the *O* phase in Al-Ni-Mn alloys leaving more of the manganese to partake in precipitation strengthening. On the other hand, elevated manganese and nickel contents promote formation of the *O* phase.

3) Al_6Mn particles precipitate predominantly within the grain boundaries. Since no preferential segregation of manganese around grain boundaries was detected, it is stipulated that the relatively high precipitate density at the grain boundaries is due to the high flux of vacancies into and along the grain boundaries. This high vacancy flux increases the nucleation rate of the Al_6Mn precipitate by increasing the frequency at which atoms add onto the critical nucleus.

4) A mathematical model is developed and used to calculate the strengthening increment contributed by each of the phases present in the aged Al-Ni-Mn alloys. The model predicts that the larger part of the alloy's yield strength is due to the Al_3Ni eutectic phase.

5) The mathematical model suggests that the total yield strength of Al-Ni-Mn alloys with compositions within the investigated range is the linear sum of the strengthening increments contributed by the α-Al phase, the Al_3Ni eutectic phase, and the Al_6Mn precipitate particles.

6) The measured room temperature yield strength of Al-6Ni-4Mn alloy solidified at 90°C/s and aged 400°C for 1.5 hours is around 200 MPa and its measured yield strength at 300°C is 130 MPa, which compares very favorably with commercial aluminum alloys.

7) The model-predicted room temperature yield strength values of the Al-Ni-Mn alloys with compositions within the investigated range compare very well with the measured values.

REFERENCES

1. H.J. Frost and M.F. Ashby: Deformation mechanism maps, Pergamon Press, Oxford, 1982.
2. M.A. Meyers, K.K. Chawla, Mechanical Metallurgy: Principles and Applications, Paramus, Englewood Cliffs, NJ, 1984.
3. A. Melander and P.A. Persson: Acat Metall., 1978, vol. 25, pp.267-78.
4. W.B. Pearson: Handbook of Lattice Spacing and Structures of Metals and Alloys Volume 2, Pergamon Press, Ottawa, 1967, pp. 122-23.
5. Properties of Wrought Aluminum and Aluminum Alloys, Properties and Selection: Nonferrous Alloys and Special-Purpose Materials, ASM Handbook, Vol. 2, ASM International, 1990, pp. 62-122.

6. T. Koutsoukis and M. M. Makhlouf: Proceedings of 115th TMS Annual Meeting, Orlando, Florida, 2015.
7. A.R. Cooke and J.W. Martin: J. of Mater. Sci., 1976, vol. 11, pp. 665-69.
8. YY. Fan and M.M. Makhlouf: Proceedings of the Light Metals Technology Conference, Old Windsor, UK, 2013, pp. 8-12.
9. T. Koutsoukis and M.M. Makhlouf: AFS Transactions, April, 2015, paper no. 15-089.
10. A.L. Kearney: Properties of Cast Aluminum Alloys, Properties and Selection: Nonferrous Alloys and Special-Purpose Materials, vol. 2, ASM Handbook, ASM International, 1990, pp. 152–77.
11. D. Shechtman, R.J. Schaefer, and F.S. Biancaniello: Metall. Trans. A, 1984, vol. 15, pp. 1987-97.
12. Yong Dua, Y.A. Changb, and Baiyun Huanga, etc.: Metal. Sci. and Eng. A, 2003, vol. 363, pp. 140-51.
13. L.M. Rylands and D.M.J. Wilkes, and W.M. Rainforth, etc.: J. of Mater. Sci., 1994, vol. 29, pp. 1895-00.
14. A.J. McAlister and J.L, Murray: Bulletin of Alloy Phase Diagram, 1987, vol. 8, pp. 385-92.
15. M.F. Ashby: Oxide Dispersion Strengthening, Gordon and Breach, Science Publishers, New York, London, Pairs, 1966, pp. 143-212.

16. H.B. Smartt, L.K. Tu, and T.H. Courtney: Metall. Trans., 1971, vol. 2, pp. 2717-27.
17. B. Cantor and G.A. Chadwick: J. of Mater. Sci., 1975, vol. 10, pp. 578-88.
18. P.M. Kelly: Int. Metall. Rev., 1973, vol. 18, pp. 31-36.
19. S. Balanetskyy, G. Meisterernst, and B. Grushko, etc.: J. of Alloys and Comp., 2011, vol. 509, pp. 3795-05.
20. D.A. Porter and K.E. Easterling: Phase Transformation in Metals and Alloys, 3 nd ed., CRC Press, 2009.
21. D. Vaughan: Acta Metall., 1968, vol. 16, pp. 563-77.
22. P.N.T. Unwin and R.B. Nicholson: Acta Metall., 1969, vol. 11, pp. 1379-93.
23. C.T. Liu, C.L. White, and J.A. Horton: Acta Metall., 1985, vol. 33, pp.213-29.

Chapter 4

Precipitation Strengthening in Aluminum-Zirconium-Vanadium Alloys

Yangyang Fan*, Jenifer Barrirero **, and Makhlouf M. Makhlouf*
*Department of Mechanical Engineering, Worcester Polytechnic Institute, Worcester, MA 01609, USA
** Material Engineering Center, Saarland University Saarbrücken, D-66123, Germany

Keywords: $Al_3(Zr,V)$, Atom probe tomography (APT), anti-phase boundary energy.

ABSTRACT

$Al_3(Zr_{1-x}V_x)$Atom probe tomography (APT) and aberration corrected HRTEM were used to study the co-precipitation and coarsening mechanisms of $Al_3(Zr_{1-x}V_x)$ precipitates formed in Al-Zr alloys with various Zr;V ratio. Also, the strengthening mechanism that is operative in properly aged Al-Zr-V alloys are determined, and the antiphase boundary (APB) energies between the aluminum matrix and the Al_3Zr and $Al_3(Zr_{1-x}V_x)$ precipitates were indirectly determined.

1. INTRODUCTION

Extensive work has been performed on alloying aluminum with transition metals (TM) particularly scandium [1, 2] and zirconium [3-6], and combinations of scandium and zirconium [7-18]; because, upon

proper heat-treatment of the alloy, these elements tend to form precipitates that have the chemical composition Al_3TM and the $L1_2$ crystal structure. These precipitates tend to be thermally stable, and when they are present in large volume fractions, they significantly increase the high temperature yield strength of aluminum alloys [2, 18-21]. For these reasons, Al-TM alloys are often thought of as excellent candidates for high temperature applications [19]. However, the strength of Al-Sc alloys deteriorates when they are used at temperatures above 300°C [19]. This is mainly due to the high diffusivity of scandium in aluminum at these temperatures ($D_{sc} = 1.98\times10^{-17}$ m^2/s at 400°C [22]) and the low thermal stability of the Al_3Sc phase at temperature above 300°C.

The $L1_2$-Al_3Zr phase is more thermally stable than the $L1_2$-Al_3Sc phase at elevated temperatures. And many studies have attempted to further stabilize it by alloying it with V to form co-precipitates of the general formula $Al_3(Zr_{1-x}V_x)$ [23-25]. For example, Fine [25] and Chen [23, 24] reported that by adding V to Al-Zr alloys, the coarsening rate of the precipitates that form is significantly lowered. Fine [25] attributed this phenomenon to a lowering of the lattice parameter mismatch between the precipitate particles and the aluminum matrix upon adding V. However, details of the mechanism of formation of the $Al_3(Zr_{1-x}V_x)$ co-precipitate remains unclear.

In this study, we employed atom probe tomography (APT) and aberration

corrected HRTEM to study the co-precipitation and coarsening mechanisms of $Al_3(Zr_{1-x}V_x)$ precipitates formed in Al-Zr alloys with various Zr:V ratio. Moreover, we define the strengthening mechanism that is operative in these Al-Zr-V alloys, and we determine – albeit indirectly – the Al-Al_3Zr and Al-$Al_3(Zr_{1-x}V_x)$ antiphase boundary (APB) energies.

2. MATERIALS AND PROCEDURES

2.1 Alloy preparation and heat-treatment

The Al-Zr-V alloys shown in Table I were constituted from pure aluminum ingots (99.99% purity), and Al-65wt.%V and Al-15wt.%Zr master alloys. The alloys were melted in air in an induction furnace in clean silicon carbide crucibles coated with boron nitride. The melts were degassed with high purity argon gas by means of a rotating impeller degasser for 30 minutes, and they were poured at approximately 800°C in a water-cooled copper mold. This mold produces ASTM standard sub-size tensile test specimens that solidify with a uniform cooling rate of about 120°C/s into a supersaturated solid solution. The as-cast specimens were isothermally aged in an electric furnace at 400°C and 450°C for various times ranging from 1 to 150 hours, and then cooled from the aging temperature to room temperature in air.

Table I. Chemical compositions of the alloys in wt.%.

Alloy	Zr	V	Al
A1	0.4	0	Balance
A2	0.8	0.4	Balance
A3	0.4	0.4	Balance
A4	0.1	0.4	Balance

2.2 Microstructure analysis

Samples from the alloys of Table I were prepared for scanning electron microscopy (SEM) by polishing according to standard metallographic

methods and etching with Kelly's reagent. A JOEL-7000F scanning electron microscope operating at 15 kV was used for the analyses. Samples from the alloys of Table I were also prepared for transmission electron microscopy (TEM) by thinning foils cut from the alloys to perforation by means of a twinjet electro-polisher (Fischione Instruments, model 120) operating at 12 volts, and utilizing a solution of 10 vol.% perchloric acid in methanol maintained at -20°C. A JOEL-2010F transmission electron microscope (TEM) was used to measure the size of the precipitate particles. A minimum of 200 particles were analyzed from each sample in order to obtain the mean precipitate size. An aberration corrected MC Zeiss 200-80 TEM operating at 200 kV was used to perform high resolution microstructure analysis.

2.3 Mechanical properties

Tensile properties of the alloys were measured by means of a Universal Testing machine (Instron model 5500R) at an extension rate of 0.05 in/min, and a 1-inch gage length extensometer (MTS model 634.25E-24) was used to measure extension. At least 5 specimens from each alloy were used and the results were averaged and standard deviations were calculated. Fracture of all specimens occurred within the gage length, and specimens with excessive porosity and/or oxides that would affect the results were excluded from the average.

2.4 Atom Probe Tomography

Atom Probe Tomography (APT) specimens of alloy A2 were prepared by the standard lift-out technique in a dual-beam focused ion beam / scanning electron microscopy workstation (FIB/SEM) (Helios NanoLab 600™, FEI Company, USA). Two lift-outs including several samples were extracted from the middle of two Al dendrites. After thinning of the samples, a low energy milling at 2 kV was performed in order to minimize Ga induced damage. APT was performed in a LEAP™ 3000X HR (CAMECA) in voltage mode at 20 % pulse fraction and a repetition rate of 200 kHz. Specimen temperature of about 60 K, pressure lower than 1×10^{-10} Torr (1.33×10^{-8} Pa) and evaporation rate of 5 atoms per 1000 pulses were used for all measurements. Datasets were reconstructed and analyzed with the IVAS™ 3.6.6 software (CAMECA). Overall compositions were measured after background noise subtraction, and all measurements were averaged by weighting the averages based on the total number of atoms of each measurement. The randomness of the atomic distribution in the APT specimens was evaluated by a frequency distribution analysis where the actual distribution of atoms is compared to a completely random dataset described by a binomial probability distribution. The departure from randomness was quantified by a chi-square analysis which allows a significance test. A significance value $p < 0.01$ was chosen to reject the null hypothesis and indicate that there is

significant deviation from randomness in the arrangements of atoms through the dataset. Localized chemical profile of the precipitates was carried out using Zr iso-concentration surfaces and proximity histograms.

3. RESULTS

3.1 As-cast microstructure

Fig. 1 shows a typical SEM photomicrograph taken from an as-cast A3 alloy sample. The sample was etched so its dendrite structure is revealed. Careful examination of this and many similar photomicrographs taken from the alloys in Table I show no primary phase precipitates, which suggests that the fast cooling rate used in making these samples suppressed precipitation and allowed formation of a supersaturated α-Al solid solution, even though the zirconium and/or vanadium content of the alloys may exceed their solubility limit in aluminum.

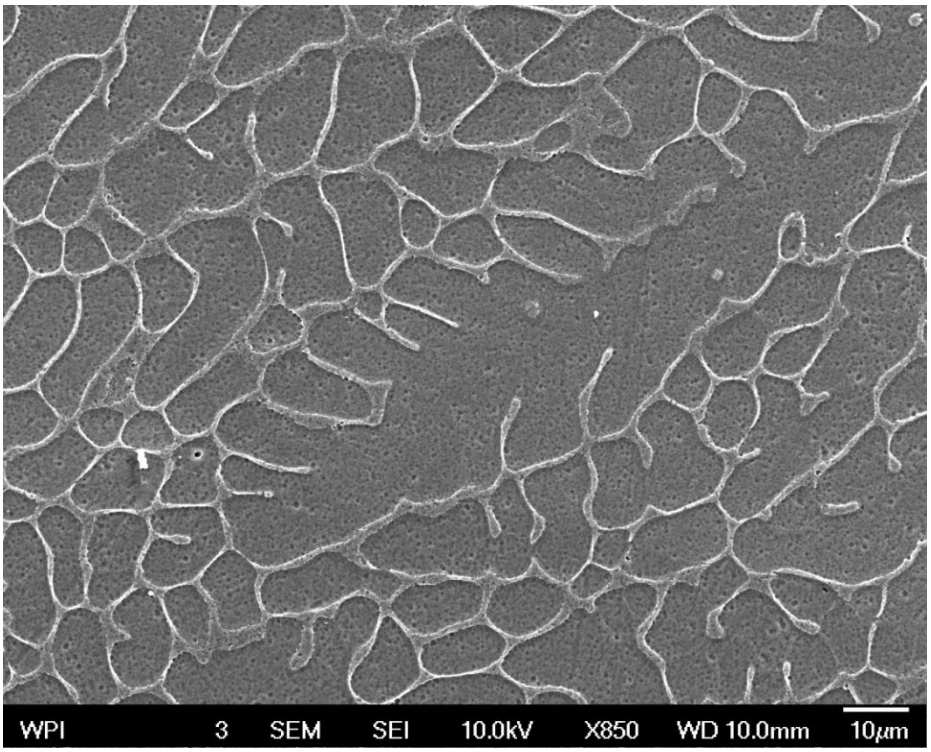

Fig. 1 SEM photomicrograph of as-cast alloy A3 of Table I.

3.2 Room-temperature mechanical properties

Fig. 2 shows the variation in measured yield strength of alloys A2, A3, and A4 with aging time at 400°C and 450°C. It is clear that at both aging temperatures the yield strength of the three alloys peaks after about 32 hours and alloy A2 has the highest yield strength. Holding the alloys at these temperatures for longer times does not significantly change their yield strength.

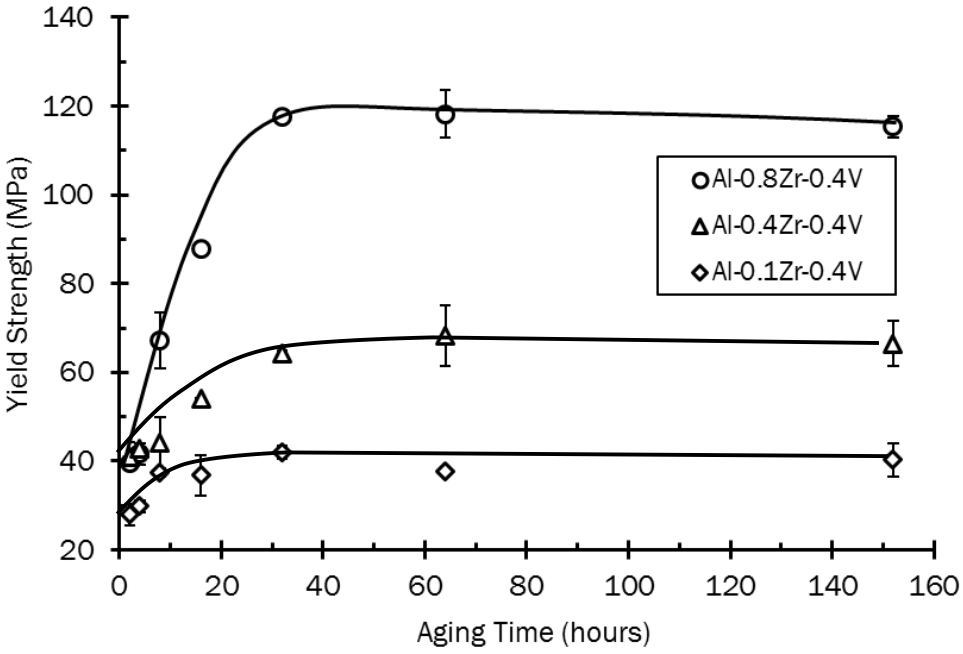

(a)

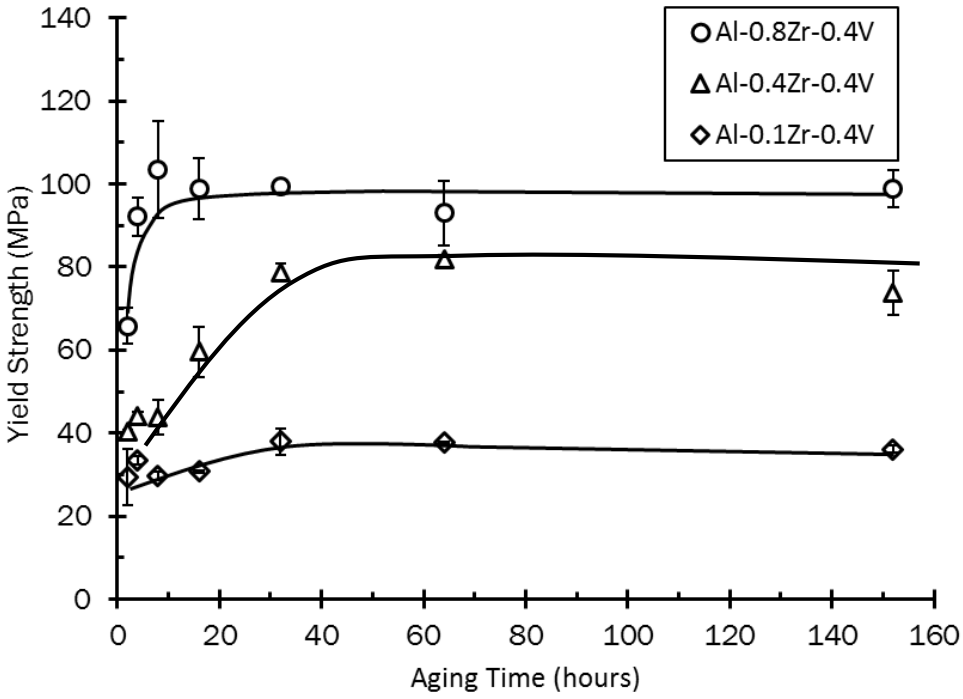

(b)

Fig. 2 Yield strength *vs.* aging time curves for Al-Zr-V alloys. (a) aged at 400°C, and (b) aged at 450°C.

3.3 Aged microstructure

Fig. 3 shows typical HRTEM images of samples from alloys A2, A3, and A4 that were aged at 400°C for 32 hours. The strain and Z contrast of the $Al_3(Zr_{1-x}V_x)$ precipitate particles can be clearly distinguished in these images. The precipitate particles in all three alloys are 4-6 nm in diameter. Alloy A2 has the highest volume fraction of $L1_2$-$Al_3(Zr_{1-x}V_x)$ particles and alloy A4 has the lowest, which is consistent with the measured yield strength of these alloys (see Fig. 2). The strain and Z contrast of the precipitate particles can be clearly distinguished in these images. The precipitate particles in all three alloys are 4-6 nm in diameter, and the particles are fully coherent with the aluminum matrix. As Fig. 3(d) shows, the samples were tilted to the [100] zone axis and the superalattice diffraction pattern contributed by $L1_2$ phase can be clearly seen. Therefore it is reasonable to conclude that these particles are $Al_3(Zr,V)$ precipitates with $L1_2$ crystal structure.

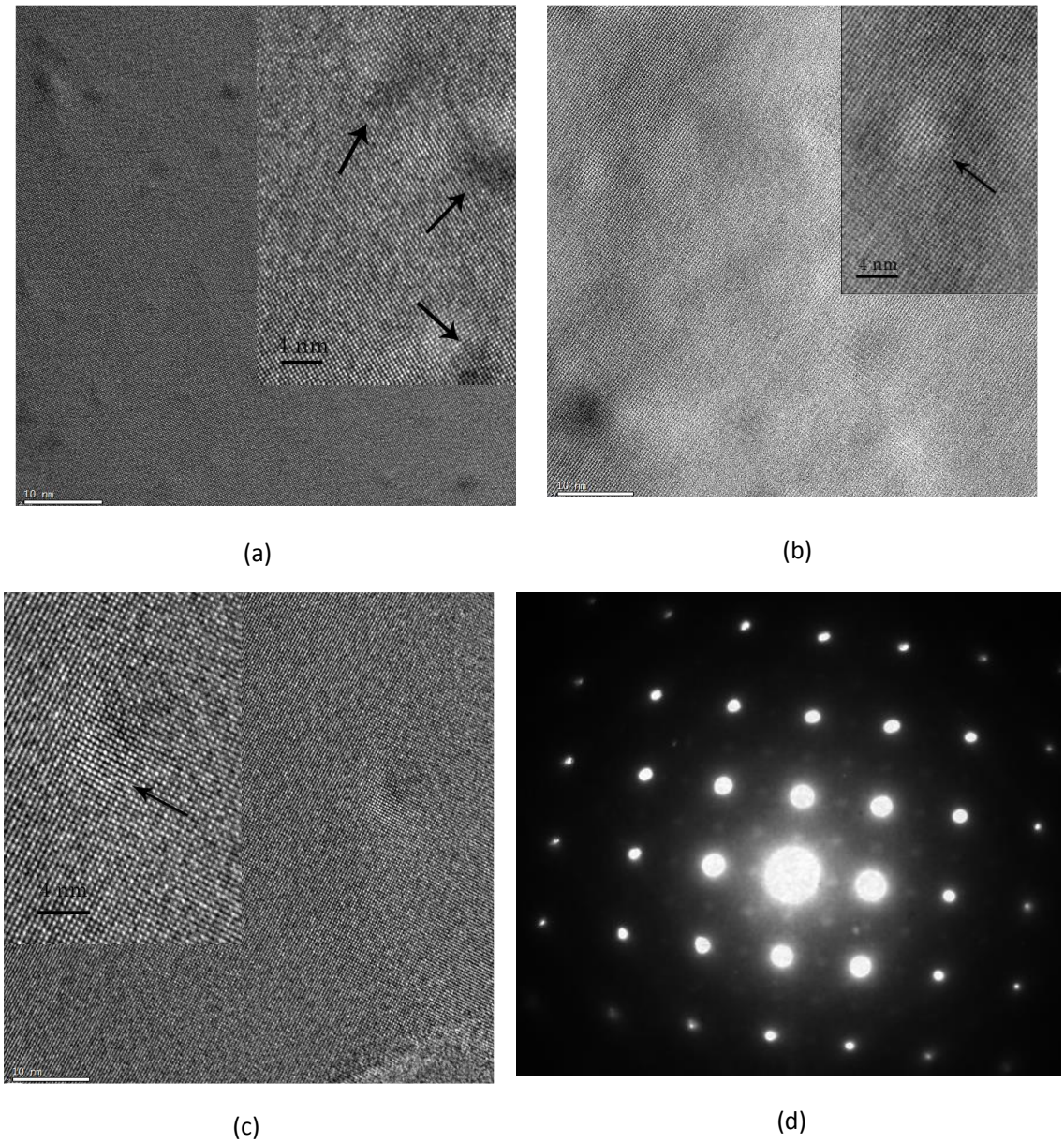

Fig.3 HRTEM micrograph of $Al_3(Zr_{1-x},V_x)$ precipitates in alloys (a) A2, (b) A3, and (c) A4. (d) Select Area Electron Diffraction (SAED) pattern of A3 alloy.

3.4 Atom probe tomography

Fig. 4 shows Zr and V atomic maps obtained by APT performed on a typical specimen of A2 alloy. The ATP samples are classified into two groups: (1) showing precipitates, and (2) without precipitates. Since APT measurements involve extremely small volumes, it is not unexpected to

find these two types of regions inside dendrites. Within 10 APT samples analyzed, 5 of them show no precipitates with a completely random distribution of Zr and V. The other 5 samples show clear precipitation of Zr in all samplings while V showed non-random atomic distribution in 3 of them. The element concentrations together with calculated standard deviations are presented in Table II. Several observations may be made: (1) because there is no significant particle clustering in Group 2 samples, the *overall* composition in each one of the Group 2 samples was measured. On the other hand, because of element clustering in Group 1 samples, the composition of each one of the Group 1 samples was measured twice - once including the clusters and once excluding the clusters. There is no difference in the V content of the Group 1 samples whether the clusters are included or excluded from the measurements, which indicates that the average concentration of V inside the precipitate particles is approximately equal to that in the aluminum matrix; (2) the average amount of V in the matrix of Group 1 samples is around 5 times higher than that in Group 2 samples; (3) the amount of Zr in the matrix of both Group 1 and Group 2 samples is approximately the same (around 0.11 ± 0.04 at.% Zr)

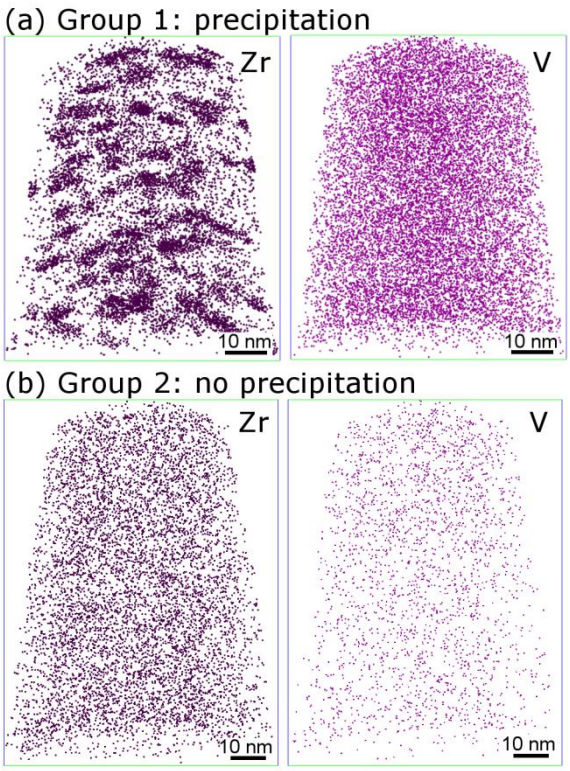

Fig. 4 Atom Probe Tomography (APT) Zr and V atomic maps. (a) Group 1: showing precipitation, (b) Group 2: showing no precipitation.

Table II: Zr and V bulk concentrations obtained by Atom Probe Tomography.

		Zr (at.%)	**V (at.%)**
Group 1	Matrix + precipitates	0.21 ± 0.03	0.26 ± 0.10
	Matrix - precipitates	0.11 ± 0.04	0.26 ± 0.10
Group 2		0.09 ± 0.01	0.05 ± 0.03

Fig. 5 shows a proximity histogram constructed on a iso-concentration surface with 2.5 at.% Zr. The profile shows the average of 70 precipitates in one sample. The Zr content of the precipitates is around 25 at.% Zr in good agreement with the expected Al_3Zr phase which suggests that the formation of the $Al_3(Zr,V)$ phase is due to a nucleation and growth mechanism and not by spinodal decomposition because the transition state of the $Al_3(Zr,V)$ clusters is not observed [26]. The concentration of V inside the precipitate particles is around 0.6 at.% suggesting a particle stoichiometry of approximately $Al_3(Zr_{24.4},V_{0.6})$. Careful examination of Fig. 5 also shows that the concentration of V at the precipitate/matrix

interface is significantly high (about 1 at. %). This is about 4 times higher than the average concentration of V inside the precipitate particles and in the matrix.

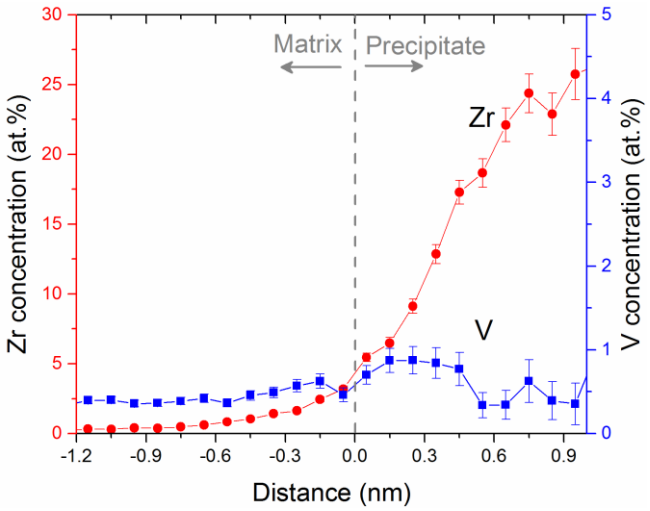

Fig. 5 APT Proximity Histogram constructed on an iso-concentration surface at 2.5 at.% Zr.

3.5 Microstructure of alloys soaked at 350°C

Figs. 6, 7, 8, and 9 are typical TEM photomicrographs of samples from alloys A1, A2, A3, and A4 that were aged at 400°C for 32 hours, and then soaked at 350°C for 100 hours, 300 hours, and 500 hours. The Figs. show that the precipitate particles in alloys A1, A2, and A3 remain spherical in shape and their average diameter does not change significantly with soaking time up to 500 hours. On the other hand, the precipitate particles in alloy A4 become elliptical in shape and increase in size after 300 hours at 350°C. Fig. 10 shows a SADP taken from the precipitate phase in alloy A4. In producing this pattern, the sample was tilted to the [323] Al zone axis. The dim diffraction spots are from $Al_3(Zr_{1-x}V_x)$ precipitates with zone

axis $[11\bar{1}]$. The lattice parameters of this precipitate are found to be a = 0.37 nm and c = 0.80 nm. The equilibrium crystal structure of the Al_3Zr phase is $D0_{23}$ with lattice parameters a = 0.4013 nm and c = 1.732 nm [27]. The equilibrium crystal structure of the Al_3V phase is $D0_{22}$ with lattice parameters a = 0.378 nm and b = 0.8321 nm [28]. It is difficult to ascertain from the diffraction pattern whether the $Al_3(Zr_{1-x}V_x)$ precipitate has the $D0_{22}$ or the $D0_{23}$ crystal structure; however its lattice parameters are very close to the lattice parameters of the Al_3V phase, which suggests that the $Al_3(Zr_{1-x}V_x)$ precipitate has the $D0_{22}$ crystal structure. It is therefore submitted that the long soak time at 350°C causes the metastable $L1_2$- $Al_3(Zr_{1-x}V_x)$ precipitates in alloy A4 to transform from the metastable $L1_2$ crystal structure to the $D0_{22}$ crystal structure. This is plausible in light of the fact that the $Al_3(Zr_{1-x}V_x)$ precipitate in alloy A4 contains more than 87% vanadium. The orientation relation between the aluminum matrix and the $D0_{22}$- $Al_3(Zr_{1-x}V_x)$ precipitate was found to be:

$$Al\ [323]\ //\ D0_{22}\text{-}Al_3(Zr_{1-x}V_x)[11\bar{1}]$$

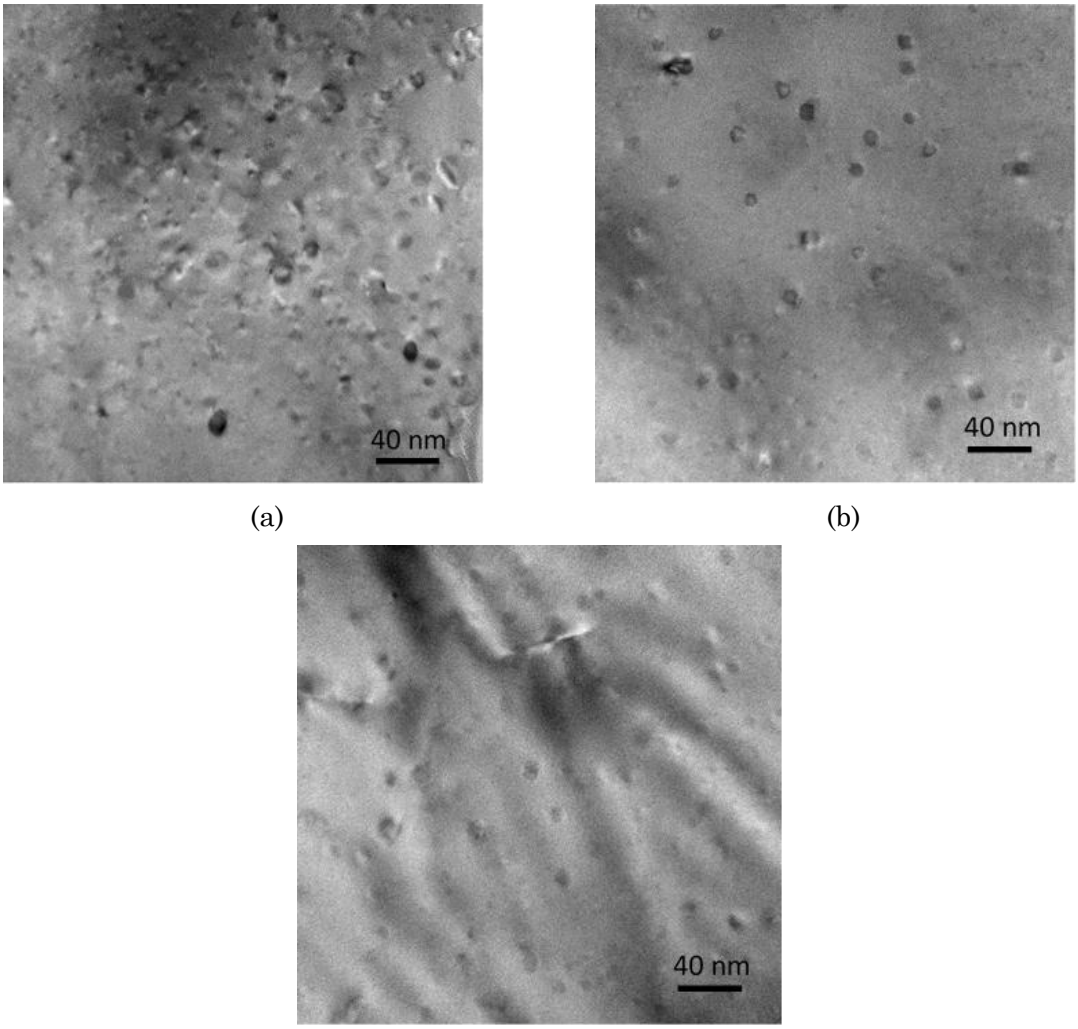

(a) (b)

(c)

Fig. 6 TEM photomicrograph of alloy A1 that was aged at 400°C for 32 hours and then soaked at 350°C for (a) 100 hours, (b) 300 hours, and (c) 500 hours.

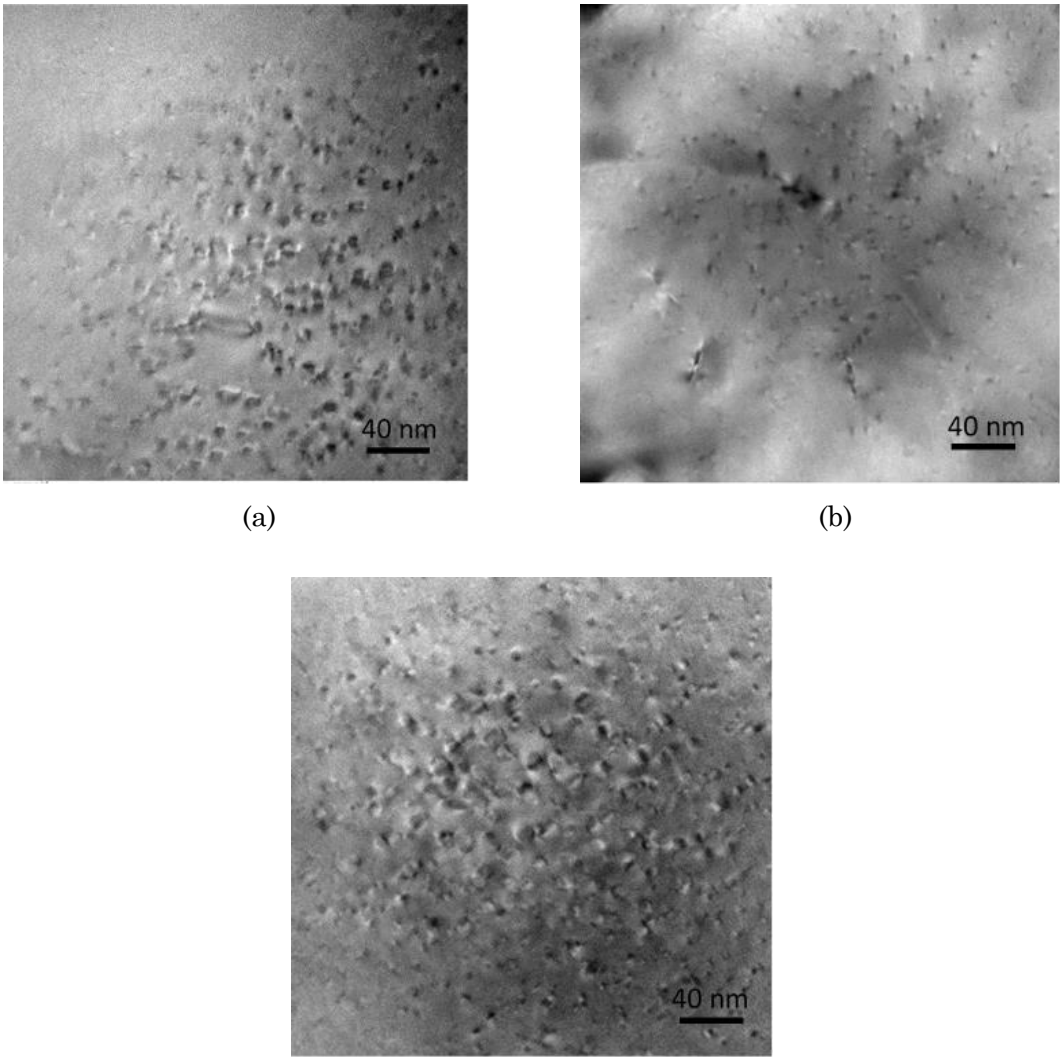

(a) (b)

(c)

Fig. 7 TEM photomicrograph of alloy A2 that was aged at 400°C for 32 hours and then soaked at 300°C for (a) 100 hours, (b) 300 hours, and (c) 500 hours.

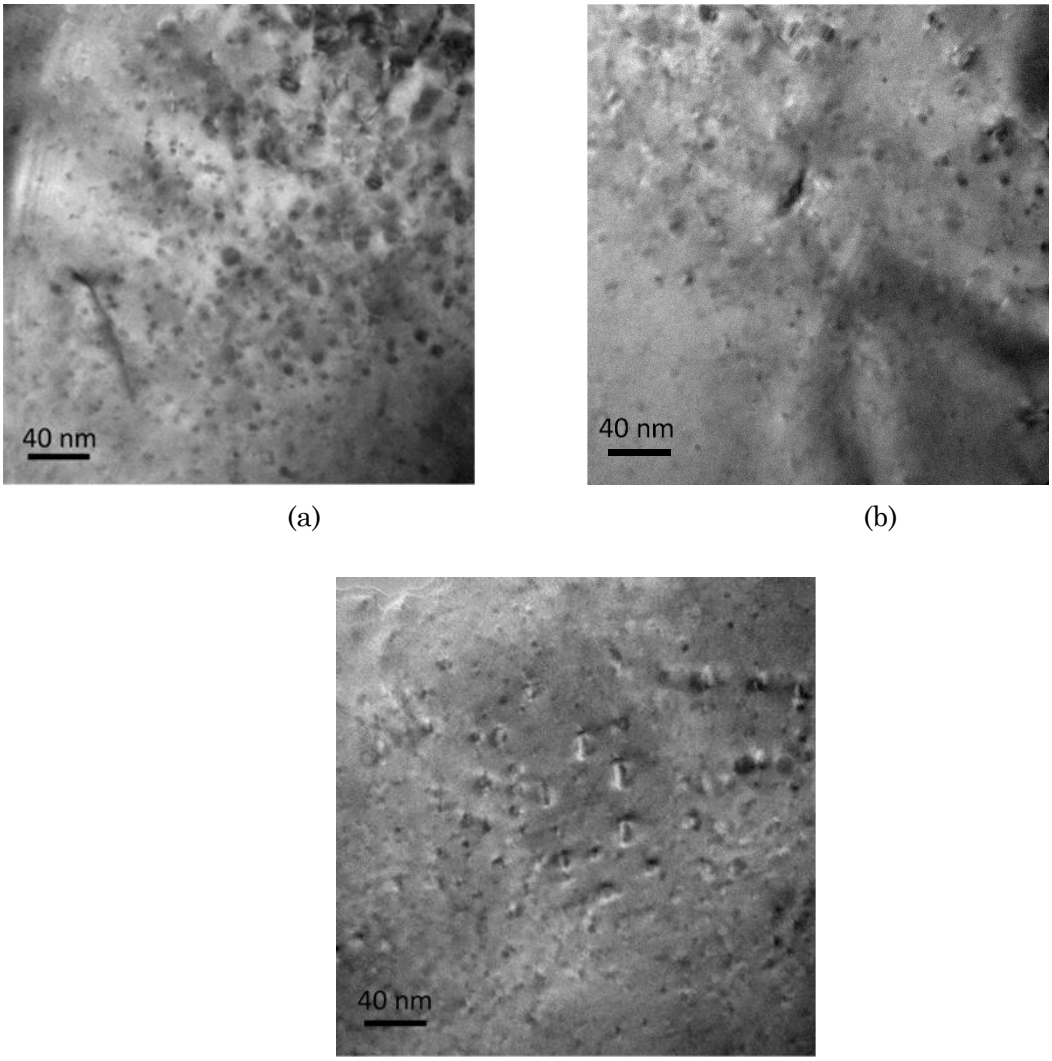

(a) (b)

(c)

Fig. 8 TEM photomicrograph of alloy A3 that was aged at 400°C for 32 hours and then soaked at 350°C for (a) 100 hours, (b) 300 hours, and (c) 500 hours.

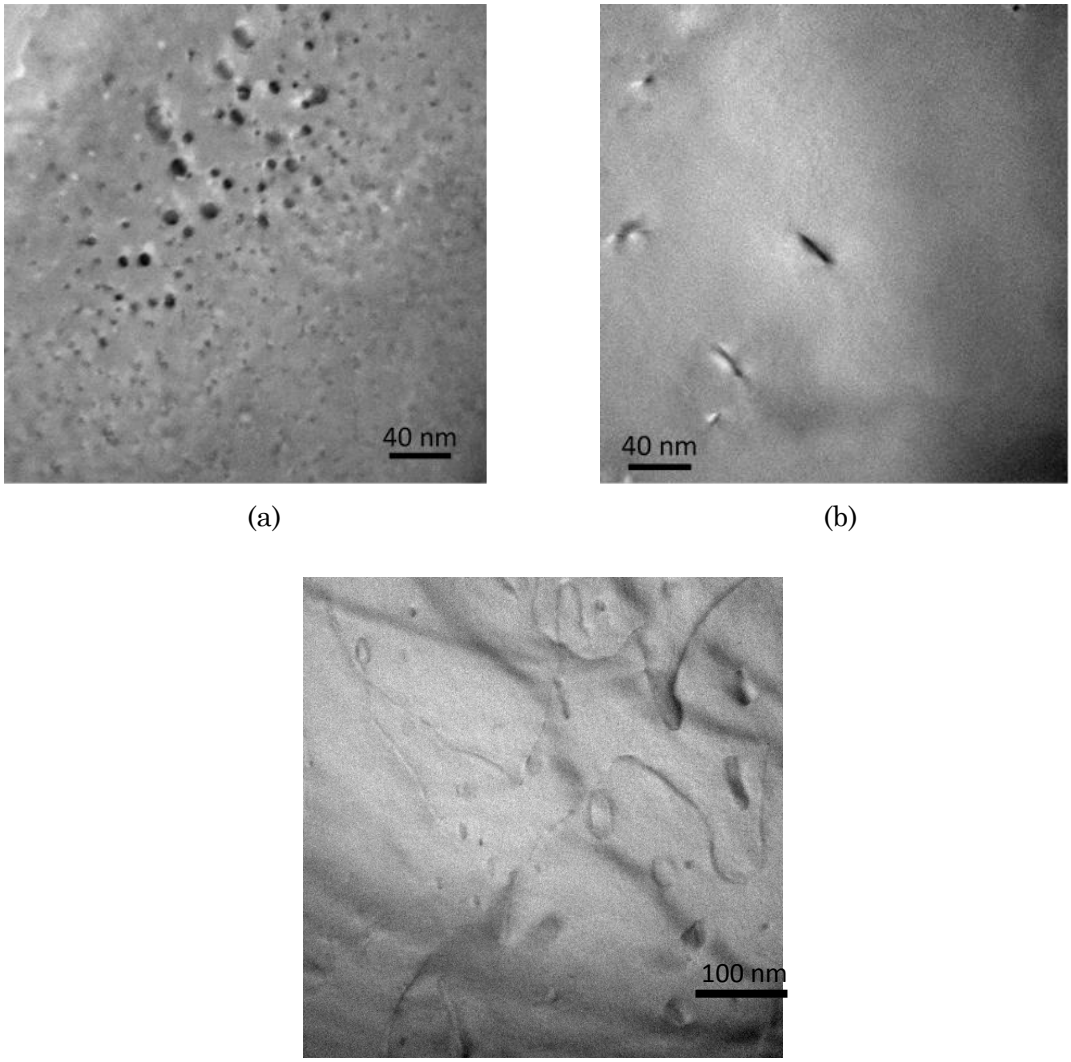

(a) (b)

(c)

Fig. 9 TEM photomicrograph of alloy A4 that was aged at 400°C for 32 hours and then soaked at 350°C for (a) 100 hours, (b) 300 hours, and (c) 500 hours.

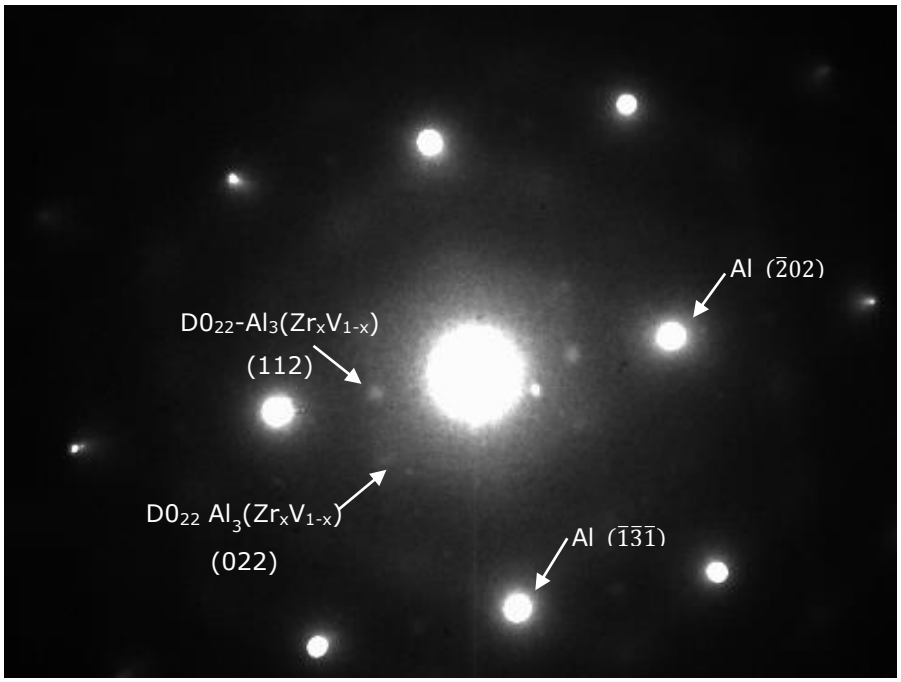

Fig. 10 Select area diffraction pattern of stable $Al_3(Zr_{1-x}V_x)$ precipitates in alloy A4. The sample was tilted to the [323] Al zone axis, and the zone axis of the precipitate is $[11\bar{1}]_p$. Note that $(\bar{1}\bar{1}0)_p$ and $(110)p$ diffraction spots overlapp with the incident beam, therefore they are not visible in this pattern.

Fig. 11 shows the change in the average size of the precipitate particles in alloys A1, A2, A3, and A4 as functions of time at 350°C. For spherical particles, the mean radius, <*R*>, was used as a measure of size, and for elliptical particles, the mean half-length axis <L_a/2>, was used as a measure of size. The coarsening kinetics of the $L1_2$ phase isothermally aged at 350°C are shown in Fig. 11. As predicted by the Lifshitz, Slyozov, and Waagner (LSW) theory, the cube of the average particle radius is linearly dependent on the isothermal soak time:

$$\langle R(t)\rangle^3 - \langle R(t_0)\rangle^3 = k(t - t_o) \qquad (1)$$

In Eq. (1), $\langle R(t)\rangle$ is the average particle radius at time t, $\langle R(t_0)\rangle$ is the

value of $\langle R \rangle$ at t_o, and k is the kinetic coarsening rate constant. The kinetic coarsening rate constant – k in Eq. (1) – was calculated by means of a least squares analysis and is reported in Table III.

As Table III shown, with the limited amounts of V added into Al-Zr alloys, the coarsening rate of $Al_3(Zr,V)$ precipitates is significantly decreased. When V and Zr atomic ratio reaches to about 1.79, the coarsening rate of $Al_3(Zr_{1-x}V_x)$ is about 10 times slower than Al_3Zr phase at 350°C. This result is consistent with other studies. For example, Fine [25] determined the coarsening rate of Al_3Zr precipitates in an Al-Zr alloy to be 6.9×10^{-3} nm^3/s at 425°C, and Chen [23] determined the coarsening rate of $Al_3(Zr_{1-x}V_x)$ precipitates with a V:Zr ratio of 2.7 to be 2.86×10^{-5} nm^3/s at 425°C. However, higher amounts of V does harm to the thermal stability of the precipitate particles. For example, when the V:Zr atomic ratio is 7.14, the coarsening rate of the $Al_3(Zr_{1-x}V_x)$ particles is almost twice as large as that of the Al_3Zr particles at 350°C, and the particles readily transform to the equilibrium $D0_{22}$ crystal structure.

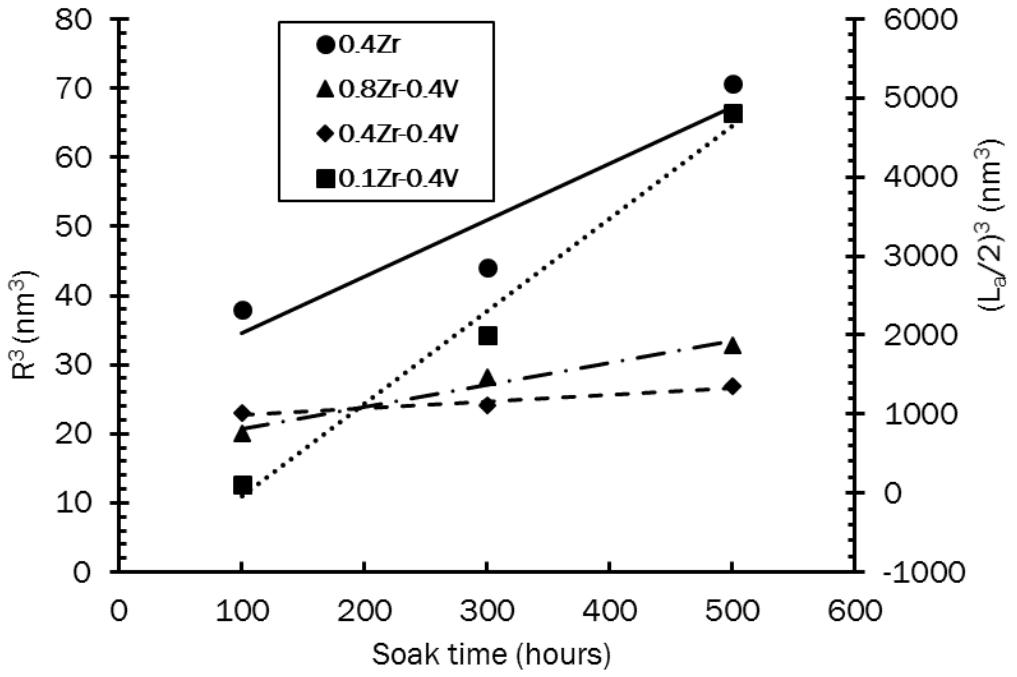

Fig. 11 The cube of the mean size parameters of precipitates in the alloys of Table I. The *y*-axis for alloy A4 is $(L_a/2)^3$.

Table III Measured kinetic coarsening rate constants and lattice parameter mismatches for the $L1_2$ particles isothermally aged at 350°C.

Alloy	V:Zr atomic ratio	Kinetic coarsening rate constant (nm^3/s)
A1	0	2.275×10^{-5}
A2	0.67	8.806×10^{-6}
A3	1.79	2.639×10^{-6}
A4	7.14	3.261×10^{-3}

4. DISCUSSION

4.1 Decomposition of $Al_3(Zr,V)$ precipitates in Al-Zr-V alloys

Compositional fluctuations in the as-cast Al-Zr-V samples is inevitable and APT analyses shows that the concentration of V in particular significantly varies from location to location so that the highest V concentration may be five times larger than the lowest. Classical

nucleation theory [29] suggests that the nucleation rate I may be given by

$$I \propto \exp[-\frac{\Delta G^*}{k_B T}] \quad (2)$$

where ΔG^* is the energy required to form a precipitate particle with the critical size; and k_B is Boltzmann constant. For spherical particles, ΔG^* is

$$\Delta G^* = \frac{16}{3}\frac{\pi\gamma^3}{\Delta g^2} \quad (3)$$

In which γ is the interfacial energy between the precipitate and the matrix; Δg is the energy of formation of the precipitate, which is negative. Eqs. (2) and (3) show that the lower the energy of formation of the precipitates, the higher the nucleation rate. Based on the fact that the precipitate particles tend to cluster in the region of the sample that is enriched with V, it can be assumed that V accelerates the nucleation rate of the $Al_3(Zr_{1-x}V_x)$ phase. This implies that the $Al_3(Zr_{1-x}V_x)$ phase has a lower energy of formation than the Al_3Zr phase. This is in line with the APT findings, which show that the precipitates tend to cluster in the regions with relatively high V concentration.

Fig. 5 shows the concentration profile of Zr and V across the matrix/precipitate interface. It is clear that while the Zr concentration increases sharply at the interface, the V concentration does not. This suggests that during the early stages of nucleation and growth of the precipitate particles, Zr diffuses relatively fast and clusters in those

regions that are enriched in V. Vanadium, on the other hand, diffuses much slower because its diffusion coefficient is much smaller than that of Zr (at 400°C, $D_{Zr} = 1.2\times10^{-20}$ m²/s and $D_V = 4.85\times10^{-24}$ m²/s [30, 31]); hence it takes V more time to diffuse into the precipitate. It is interesting to note that the concentration profile of Zr is an uphill diffusion profile while that of V is a typical down hill Zener [32] diffusion profile. Careful examination of Fig. 5 also reveals a decrease in the V concentration right at the precipitates/matrix interface. This V depletion is cause by diffusion of V into the precipitate particle. Based on these observations, it is submitted that growth of the $Al_3(Zr_{1-x}V_x)$ precipitate occurs in two stages. First, the Al_3Zr phase nucleates and grows by uphill diffusion of Zr atoms into regions that are enriched with V relative to the rest of the matrix. Then, V atoms slowly diffuse into the Al_3Zr particles by the typical Zener precipitate growth mechanism so as to gradually convert the Al_3Zr particles into V enriched $Al_3(Zr_xV_{1-x})$ particles. A similar mechanism has been recently reported for the formation of $Al_3(Zr_xSc_{1-x})$ precipitates in Al-Zr-Sc alloys [7, 14-16]. But in the Al-Zr-Sc system, the diffusion coefficient of Sc atoms in aluminum is much larger than that of Zr atoms, therefore the Sc atoms tend to cluster together and form an Al_3Sc core into which Zr atoms gradually diffuse to form the $Al_3(Zr_xSc_{1-x})$ precipitate.

4.2 Energy of formation of the $L1_2$-Al_3Zr and $Al_3(Zr_{1-x}V_x)$ precipitates

The coarsening rate of precipitates is related to the Gibbs energy of their formation in such a way that the lower the energy of formation of a precipitate, the lower is its coarsening rate [33], and hence the more thermally stable is the precipitates.

The energy of formation of the $Al_3(Zr_{1-x}V_x)$ phase may be given by Eq. (4)

$$\Delta G_{Al_3(Zr_{(1-x)}V_x)} = x\Delta G_{Al_3V} + (1-x)\Delta G_{Al_3Zr} + G_m^{ex} + RT[xlnx + (1-x)ln(1-x)] \quad (4)$$

in which $x = \frac{n_V}{n_V + n_{Zr}}$

The energy of formation of the $L1_2$-Al_3Zr phase was measured to be [27]:

$$\Delta G_{Al_3Zr} = -40300 + 11.59T \quad (5)$$

The energy of formation of the $L1_2$-Al_3V phase is unavailable in the open literature. However, because the $Al_3(Zr_{1-x}V_x)$ phase easily transforms to the $D0_{22}$ crystal structure at 350°C when V:Zr > 7, we will use the energy of formation of the $D0_{22}$-Al_3V phase in place of that of the $L1_2$-Al_3V [28]

$$\Delta G_{Al_3V-D0_{22}} = -26600 + 8.50273T \quad (6)$$

Fig. 12 is a schematic representation of the change in the energy of

formation of the $Al_3(Zr_{1-x}V_x)$ phase as function of its V content. An increase in the V content of the $Al_3(Zr_{1-x}V_x)$ precipitate leads to a decrease in its energy of formation, and hence its coarsening rate. This trend continues until an optimum V content is reached, beyond this point, further increases in the V content of the precipitate leads to an increase in its energy of formation until eventually the energy of formation of the $Al_3(Zr_{1-x}V_x)$ phase becomes larger than that of the Al_3Zr precipitate. Fig. 12 explains why even small additions of V to the Al_3Zr precipitate lowers its coarsening rate and enhances its thermal stability: As the $Al_3(Zr_{1-x}V_x)$ phase is subjected to elevated temperature, V continuously diffuses into it, and as long as its concentration in the precipitate is below the optimum amount, the precipitate will have a slower coarsening rate than that of the Al_3Zr phase; however, once the V concentration in the precipitate exceeds the optimum value, the precipitate will be prone to coarsening.

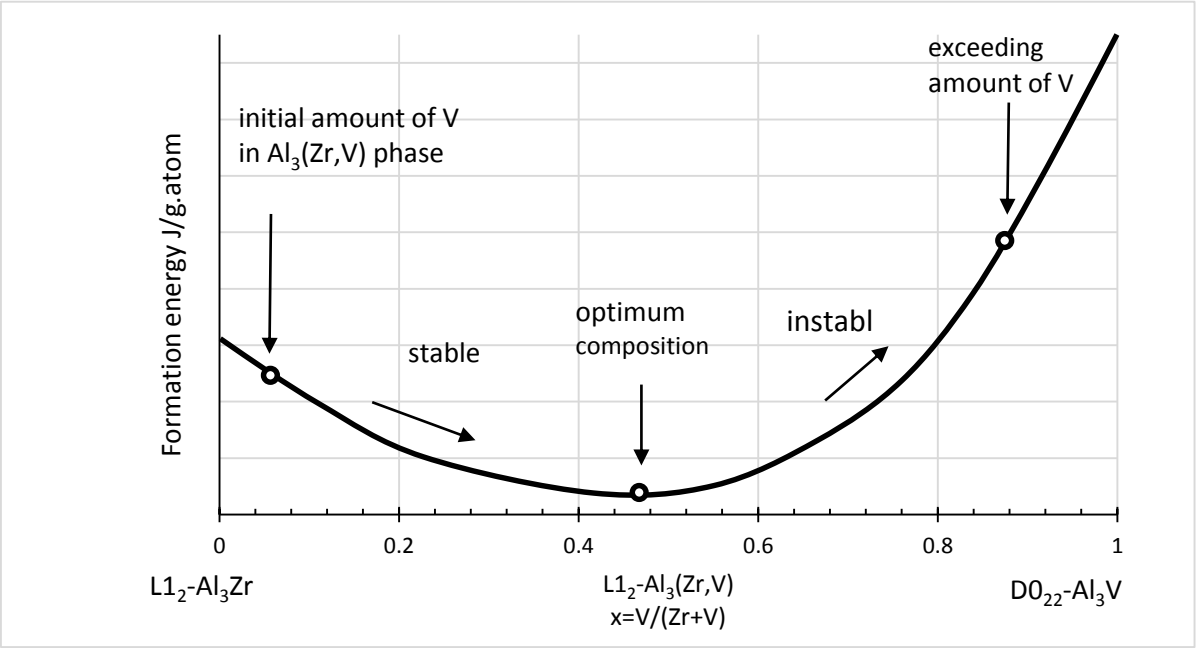

Fig.12 Sketch of the energy of formation of the $Al_3(Zr_{1-x}V_x)$ phase as function of the V concentration.

4.3 Precipitation strengthening mechanisms

Fig. 2 reflects the strengthening process occurring during aging of the alloys in Table I. The measured average yield strength of alloys A2, A3, and A4 in the as-cast condition are respectively 25 MPa, 38 MPa, and 40 MPa, which are quite low, but yet somewhat higher than the yield strength of pure aluminum. This is expected due to the presence of zirconium and vanadium in solid solution. After aging, precipitates form in these alloys, and when the aged alloy is subjected to stress, dislocations move in the alloy matrix and as they do so they encounter the precipitate particles on their slip plane. If the work required to shear the precipitate particles is high, the dislocations will not be able to *cut* the particles and they can only bypass the particles by looping around them. This

mechanism was first suggested by Orowan in 1948 and is known as the Orowan mechanism. The increase in yield strength due to Orowan dislocation looping is given by [34]

$$\Delta\sigma_{Orowan} = \frac{M0.4Gb}{\pi L}\frac{\ln\left(\frac{\pi\langle R\rangle}{2b}\right)}{\sqrt{1-\upsilon}} \tag{7}$$

Where L is the effective spacing between precipitate particles and is given by [35]:

$$\mathrm{L} = \left(\sqrt{\frac{2\pi}{3f}} - \pi/2\right)\langle \mathrm{R}\rangle \tag{8}$$

On the other hand, if the work required to shear the particles is practicable, then the particles will be cut, and a number of strengthening mechanisms may become operative. These include (i) surface strengthening, (ii) coherency strain strengthening, (iii) atomic order strengthening, (iv) stacking fault strengthening, and (v) modulus strengthening. Since precipitation of $L1_2$-$Al_3(Zr_{1-x}V_x)$ particles in an aluminum matrix is an order/disorder phase transformation; then the atomic order strengthening mechanism will dominate [35], and the additional strengthening is approximately given by [35]:

$$\Delta\sigma_{order} = M\frac{\gamma_{APB}}{2b}\left[\left(\frac{3\pi^2\gamma_{APB}f < R >}{32\Gamma}\right)^{\frac{1}{2}} - f\right] \tag{9}$$

In Eq. (9) M is the Taylor factor, it relates the macroscopic yield strength to the critical resolved shear stress so that$\sigma_y = M\Delta\tau_{CRSS}$. For texture-free

fcc metals, M = 3.06 [36]. γ_{APB} is the anti-phase boundary energy between the precipitate and the aluminum matrix, b is Burger's vector, for aluminum b = 0.286 nm [37], f is volume fraction of the precipitate, <R> is the mean radius of the precipitates, and Γ is the line tension in the dislocation, and is given by [35]:

$$\Gamma = \frac{Gb^2}{4\pi}\left[\frac{1+\nu-3\nu sin^2\xi}{1-\nu}\right]\ln\left(\frac{\Lambda}{r_0}\right) \tag{10}$$

In Eq. (10), G is the shear modulus at room temperature – for aluminum G = 26.2 GPa [37], ν is the matrix Possion's ratio – for aluminum ν = 0.362 [38]. ξ is the angle between the dislocation line and the precipitate particle. It is usually assumed that edge dislocations dominate movement on the slip plane so that $\xi = \pi/2$ [35]. r_0 is the inner-cut dislocation radius and is approximately equal to $2b$ [35]. Λ is the outer-cut dislocation radius and is given by [39]:

$$\Lambda = \frac{4\langle R\rangle}{3f} - 2\langle R\rangle \tag{11}$$

When the Orowan mechanism is operative, the increment to yield strength is proportional to $f^{\frac{1}{2}}\langle R\rangle$. In principle, this function rises with decreasing particle size until the theoretical critical resolved shear stress (CRSS) of the alloy is reached. The strengthening increment from the more complex particle shearing mechanism follows an equation of the form $\beta f^n\sqrt{\langle R\rangle}$; where β and n depend on the controlling particle shearing mechanism. Eq. (7) and Eq. (9) are used to plot the theoretical increase

in strength as a function of precipitate size. The theoretical strengthening increment is the minimum of the values given by Orowan mechanism and the order strengthening mechanism, as shown in Eq. (12).

$$\Delta\sigma = \min(\Delta\sigma_{Orowan}, \Delta\sigma_{order}) \tag{12}$$

When $\Delta\sigma_{Orowan} = \Delta\sigma_{order}$, the strengthening increment reaches its possible maximum, which corresponds to a critical radius that may be determined by equating Eq. (7) to Eq. (9) or approximately from Eq. (13) [].

$$R_c = \sqrt{\frac{3}{2}}\left(\frac{Gb^2}{2\gamma_{APB}}\right)\left(1 + 1.53\sqrt{\frac{f}{\pi}}\right) \tag{13}$$

4.4 Estimation of the antiphase boundary energy

APB energies of intermetallic compounds are difficult to determine, and different methods for calculating them tend to give different values [40, 41]. For this reason, they are not available for many compounds, and certainly not for the $L1_2$- $Al_3(Zr_{1-x}V_x)$ intermetallic. In what follows an indirect method is described and used to estimate the magnitude of γ_{APB} for the $L1_2$- $Al_3(Zr_{1-x}V_x)$ phase. The method requires accurate measurement of a series of mean precipitate particle radii and the increment of yield strength (or hardness) that each particle radius

imparts to the alloy. Next, Eq. (12), which gives the theoretical yield strength increment *vs.* precipitate radius is used to produce a *theoretical* curve. All parameters; in Eq. (12), i.e. G, b, v, etc., are known except for γ_{APB}. A magnitude for γ_{APB} is guessed and then iteratively adjusted until a best fit is found between the theoretical curve and the measured values of precipitate radii *vs*. strengthening increment. Figs. 13, 14, and 15 show this procedure applied to alloys A1, A2, and A3. In order to get the data points in Figs. 13, 14 and 15, the samples were aged at 400°C for 32 hours first, and then they were soaked at 350°C for 100, 300, and 500 hours. Both the yield strength and the mean precipitate radius were measured in each sample. From these Figs., and using the procedure just described, γ_{APB} is determined to be between 0.18 J/m^2 and 0.19 J/m^2. As Figs.13-15 shown, the strengthening mechanism in alloys A1, A2, and A3 is order strengthening. This is because the average size of the precipitates in these alloys (measured to be 3 – 4.5 nm in radius) is smaller than the critical radius. It is worth noting that the strength increment caused by the order strengthening mechanism is very sensitive to the magnitude of γ_{APB} to the extent that changing γ_{APB} by as little as 0.01 J/m^2 significantly shifts the experimental data points. Therefore, the accuracy of calculating γ_{APB} by this method is in the range of 0.01 J/m^2. Note that this method was not applied to alloy A4. This is because the precipitate in alloy A4 transforms from the $L1_2$ crystal structure to the $D0_{22}$ crystal

structure upon soaking at 350°C for 300 hours. The APB energy of the $D0_{22}$ phase is different from that of the $L1_2$ phase; moreover, the shape of the precipitate changes form spherical to elliptical; and hence Eqs. (7) and (9) become inapplicable. The APB energy determined by this method is lower than the value reported by Lefebvre who used measurements of precipitate critical radius to calculate the APB energy between $L1_2$-Al_3Zr precipitate particles and the aluminum matrix to be 0.445 J/m^2 [42]. However, such a high magnitude for γ_{APB} would signify an unrealistically large strengthening increment. Liu [43] calculated γ_{APB} for the (001) plane in $D0_{22}$-$Al_3(Zr_{0.125}Ti_{0.875})$, which should be close to the APB energy for the (001) plane in $L1_2$-$Al_3(Zr_{1-x,}\ V_x)$ because there is only a small difference (0.1 eV per unit formula) between the APB energy for the (001) plane in the $D0_{22}$ and L_{12} structures of Al_3Ti [43][5]. He reported γ_{APB} = 0.0683 J/m^2.

[5] Although it is generally known that fcc materials fail by slip along the planes, the APB energy for the {001} planes may be used instead of the APB energy for the {111} planes because it [43] has been shown that the main deformation mode in Al_3V is dislocation dissociation of the type <110> on {001} planes.

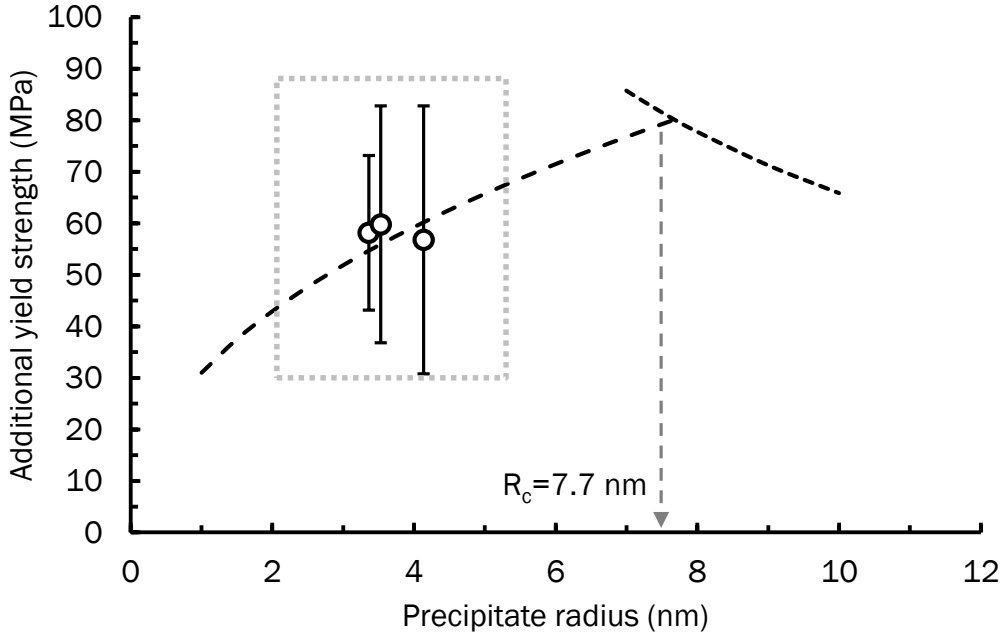

(a)

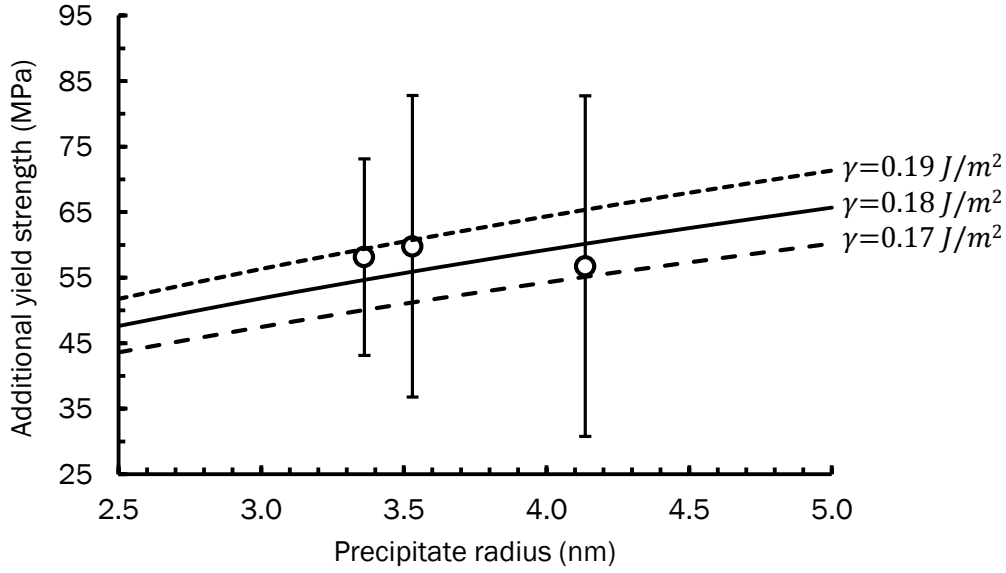

(b)

Fig. 11 Theoretical yield strength increment *vs.* precipitate radius for alloy A1 (a) Orowan strengthening and order strengthening curves calculated from Eqs. (4) and (6). (b) Region within the marked area in (a) enlarged for better visualization and curves plotted with different magnitudes of γ_{APB}.

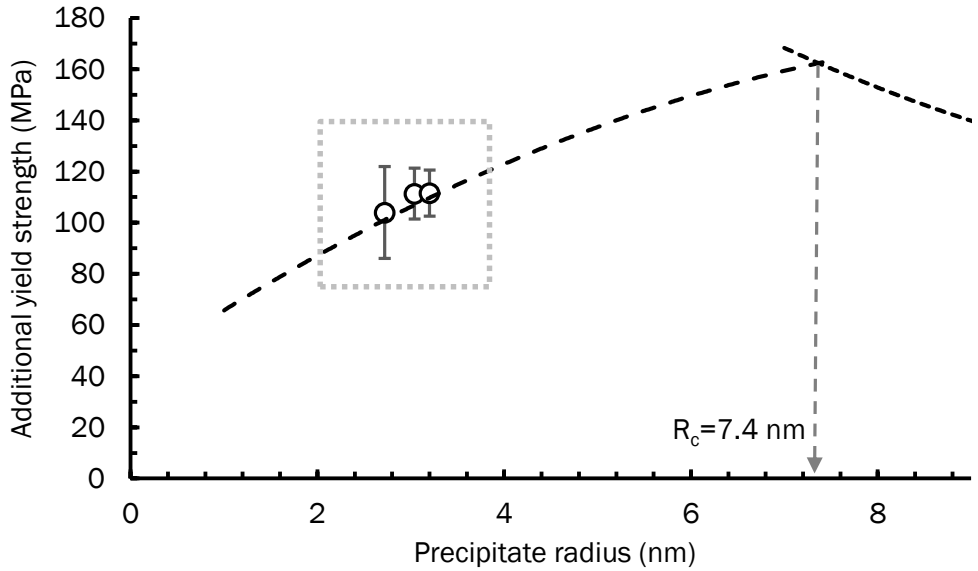

(a)

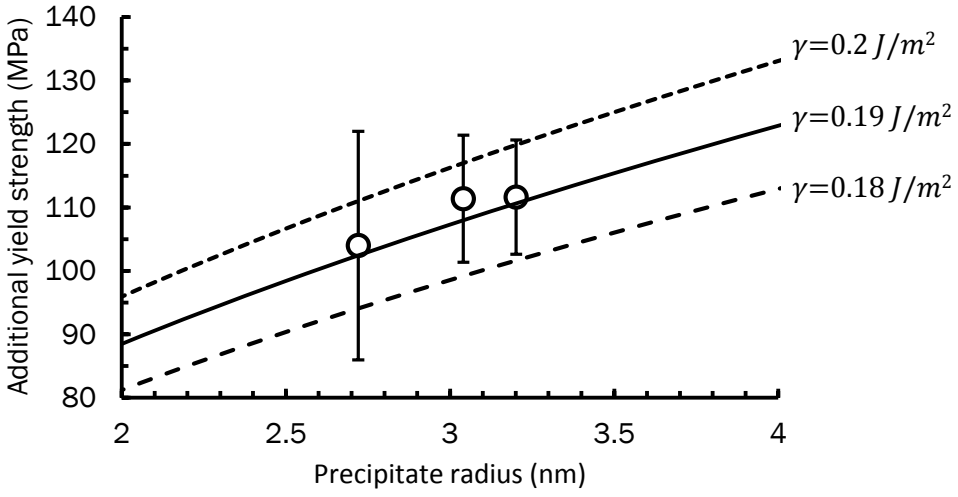

(b)

Fig. 12 Theoretical yield strength increment *vs.* precipitate radius for alloy A2 (a) Orowan strengthening and order strengthening curves calculated from Eqs. (4) and (6). (b) Region within the marked area in (a) enlarged for better visualization enlarged for better visualization and curves plotted with different magnitudes of γ_{APB}.

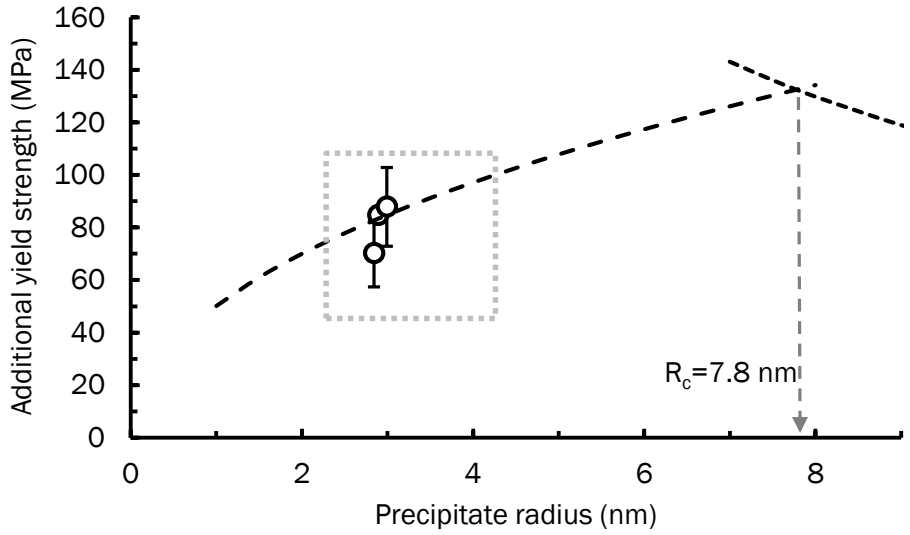

(a)

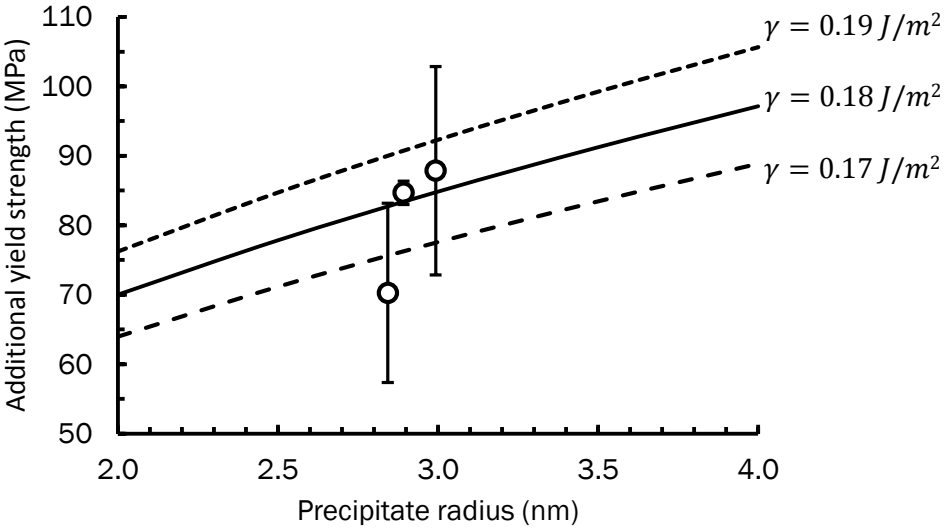

(b)

Fig. 13 Theoretical yield strength increment *vs.* precipitate radius for alloy A3 (a) Orowan strengthening and order strengthening curves calculated from Eqs. (4) and (6). (b) Region within the marked area in (a) enlarged for better visualization enlarged for better visualization and curves plotted with different magnitudes of γ_{APB}.

5. CONCLUSIONS

1. The yield strength of Al alloys that contain Zr and V significantly increases by aging at 400°C. The yield strength of Al-0.8Zr-0.4V alloy is 120 MPa after it is aged at 400°C for 32 hours.

2. During aging, Zr atoms preferentially cluster in locations that are rich in V. Nucleation and growth of Al_3Zr precipitates that have the $L1_2$ crystal structure occurs, and then V, which is a slower diffuser than Zr gradually enters the Al_3Zr particles to form $Al_3(Zr_{1-x}V_x)$. The $Al_3(Zr_{1-x}V_x)$ precipitates also have the $L1_2$ crystal structure and are coherent with the α-aluminum matrix.

3. The coarsening rate of the Al_3Zr precipitates is significantly lowered by adding V to form $Al_3(Zr_{1-x}V_x)$ wherein the V:Zr atom ratio is approximately 1.8. However, the coarsening rate of the $Al_3(Zr_{1-x}V_x)$ precipitates increases when the V:Zr atom ratio exceeds 7. At V concentrations exceeding 7, the V:Zr atom ratio precipitate tends to transform to the $D0_{22}$ crystal structure and the alloy's thermal stability is degraded.

4. The precipitation strengthening mechanism operative in properly aged Al-Zr-V alloys is order strengthening and it is contributed by $Al_3(Zr_{1-x}V_x)$ nono-size precipitates that are coherent with the alloy's matrix and have the $L1_2$ crystal structure.

5. The antiphase boundary energy between the α-Al matrix and the Al_3Zr precipitate, and between the α-Al matrix and the $Al_3(Zr_{1-x}V_x)$ precipitate were determined by an indirect method and found to be 0.185 J/m^2.

REFERENCES

1. *Marquis, E.A. and D.N. Seidman, Coarsening kinetics of nanoscale Al3Sc precipitates in an Al–Mg–Sc alloy. Acta Materialia, 2005.* ***53****(15): p. 4259-4268.*
2. *K.L. Kendig, D.B.M., Strengthening mechanisms of an Al-Mg-Sc-Zr alloy. Acta Materialia, 2002.* ***50****: p. 4165-4175.*
3. *Knipling, K.E., D.C. Dunand, and D.N. Seidman, Precipitation evolution in Al–Zr and Al–Zr–Ti alloys during isothermal aging at 375–425°C. Acta Materialia, 2008.* ***56****(1): p. 114-127.*
4. *Knipling, K.E., D.C. Dunand, and D.N. Seidman, Nucleation and Precipitation Strengthening in Dilute Al-Ti and Al-Zr Alloys. Metallurgical and Materials Transactions A, 2007.* ***38****(10): p. 2552-2563.*
5. *Knipling, K., Precipitation evolution in Al–Zr and Al–Zr–Ti alloys during aging at 450–600°C. Acta Materialia, 2008.* ***56****(6): p. 1182-1195.*
6. *Jia, Z.-h., et al., Precipitation behaviour of Al3Zr precipitate in Al–Cu–Zr and Al–Cu–Zr–Ti–V alloys. Transactions of Nonferrous Metals Society of China, 2012.* ***22****(8): p. 1860-1865.*
7. *Tolley, A., V. Radmilovic, and U. Dahmen, Segregation in Al3(Sc,Zr) precipitates in Al–Sc–Zr alloys. Scripta Materialia, 2005.* ***52****(7): p. 621-625.*

8. *Senkov, O.N., et al., Precipitation of Al3(Sc,Zr) particles in an Al–Zn–Mg–Cu–Sc–Zr alloy during conventional solution heat treatment and its effect on tensile properties. Acta Materialia, 2008.* ***56****(15): p. 3723-3738.*

9. *Radmilovic, V., et al., Monodisperse Al3(LiScZr) core/shell precipitates in Al alloys. Scripta Materialia, 2008.* ***58****(7): p. 529-532.*

10. *Lefebvre, W., et al., Precipitation kinetic of Al3(Sc,Zr) dispersoids in aluminium. Journal of Alloys and Compounds, 2009.* ***470****(1-2): p. 107-110.*

11. *Knipling, K.E., et al., Precipitation evolution in Al–0.1Sc, Al–0.1Zr and Al–0.1Sc–0.1Zr (at.%) alloys during isochronal aging. Acta Materialia, 2010.* ***58****(15): p. 5184-5195.*

12. *Hallem, H., et al., The formation of Al3(ScxZryHf1−x−y)-dispersoids in aluminium alloys. Materials Science and Engineering: A, 2006.* ***421****(1-2): p. 154-160.*

13. *Fuller, C.B., D.N. Seidman, and D.C. Dunand, Mechanical properties of Al(Sc,Zr) alloys at ambient and elevated temperatures. Acta Materialia, 2003.* ***51****(16): p. 4803-4814.*

14. *Fuller, C. and D. Seidman, Temporal evolution of the nanostructure of Al(Sc,Zr) alloys: Part II-coarsening of Al(ScZr) precipitates. Acta Materialia, 2005.* ***53****(20): p. 5415-5428.*

15. *Fuller, C., J. Murray, and D. Seidman, Temporal evolution of the nanostructure of Al(Sc,Zr) alloys: Part I – Chemical compositions of Al(ScZr) precipitates. Acta Materialia, 2005.* ***53****(20): p. 5401-5413.*

16. *Forbord, B., et al., Three dimensional atom probe investigation on the formation of Al3(Sc,Zr)-dispersoids in aluminium alloys. Scripta Materialia, 2004.* ***51****(4): p. 333-337.*

17. *Booth-Morrison, C., D.C. Dunand, and D.N. Seidman, Coarsening resistance at 400°C of precipitation-strengthened Al–Zr–Sc–Er alloys. Acta Materialia, 2011.* ***59****(18): p. 7029-7042.*

18. *Belov, N.A., et al., Optimization of hardening of Al–Zr–Sc cast alloys. Journal of Materials Science, 2006.* ***41****(18): p. 5890-5899.*

19. *Seidman, D.N. and E.A.M. , David C. Dunand, Precipitation strengthening at ambient and elevated temperatures of heat-treatable Al(Sc) alloys. Acta Materialia, 2002.* ***50****: p. 4021-4035.*

20. *van Dalen, M.E., D.C. Dunand, and D.N. Seidman, Nanoscale precipitation and mechanical properties of Al-0.06 at.% Sc alloys microalloyed with Yb or Gd. Journal of Materials Science, 2006.* ***41****(23): p. 7814-7823.*

21. *Singh, V., K. Satya Prasad, and A.A. Gokhale, Effect of minor Sc additions on structure, age hardening and tensile properties of*

aluminium alloy AA8090 plate. Scripta Materialia, 2004. ***50****(6): p. 903-908.*

22. *Fujikawa, S.-I. Impurity diffusion of scandium in aluminium. in Defect and Diffusion Forum. 1997. Trans Tech Publ.*

23. *Y.C. Chen, M.E.F., J.R. Weertman, Coarsening behavior of Ll_2 structured $Al_3(Zr_x V_{1-x})$ precipitates in rapidly solidified Al-Zr-V alloy. Scripta Metallurgica, 1987.* ***21****(7): p. 1003-1008.*

24. *Y.C. Chen, M.E.F., J.R. Weertman, Microstructural evolution and mechanical properties of rapidly solidified Al-Zr-V alloys at high temperatures. Acta Metallurgica et Materialia, 1990.* ***38****(5): p. 771-780.*

25. *Zedalis, M. and M. Fine, Precipitation and ostwald ripening in dilute AI Base-Zr-V alloys. Metallurgical Transactions A, 1986.* ***17****(12): p. 2187-2198.*

26. *Haasen, P., Nucleation and growth of γ'-Precipitates in Ni-14 at.% Al. Acta Metallurgica, 1983.* ***31****(10): p. 1649-1659.*

27. *Murray, J., A. Peruzzi, and J. Abriata, The Al-Zr (aluminum-zirconium) system. Journal of phase equilibria, 1992.* ***13****(3): p. 277-291.*

28. *Murray, J., Al-V (aluminum-vanadium). Bulletin of Alloy Phase Diagrams, 1989.* ***10****(4): p. 351-357.*

29. *Volmer, M. and A. Weber, Keimbildung in ubersattigten Losungen. Zeitschrift für Physikalische Chemie, 1926.* ***119****.*

30. *Marumo, T., S. Fujikawa, and K.-i. Hirano, Diffusion of zirconium in aluminum. J. Jap. Inst. Light Met., 1973.* ***23****(1): p. 17-25.*

31. *Bergner, D. and N. Van Chi, Untersuchungen zur diffusion von 3d-metallen in Al. Wissenschaftliche Zeitschrift der Padagogischen Hochschule, 1977.* ***15****(3).*

32. *Zener, C., Theory of Growth of Spherical Precipitates from Solid Solution. Journal of Applied Physics, 1949.* ***20****(10): p. 950.*

33. *Perez, M., M. Dumont, and D. Acevedo-Reyes, Implementation of classical nucleation and growth theories for precipitation. Acta Materialia, 2008.* ***56****(9): p. 2119-2132.*

34. *Hirsch, P. and F. Humphreys, The Physics and Strength of Plasticity, A. Argon, ed. 1969, MIT Press, Cambridge, MA.*

35. *Ardell, A., Precipitation hardening. Metallurgical Transactions A, 1985.* ***16****(12): p. 2131-2165.*

36. *Meyers, M.A. and K.K. Chawla, Mechanical Metallurgy: Principles and Applications. 1984. Paramus, NJ: Englewood Cliffs, 1982.*

37. *Frost, H.J. and M.F. Ashby, Deformation mechanism maps: the plasticity and creep of metals and ceramics. 1982.*

38. *Melander, A. and P.Å. Persson, The strength of a precipitation hardened AlZnMg alloy. Acta Metallurgica, 1978.* ***26****(2): p. 267-278.*

39. *Nembach, E., How the choice of the dislocations' outer cut-off radius affects the evaluation of precipitation hardening data. Scripta Metallurgica, 1982.* ***16****(11): p. 1261-1265.*

40. *Hyland, R., et al., Al (fcc): Al 3 Sc (L1 2) interphase boundary energy calculations. Acta materialia, 1998.* ***46****(10): p. 3667-3678.*

41. *Phillips, M.A., B.M. Clemens, and W.D. Nix, A model for dislocation behavior during deformation of Al/Al3Sc (fcc/L12) metallic multilayers. Acta Materialia, 2003.* ***51****(11): p. 3157-3170.*

42. *Lefebvre, W., et al., Tracking the path of dislocations across ordered Al3Zr nano-precipitates in three dimensions. Scripta Materialia, 2014.* ***70****: p. 43-46.*

43. *Liu, S., R. Hu, and C. Wang, Electronic and physical properties of Al3VxTi1−x (x=1, 0.875, and 0) alloys. Journal of Applied Physics, 1996.* ***79****(1): p. 214.*

Chapter 5

The Effect of Introducing the Al-Ni Eutectic Composition into Al-Zr-V Alloys on Microstructure and Tensile Properties

Yangyang Fan and Makhlouf M. Makhlouf *

Department of Mechanical Engineering, Worcester Polytechnic Institute, Worcester, MA 01609, USA

Keywords: eutectic, solidification, Al-6Ni, precipitation hardening

ABSTRACT

Adding the Al-6Ni eutectic structure to an Al-0.4Zr-0.4V alloy completely replaces the typical dendritic structure of the alloy by an Al-Al_3Ni eutectic structure. After aging the Al-6Ni-0.4Zr-0.4V alloy at 400°C for 32 hours, which is an optimum heat treatment for this alloy, its yield strength reaches a maximum of 187 MPa. The increased yield strength comes from the eutectic Al_3Ni phase and the $Al_3(Zr_x,V_{1-x})$ precipitates. Theoretical calculations suggest that about 36% of the yield strength is contributed by the $Al_3(Zr_x,V_{1-x})$ precipitate and about 50% is contributed by the Al_3Ni eutectic phase.

* Corresponding author
Tel.: (508) 831-5647 Fax: (508) 831-5992 e-mail: mmm@wpi.edu

1. INTRODUCTION

It has been widely reported that by employing a very fast cooling rate; such as in direct chill casting, the transition metals Sc, Zr, and V may dissolve in aluminum to from supersaturated solid solutions in which the concentration of the transition metal is significantly higher than the maximum solubility indicated by the equilibrium phase diagram [1-6]. Proper aging of these super saturated solid solutions results in the formation of precipitate particles with a chemical composition that corresponds to the general stoichiometric formula Al_3TM, where TM ≡ transition metal. These precipitates, i.e., Al_3Sc, Al_3Zr, and $Al_3(Zr_x,V_{1-x})$, may have an ordered $L1_2$ crystal structure, and therefore they have the potential to be excellent inducers of precipitation hardening in creep-resistant thermally stable aluminum alloys. Fan and Makhlouf [7] have shown that $Al_3(Zr_x,V_{1-x})$ precipitate particles are significantly more thermally stable than Al_3Zr and Al_3V particles; and they are more thermally stable than Al_3Sc particles because scandium diffuses more readily in aluminum than zirconium and vanadium (e.g., at 400°C, $D_{sc} = 1.98\times10^{-17}$ m²/s [8], $D_{Zr} = 1.2\times10^{-20}$ m²/s [9], and $D_V = 4.85\times10^{-24}$ m²/s [10]). However, for the Al-Zr-V system to fulfil its potential in being the basis of aluminum alloys that are useful at elevated temperatures, several major issues have to be resolved. These are: (1) its poor castability, including its insufficient fluidity and its high tendency to hot tear during

solidification, (2) the relatively low solubility of zirconium and vanadium in aluminum ($C_{\alpha p\text{-}Zr}$) ≅ 0.08% wt.% [11], $C_{\alpha p\text{-}V}$ ≅ 0.56% wt.% [12]), which limits the volume fraction of the precipitate phase that forms upon aging, and (3) the rather large equilibrium partition coefficient of the binary aluminum-zirconium and aluminum-vanadium systems ($k_{e(Al\text{-}Zr)} \cong 4$, $k_{e(Al\text{-}V)} \cong 2.5$ [13]), which contributes to excessive microsegregation of zirconium and vanadium in the dendritic structure of the alloy. A possible way of addressing these issues involves introducing a proper eutectic into the Al-Zr-V alloy. Solidification of a eutectic composition does not result in a dendritic structure since it solidifies like a pure metal; i.e., it solidifies at a single temperature – as opposed to solidifying over a temperature range. Moreover, the fluidity of a eutectic composition is superior to that of other compositions since the eutectic composition tends to solidify with a plane front that originates at the walls of the mold and progresses towards its center. Consequently, the stream of molten metal can continue to flow until the freezing fronts meet and close the flow channel. In contrast, compositions that are far from the eutectic tend to form dendrites during solidification. The dendrites, which originate at the walls of the mold and grow inwards towards its center may be fragmented by the flow of the molten metal, and the stream develops as a slurry of tumbling dendritic crystals. Eventually, the dendrites interlock and the flow of molten metal stops. Also, a eutectic composition

has a comparatively longer time during solidification that is available for stress relief; i.e., it exhibits a longer time at which mass feeding can occur. Consequently, eutectic compositions are more resistant to hot tearing than other compositions.

Alas, not all aluminum-based eutectic systems are capable of addressing these issues. Eutectic systems that are appropriate for addition to Al-TM alloys must fulfill three general requirements. (1) Their eutectic temperature should be higher (or at least not much lower) than the peritectic temperature of the Al-TM system, otherwise the eutectic transformation may not occur preferentially. (2) The eutectic structure should enhance the strength of the alloy both at room temperature and at elevated temperatures in order to compensate for the small strengthening increment provided by the Al_3TM phase (low strengthening increment because of its relatively low volume fraction). (3) The eutectic structure should be thermally stable. The aluminum-nickel system has a eutectic composition that meets these requirements. Nickel forms with aluminum a series of nickel aluminides, one of them is Al_3Ni. Aluminum forms a eutectic with Al_3Ni at 6.1 wt. pct. nickel. The melting point of the Al-Al_3Ni eutectic is 640°C and the volume of Al_3Ni in the eutectic structure is relatively large (9.7 vol. pct.); consequently, the Al-Al_3Ni eutectic composition has very good fluidity, and castings made of this material have a low tendency to hot tear [14]. Moreover, the two

eutectic phases in this structure (namely, α-Al and Al_3Ni) are in chemical equilibrium with one another so they are not prone to chemical degradation, and the interface between them has a low energy structure that ensures the thermal stability of the material [7]. Moreover, the two eutectic phases share a strong interfacial bond with one another, which allows efficient load transfer between them. Examination of the portion of the diagram that pertains to the eutectic reaction: $L \leftrightarrow Al + Al_3Ni$, shows that nickel has only very limited solubility in aluminum (about 0.05 wt. pct. at 640°C, and less than 0.005 wt. pct. at 450°C) [15]. Table 1 shows various characteristics of the binary intermetallic compound Al_3Ni which, together with α-Al, are the two phases in this eutectic structure.

Table 1. Characteristics of Al_3Ni.

Stoichiometric composition	0.25 at. pct. Ni
Degree of order	1
Melting type	incongruent
Strukturbericht symbol	$D0_{20}$
Prototype	Al_3Ni
Pearson symbol	oP16
Space group	Pnma

In this publication, we discuss the effect of introducing the Al-Ni eutectic composition on the microstructure and tensile properties of Al-Zr-V alloys.

2. MATERIALS AND PROCEDURES

Al-0.4Zr-0.4V (wt.%) and Al-6Ni-0.4Zr-0.4V (wt.%) alloys were constituted from pure aluminum ingots (99.999% purity), Al-20wt.% Ni, Al-15wt.% Zr, and Al-65wt.% V master alloys. The alloys were melted in an induction furnace in clean silicon carbide crucibles coated with boron nitride. The melts were degassed with high purity argon gas by means of a rotating impeller degasser for 30 minutes, and they were poured at approximately 800°C into a water-chilled copper mold. The water-chilled copper mold produces ASTM standard sub size tensile specimens with a uniform solidification cooling rate of about 120°C/s. The specimens, in their as-cast condition, were aged in an electric furnace and then cooled from the aging temperature to room temperature in air. Although precipitation hardenable aluminum casting alloys are solution heat treated and quenched before they are artificially aged, the Al-0.4Zr-0.4V and Al-6Ni-0.4Zr-0.4V alloys of this study were aged without solutionizing and quenching. This deviation from the norm is dictated by the fact that these alloys are based on peritectic systems wherein a solutionizing heat treatment is not possible without causing incipient melting of the cast part. For these alloys, it is submitted that the liquid is homogenized during melting and the fast cooling rate during solidification replaces the quenching step and preserves the homogeneous super saturated solid solution. As seen in Fig. 1,

microstructure analysis shows that this statement is true for the Al-6Ni-0.4Zr-0.4V alloy, but not necessarily for the Al-0.4Zr-0.4V alloy.

Samples from both alloys were prepared for scanning electron microscopy (SEM) by polishing according to standard metallographic methods. Samples used for transmission electron microscopy (TEM) were produced by thinning foils of the alloys to perforation by means of a twinjet electro-polisher (Fischione Instruments, model 120) operating at 12 volts and utilizing a solution of 10 vol.% perchloric acid in methanol maintained at -20°C. A JOEL-7000F scanning electron microscope operating at 200 kV and a JOEL-2010F transmission electron microscope were used for microstructure analyses.

Room temperature tensile properties of the alloys were measured by means of a Universal Testing machine (Instron model 5500R) at an extension rate of 0.05 in/min. A 1-inch gage length extensometer (MTS model 634.25E-24) was used to measure extension. At least 5 specimens were used in each measurement and the results were averaged and the standard deviations were calculated. Fracture of all specimens took place within the gage length and specimens with severe porosity and/or oxides that would affect the results were excluded.

3. RESLUTS

3.1 Microstructure of the as-cast specimens

Fig. 1 shows SEM photomicrographs and EDS spectra of the as-cast Al-0.4Zr-0.4V and Al-6Ni-0.4Zr-0.4V alloys. The Al-0.4Zr-0.4V specimen was etched in order to reveal the dendritic structure of the alloy. The average secondary dendrite arm spacing was measured and it was found to be 10 μm. At the fast cooling rate employed (120°C/s), the Al-0.4Zr-0.4V alloy is a α-Al solid solution in which formation of primary Al_3Zr and $Al_{10}V$ phases is completely suppressed [4-6]. The Al-6Ni-0.4Zr-0.4V alloy exhibits a eutectic microstructure in which rods of eutectic Al_3Ni are dispersed in aluminum. Similar to the Al-0.4Zr-0.4V alloy, the fast cooling rate employed in casting the Al-6Ni-0.4Zr-0.4V alloy suppresses formation of primary Al_3Zr and Al_3V phases in this specimen. EDS line scanning was performed along the black lines indicated in the photomicrographs in order to detected segregation of zirconium and vanadium. Although EDS results are not very precise, they are accurate enough to indicate the presence of concentration fluctuations, and as such, they have been widely used to detect microsegregation in metallic alloys [2, 3] . Results of the EDS measurements are shown in Figs. 1(c) and (d). Fig. 1(c) shows that the concentration of zirconium and vanadium near the outer periphery of the secondary dendrite arms is significantly lower than that near the core of the secondary dendrite arms. The

standard deviations of the measured zirconium and vanadium concentrations across a typical secondary dendrite arm are respectively ±0.24 and ±0.20. Similar behavior has been observed in Al-Zr-Ti compositions [2, 3]. Fig. 1(d), on the other hand, shows that microsegregation of zirconium and vanadium does not occur in the Al-6Ni-0.4Zr-0.4V alloy. In this case, the standard deviation for the measured zirconium and vanadium concentrations across two typical grains is only ±0.1. Hence, it is submitted that the introduction of the eutectic Al-Al_3Ni structure into the Al-0.4Zr-0.4V composition mitigates the occurrence of zirconium and vanadium microsegration in the as-cast alloy.

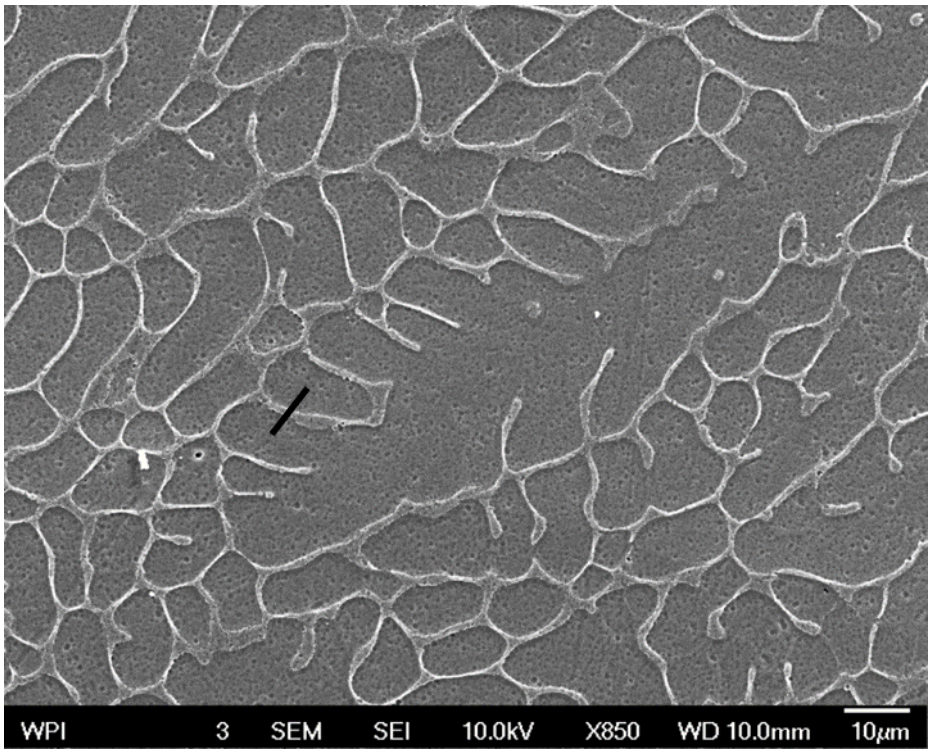

(a)

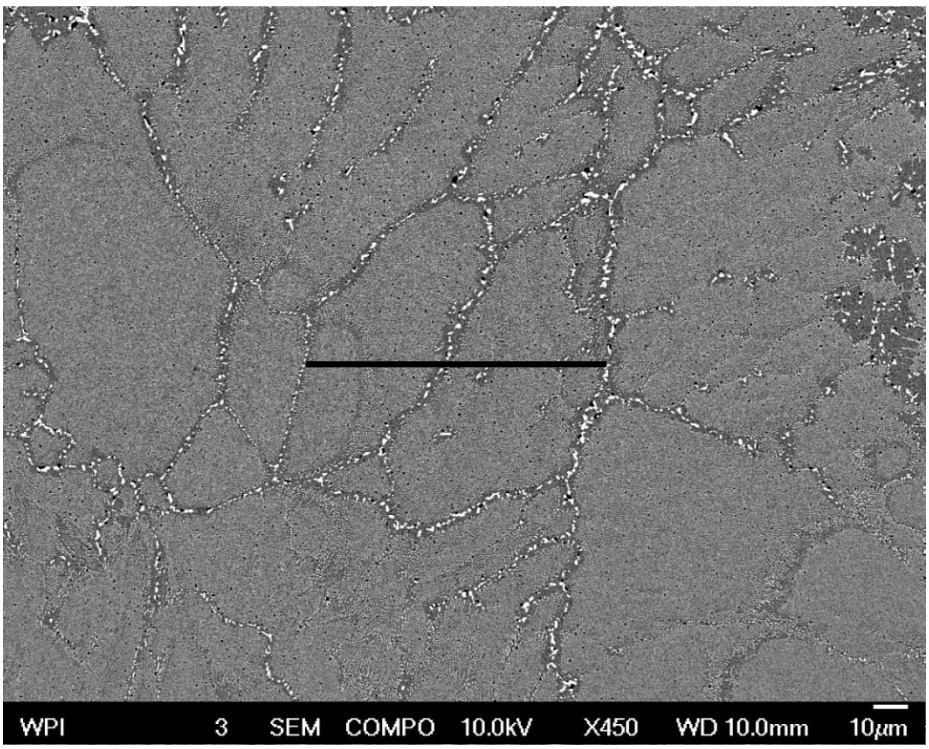
WPI 3 SEM COMPO 10.0kV X450 WD 10.0mm 10μm

(b)

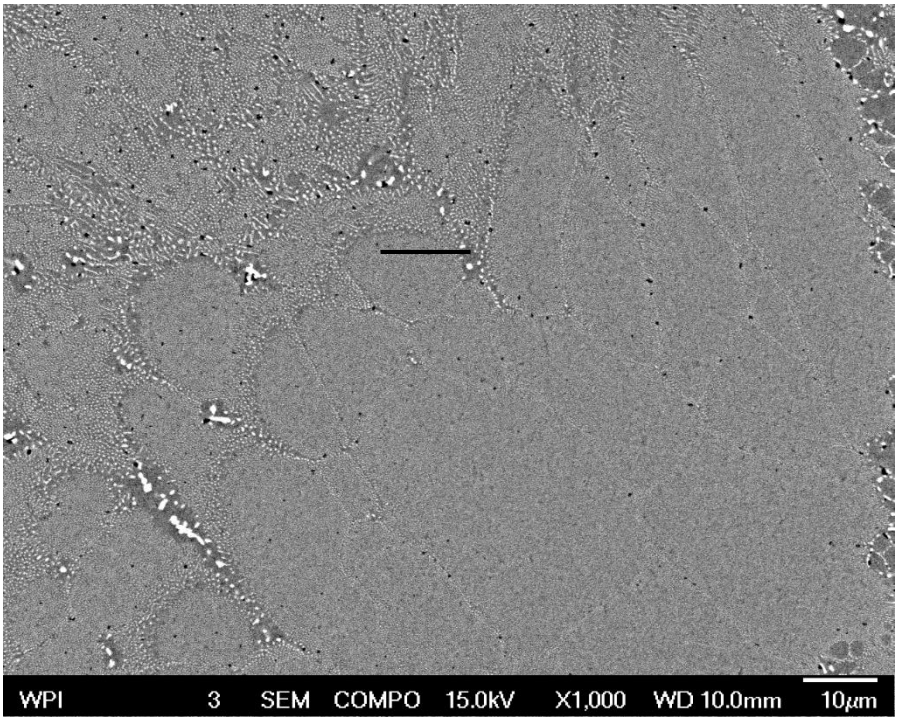
WPI 3 SEM COMPO 15.0kV X1,000 WD 10.0mm 10μm

(c)

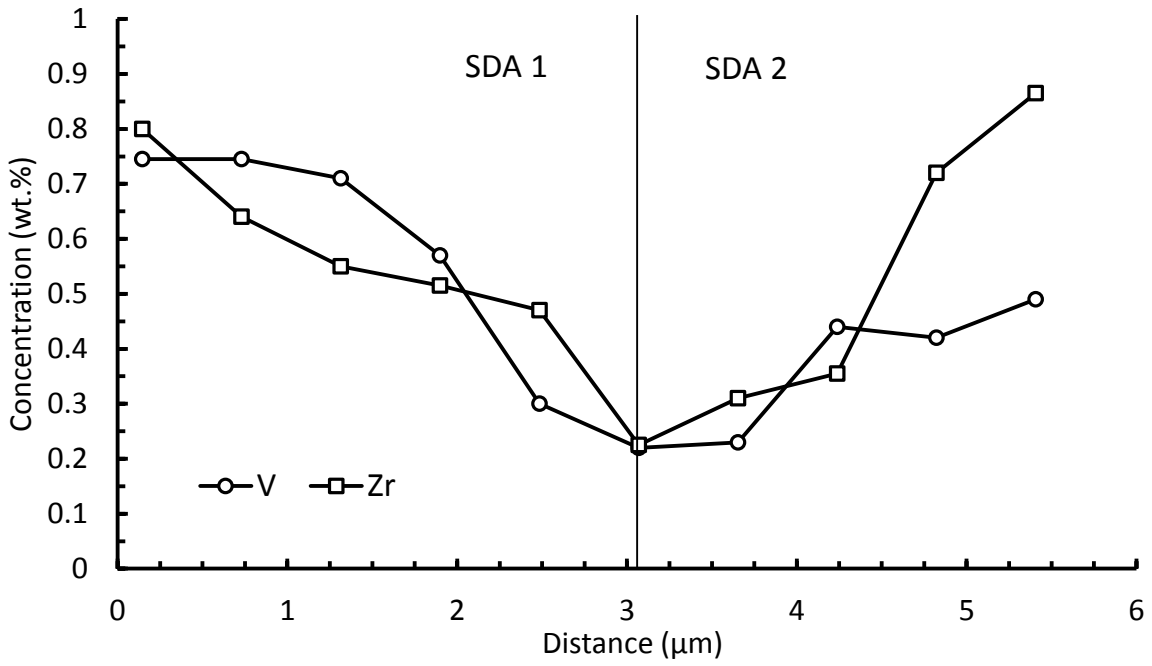
SDA 1
SDA 2
Concentration (wt.%)
Distance (μm)
V
Zr
0
0.1
0.2
0.3
0.4
0.5
0.6
0.7
0.8
0.9
1
0
1
2
3
4
5
6

(d)

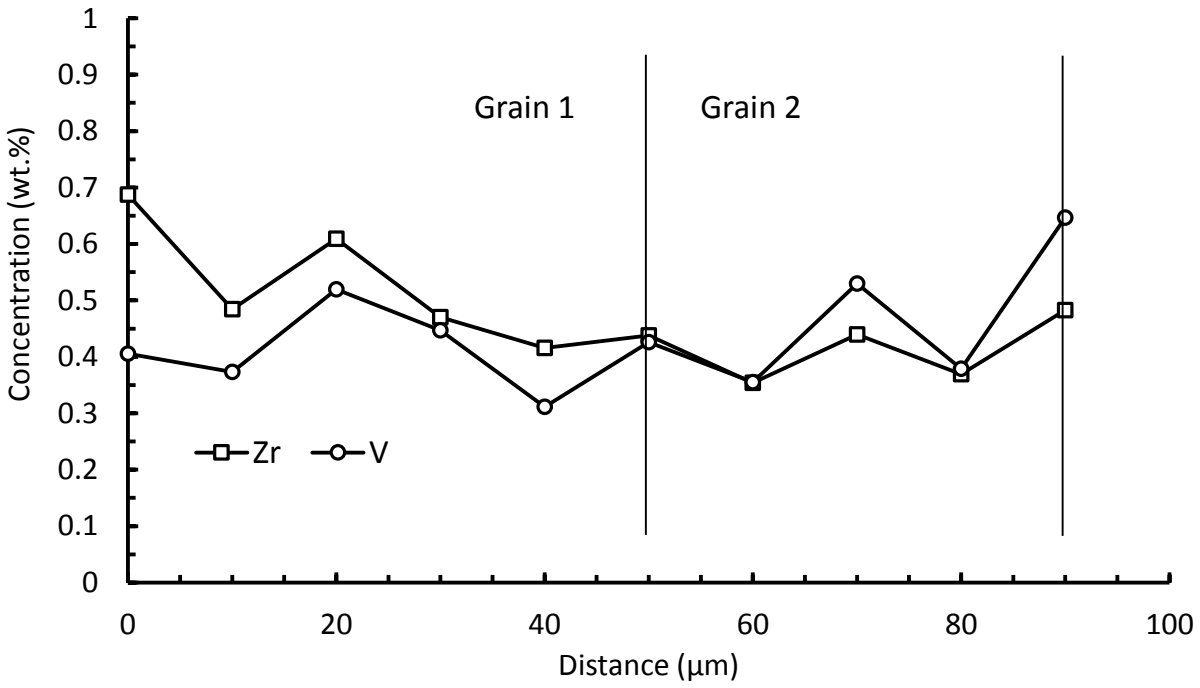
Grain 1
Grain 2
Concentration (wt.%)
Distance (μm)
Zr
V
0
0.1
0.2
0.3
0.4
0.5
0.6
0.7
0.8
0.9
1
0
20
40
60
80
100

(e)

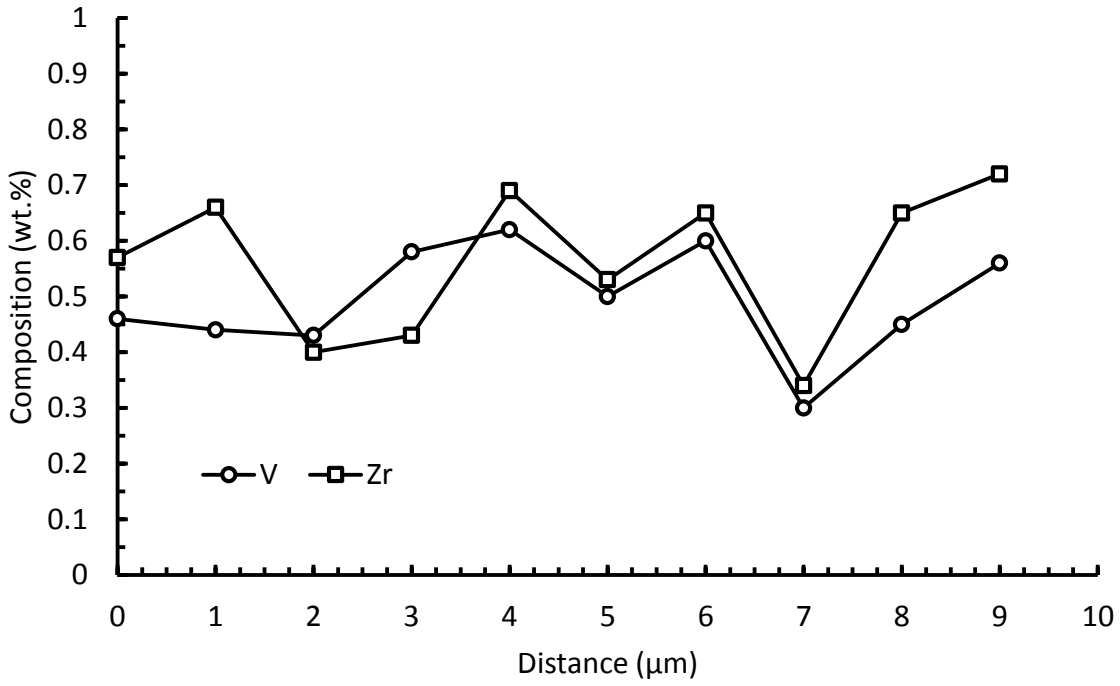

(f)

Fig. 1 SEM photomicrographs of (a) Al-0.4Zr-0.4V, (b) and (c) Al-6Ni-0.4Zr-0.4V specimens; and EDS measurements from (d) the Al-0.4Zr-0.4V, and (e) and (f) the Al-6Ni-0.4Zr-0.4V specimens shown in (a), (b), and (c), respectively.

3.2 Aging response

Fig. 2 shows the variation in yield strength of the Al-0.4Zr-0.4V and Al-6Ni-0.4Zr-0.4V alloys as function of aging time at 400°C. Also shown in Fig. 2 is the yield strength of the Al-6Ni eutectic composition, and a calculated curve obtained by adding the yield strength of the Al-6Ni eutectic to that of the Al-0.4Zr-0.4V alloy. The yield strength of the Al-6Ni eutectic is 95 MPa and is more or less constant with aging time. This is mainly due to the good thermal stability of the Al_3Ni rods at elevated temperatures [16]. At the beginning of aging, most of the zirconium and vanadium in both the Al-6Ni-0.4Zr-0.4V alloy and the Al-0.4Zr-0.4V alloy

are in solid solution with the aluminum matrix. Because both alloys contain the same amount of these elements, their yield strength is increased by the same increment (40 MPa) over the base yield strength of their respective compositions. This increment of strength is due to solid solution effects. After about 4 hours at 400°C, the yield strength of both the Al-0.4Zr-0.4V alloy and the Al-6Ni-0.4Zr-0.4V alloy continue to increase sharply until eventually (after 32 hours), it reaches its peak value. Beyond 32 hours, the yield strength of both alloys levels off and remains constant with aging time. This sharp increase in yield strength is attributed to precipitation of $Al_3(Zr_x,V_{1-x})$ nano-sized particles in the alloy's matrix [4-6]. Unlike the strengthening increment caused by solid solution effects, which is the same for both alloys, precipitation hardening effects is different in the two alloys. This is evidenced by the different magnitudes of maximum yield strength for the Al-6Ni-0.4Zr-0.4V alloy (187 MPa) and the calculated curve obtained by adding the yield strength of the Al-6Ni eutectic to that of the Al-0.4Zr-0.4V alloy (157 MPa). It is submitted that precipitation strengthening by $Al_3(Zr_x,V_{1-x})$ particles is more potent in the Al-6Ni-0.4Zr-0.4V alloy than in the Al-0.4Zr-0.4V alloy.

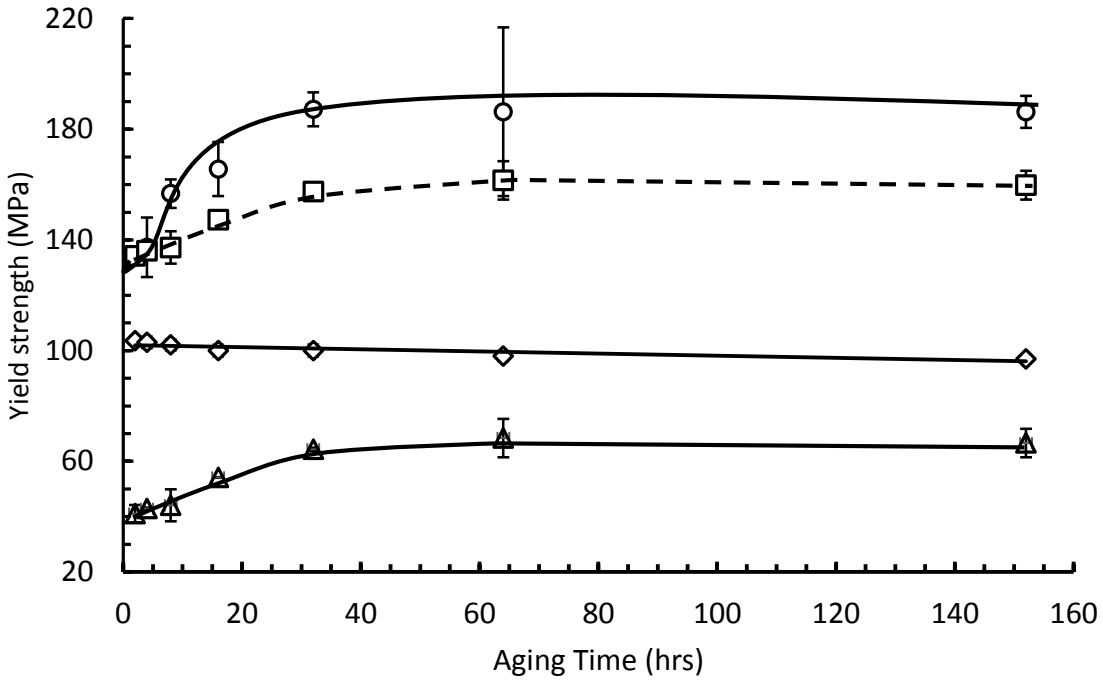

Fig. 2 Variation of yield strength of the Al-0.4Zr-0.4V (△) alloy, the Al-6Ni-0.4Zr-0.4V (○) alloy, the Al-6Ni eutectic composition (◇), and a calculated curve obtained by adding the yield strength of the Al-6Ni eutectic to that of the Al-0.4Zr-0.4V alloy (□) all as functions of aging time at 400°C.

3.3 Precipitation in Al-6Ni-0.4Zr-0.4V alloy

Fig. 3 shows photomicrographs of the Al-6Ni-0.4Zr-0.4V alloy that was aged at 400°C for 32 hours. The microstructure of the Al-Al_3Ni eutectic is shown in Fig. 3(a). The Al_3Ni phase appears as long thin rods with an average diameter of about 100 nm and a length that varies between 1 and 10 μm. The Al_3Ni rods within any given grain are well aligned, which suggests that they have a specific orientation relationship with the α-Al matrix. Fig. 3(b) is a TEM photomicrograph of the same alloy and shows that very fine particles (approximately 5 nm in average diameter) are present in the eutectic aluminum phase that is between the eutectic Al_3Ni rods. Fig. 4 shows a select area diffraction pattern (SADP) of a

typical precipitate particle together with its surrounding eutectic aluminum. A super lattice diffraction pattern contributed by an $L1_2$ crystal structure is clearly seen in Fig. 4. Precipitation in Al-Zr-V alloys has been extensively investigated [4-6], and it is believed that coherent $L1_2$- $Al_3(Zr_x,V_{1-x})$ particles do indeed form in these alloys when the alloys are aged between 375 and 450°C for sufficient time.

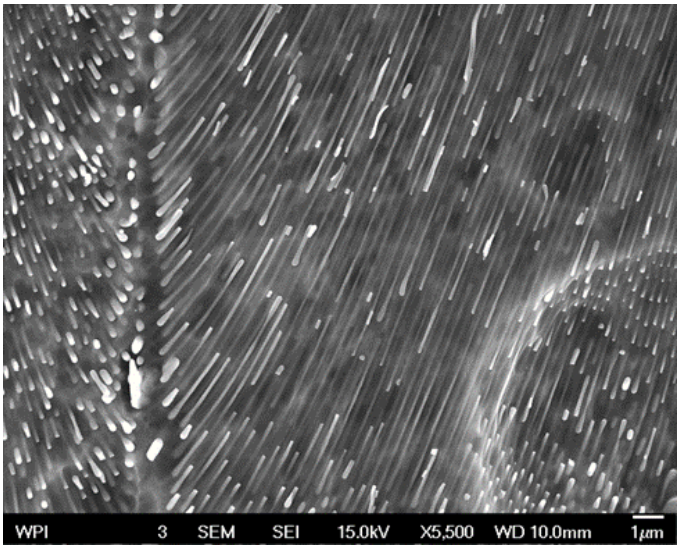

(a)

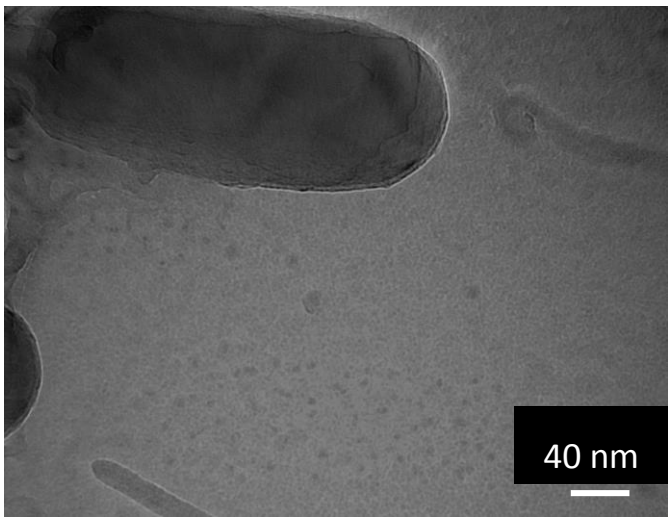

(b)

Fig. 3 Microstructure of Al-6Ni-0.4Zr-0.4V alloy that has been aged at 400°C for 32 hours. (a) SEM photomicrograph showing the Al-Al_3Ni eutectic, and (b) TEM photomicrograph showing that very fine particles form in between the eutectic Al_3Ni fibers.

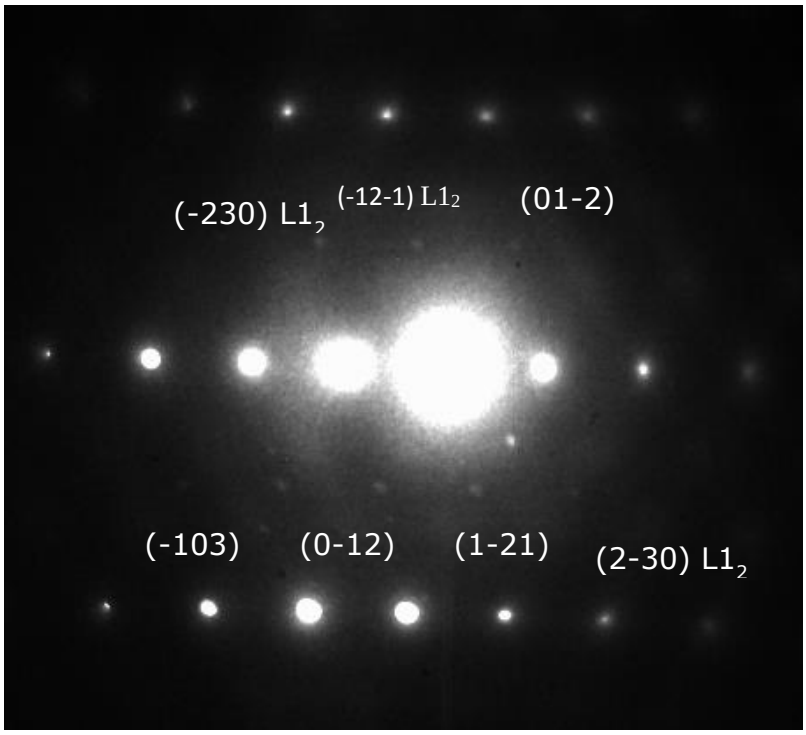

(a)

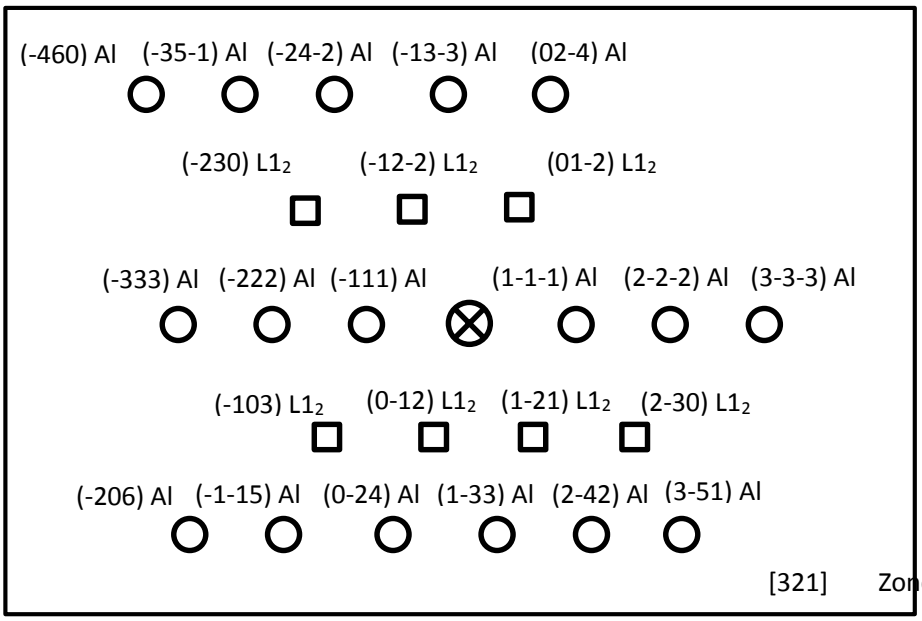

(b)

Fig. 4 (a) SADP from the area marked in Fig. 3(b), (b) indexing of the SADP.

3.4 Coarsening of the $Al_3(Zr_x,V_{1-x})$ precipitate in Al-6Ni-0.4Zr-0.4V and Al-0.4Zr-0.4V alloys

Fig. 5 shows typical TEM photomicrographs of the Al-6Ni-0.4Zr-0.4V and Al-0.4Zr-0.4V alloys. Both specimens used to produce Fig. 5 were aged at 400°C for 32 hours and then soaked at 350°C for 100 hours. As Fig. 5(a) shows, the $Al_3(Zr_x,V_{1-x})$ precipitate that forms in the Al-0.4Zr-0.4V alloy upon aging tend to be more concentrated within the core of the dendrite arms while the precipitate density at the outer periphery of the dendrite arms is significantly lower. Moreover, the average size of the precipitate particles near the center of the dendrite arm is significantly larger than that at the periphery of the dendrite arms. On the other hand, as Fig. 5(b) shows, the $Al_3(Zr_x,V_{1-x})$ precipitate particles that form in the Al-6Ni-0.4Zr-0.4V alloy are uniformly distributed throughout the matrix and their average size is slightly smaller than the average size of the precipitate particles that form in the Al-0.4Zr-0.4V alloy. More than 200 precipitate particles were analyzed in each alloy and the average particle radius in the Al-0.4Zr-0.4V and Al-6Ni-0.4Zr-0.4V alloys were calculated to be 2.8 nm and 2.6 nm, respectively. Fig. 6 shows the particle size distribution in the two alloys. The precipitate particles in the Al-6Ni-0.4Zr-0.4V alloy are more uniform in size than those in the Al-0.4Zr-0.4V alloy. More than 55% of the precipitate particles in the Al-6Ni-0.4Zr-0.4V alloy are close to the mean precipitate radius and there is less than 1 nm

difference between any measured particle radius and the mean radius. On the other hand, in the Al-0.4Zr-0.4V alloy, only about 37% of the precipitate particles are close to the mean precipitate radius.

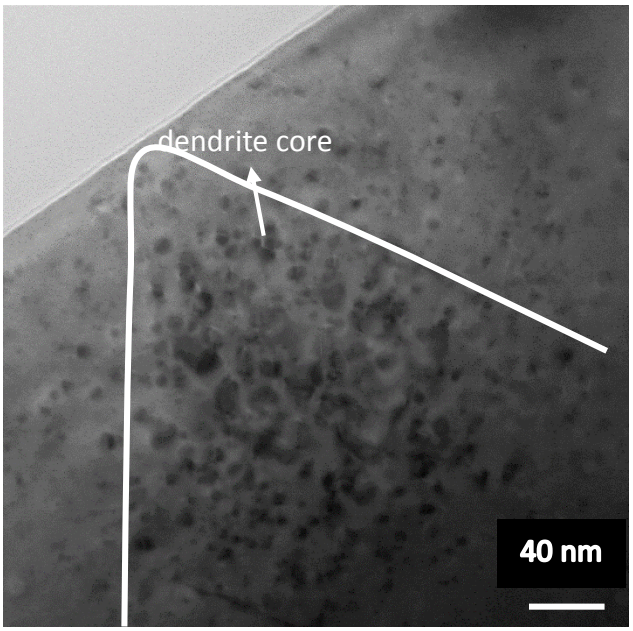

(a)

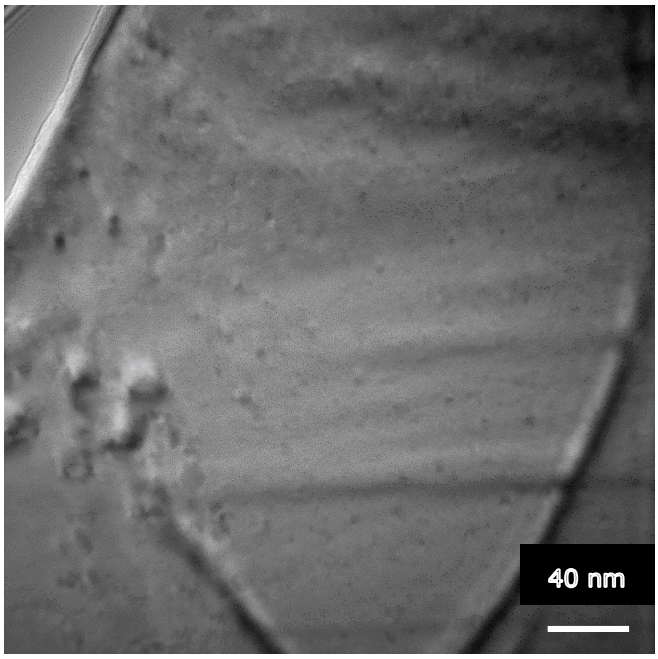

(b)

Fig. 5 (a) TEM picture of Al-0.4Zr-0.4V alloy; (b) TEM picture of Al-6Ni-0.4Zr-0.4V alloy. Both of the alloys were aged at 400°C for 32 hours and then are soaked at 350°C for 100 hours.

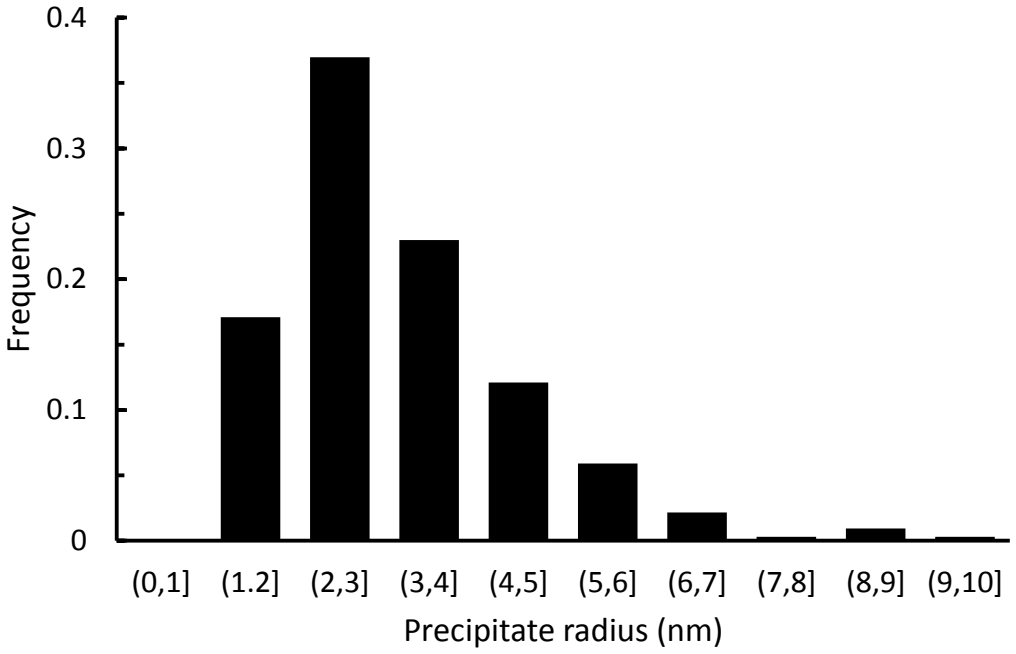

(a)

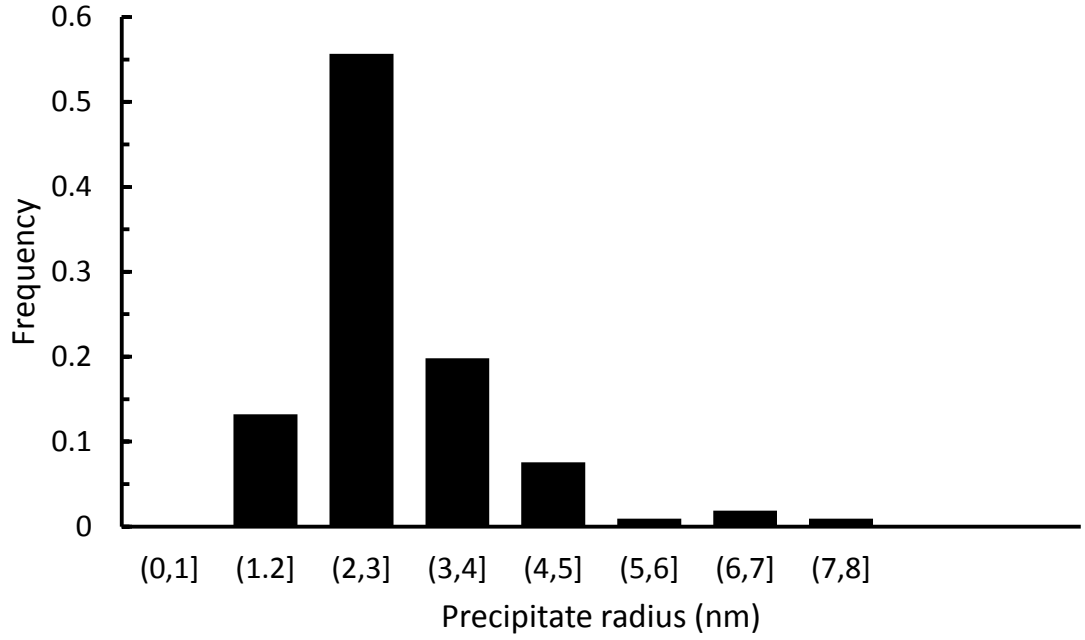

(b)

Fig. 6 (a) Precipitate size distribution in (a) Al-0.4Zr-0.4V alloy, and (b) Al-6Ni-0.4Zr-0.4V alloy. Both alloys were aged at 400°C for 32 hours and then soaked at 350°C for 100 hours.

4. DISCUSSION

4.1 Microsegregation of zirconium and vanadium in Al-Zr-V alloys

It is well established that when the cooling rate is fast enough, solidification of peritectic systems will deviate considerably from equilibrium [17, 18]; and hence a non-equilibrium phase diagram, rather than an equilibrium one should be employed. The following findings help us sketch the non-equilibrium phase diagram for the Al-TM system (Fig. 7). (1) Fig. 1 shows that the concentration of TM at the middle of the typical dendrite arm is higher than the initial concentration of TM in the alloy. This suggests that when the system solidifies under non-equilibrium conditions, the maximum solubility of TM moves towards the solute rich region of the non-equilibrium phase diagram, i.e., $C'_{\alpha p} > C_{\alpha p}$. (2) Also, Fig. 1 shows that because of the fast cooling rate employed during solidification, primary phases did not form in the as-cast alloy. This indicates that the liquidus of the system (shown as a dotted line in Fig. 7) is to the right of the initial alloy composition, and there is no peritectic reaction plateau, i.e., $C'_{Lp} > C_o$. (3) $C'_{\alpha p}$ and C'_{Lp} depend on the solidification cooling rate in such a way that an increase in the solidification cooling rate results in an increase the solubility limit of the TM in aluminum.

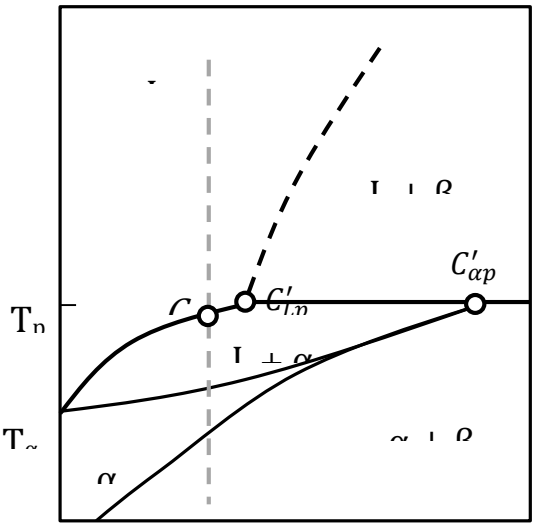

Fig. 7 Non-equilibrium phase diagram of a hypothetical peritectic alloy.

Because the solidification rate is very fast, the Scheil equation shown as Eq. (1) may be used to calculate the concentration profiles of zirconium and vanadium in the Al-Zr-V alloy [13]

$$C_s = k' C_0 (1 - f_s)^{(k'-1)} \tag{1}$$

Eq. (1) was fitted to the measured zirconium and vanadium concentration profiles (Figs. 1(c)) in order to yield the non-equilibrium partition coefficient, k'. Fig. 8 shows the measured concentrations of zirconium and vanadium across a dendrite arm together with the concentration profile calculated by the Scheil equation. Because the shape of the dendrite arm closely resembles a straight cylinder, the solid fraction (f_s) in Eq. (1) may be approximated by r^2/r_0^2 where r is the distance measured from the center of a dendrite arm and r_0 is the radius of the dendrite arm. With this approximation, the non-equilibrium partition coefficient for

vanadium, k'_V is determined to be 2.0 and that for zirconium, k'_{Zr} is determined to be 1.6. The non-equilibrium partition coefficient for zirconium is in good agreement with that determined by Roson [13] who reports the non-equilibrium partition coefficient of zirconium in directly chilled Al-Zr-Sc alloys to be 1.4. Comparing these values of non-equilibrium partition coefficients with their equilibrium counterparts (k_V = 4 [12], k_{Zr} = 2.5 [11]), it is submitted that the partition coefficients of zirconium and vanadium in the Al-Zr-V system decrease significantly with increasing solidification cooling rate.

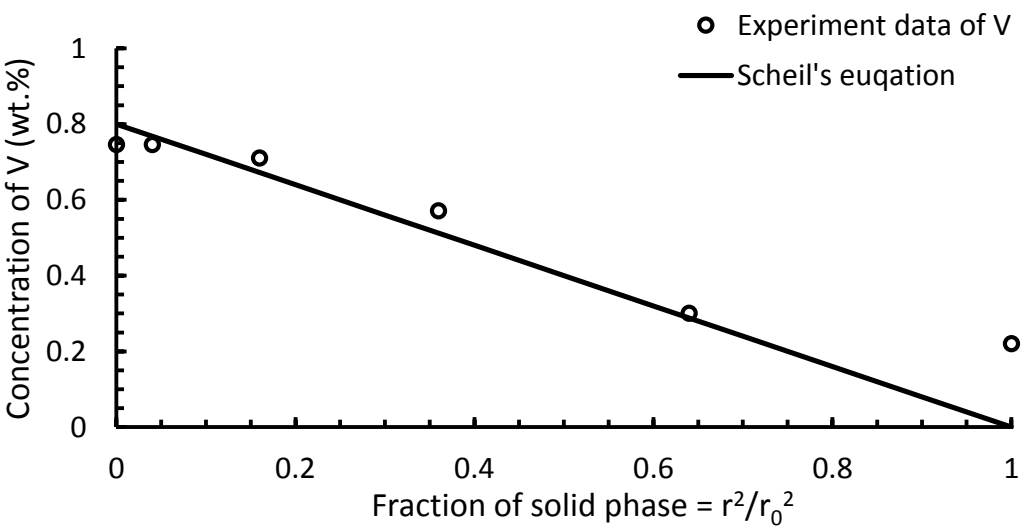

(a)

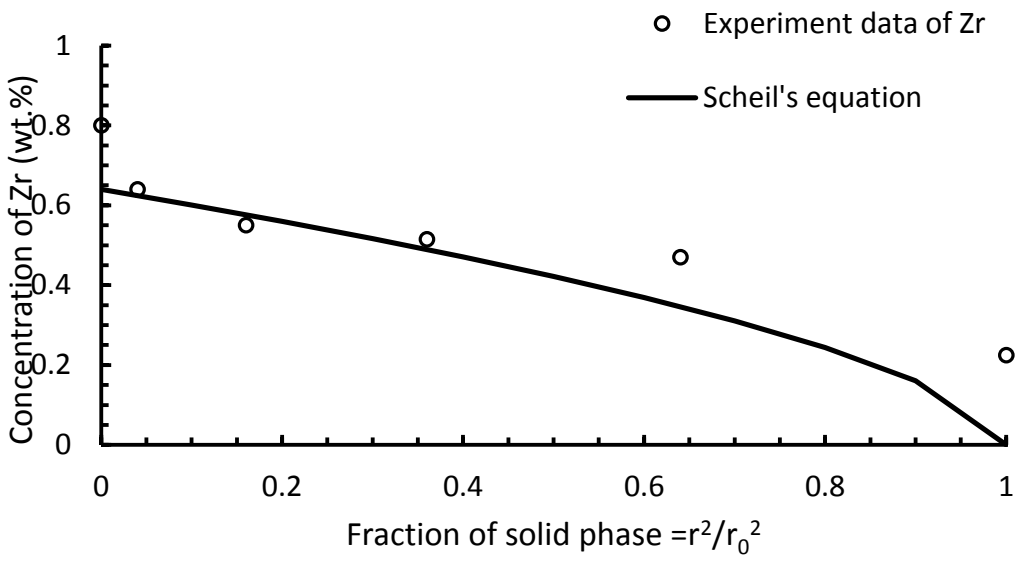

(b)

Fig. 8 Measured and predicted (with the Scheil's equation) concentration of (a) vanadium and (b) zirconium within in a dendrite arm.

4.2 The effect of zirconium and vanadium concentration distribution on precipitate coarsening

The coarsening rate of a precipitate particle can be determined from Eq. (2) [13]:

$$\frac{\mathrm{d}r}{\mathrm{d}t} = \frac{D_{Zr}}{r}\frac{C_{Zr} - C_{Zr}^{\alpha}(r)}{C_{Zr}^{\beta} - C_{Zr}^{\alpha}(r)} = \frac{D_V}{r}\frac{C_V - C_V^{\alpha}(r)}{C_V^{\beta} - C_V^{\alpha}(r)} \tag{2}$$

where D is the diffusion coefficient of zirconium or vanadium in aluminum, C is the concentration in the far field matrix, $C^{\alpha}(r)$ is the interfacial concentration of zirconium or vanadium in the matrix (which is a function of the particle radius because of the Gibbs-Thomson effect), and C^{β} is the concentration of zirconium or vanadium in the precipitate. Eq. (2) indicates that a higher matrix concentration, C, results in a faster

coarsening rate. Therefore when the solute element is strongly segregated, the range of precipitate particle size will be wide.

Eq. (3) was used to calculate the particle distribution functions [6]

$$\rho^2 h(\rho) = \frac{N(r, r+\Delta r)}{\Sigma N(r, r+\Delta r)} \frac{\bar{r}}{\Delta r} \frac{9}{4} \tag{3}$$

In Eq. (3), $\rho = r/\bar{r}$ where r is the radius of the precipitate particle and $\bar{r}$ is the average radius of precipitate particles.

According to the Lifshitz, Slyozov, and Wagner (LSW) theory, the size distribution of precipitates in a dilute system is given by Eq. (4) [6]

$$h(\rho) = \left[\frac{3}{\rho+3}\right]^{7/3} \left[-\frac{1.5}{\rho-1.5}\right]^{11/3} \exp\left(\frac{\rho}{\rho-1.5}\right), \qquad h(\rho) \tag{4}$$
$$= 0 \text{ except for } \rho < 1.5$$

Fig. 9 shows the measured precipitate particle size distribution together with the distribution calculated with Eq. (4) for both the Al-0.4Zr-0.4V and the Al-6Ni-0.4Zr-0.4V alloys. The measured particle size distribution fits the LSW function well in the case of the Al-6Ni-0.4Zr-0.4V alloy, but for the Al-0.4Zr-0.4V alloy, the measured size distribution deviates significantly from the LSW function. This may be due to the fact that the LSW distribution does not account for the initial segregation of solute elements, which is prevalent in the Al-0.4Zr-0.4V alloy. It is submitted that the Al-6Ni-0.4Zr-0.4V alloy because of its more uniform distribution of precipitate particles is more thermally stable than the Al-0.4Zr-0.4V

alloy. This is explained in terms of Ostwald ripening, which postulates that when an inhomogeneous structure is held at an elevated temperature for sufficient time, energetic factors will cause the larger precipitate particles to grow by drawing material from the smaller ones, which, in turn, shrink.

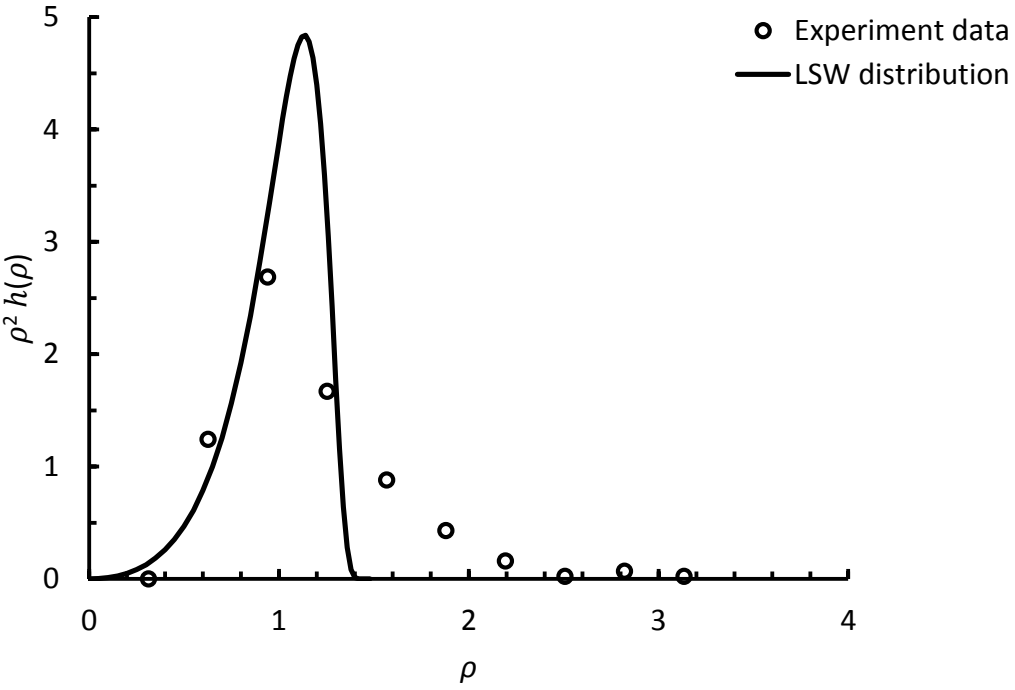

(a)

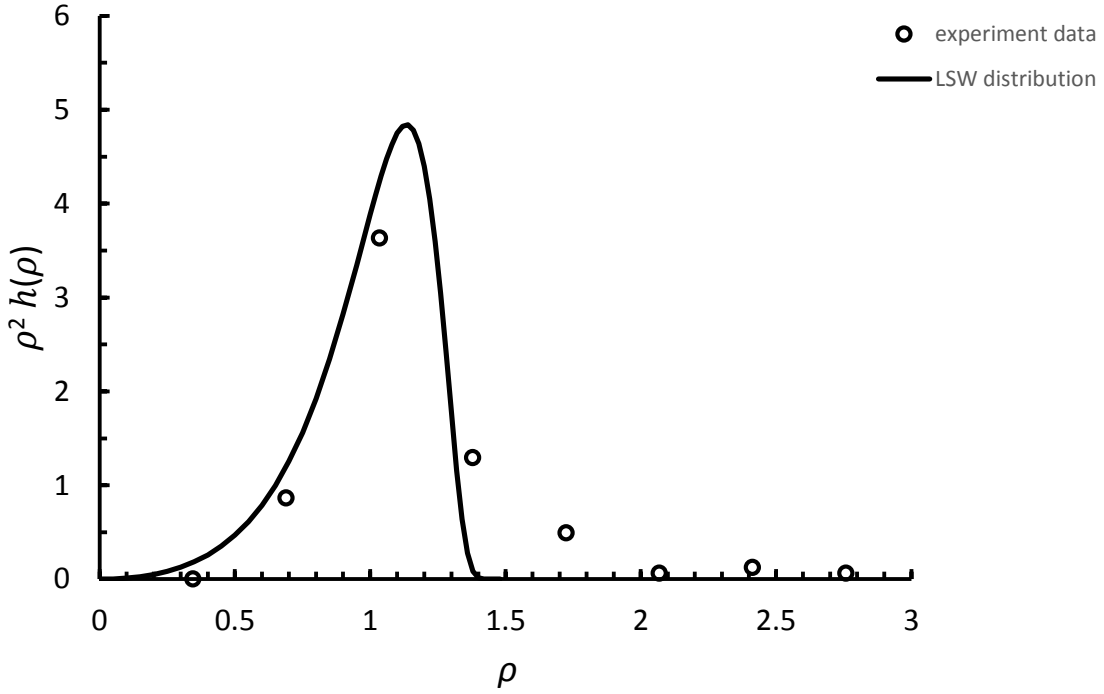

(b)

Fig. 9 (a) Measured and calculated size distribution of $Al_3(Zr_x,V_{1-x})$ precipitates in (a) the Al-0.4Zr-0.4V alloy and (b) the 6Ni-0.4Zr-0.4V alloy.

4.3 Tensile strength of the Al-6Ni-0.4Zr-0.4V *alloy*

Three different phases contribute to the strength of the Al-6Ni-0.4Zr-0.4V alloy. These are the α-Al phase, the Al_3Ni eutectic phase, and the $Al_3(Zr_x,V_{1-x})$ precipitate particles, and the strength of the alloy may be expressed as a linear combination of these contributions as shown in Eq. (5)

$$\sigma_{Total} = \sigma_{Al} + \Delta\sigma_{Al_3Ni} + \Delta\sigma_{Al_3(Zr,V)} \quad (5)$$

Since the solubility of zirconium, vanadium, and nickel in solid aluminum is negligible, then the yield strength of the α-Al phase may be assumed equal to the yield strength of pure aluminum, so that $\sigma_{Al} =$ 28 MPa [19].

The Al_3Ni eutectic rods are approximately 100 nm in diameter and several micrometers in length, so they tend to strengthen the α-Al phase by the Orowan looping mechanism. They contribute a strengthening increment, $\Delta\sigma_{Al_3Ni}$ given by Eq. (6) [7]:

$$\Delta\sigma_{Al_3Ni} = \frac{M(1+\frac{1}{\sqrt{1-\nu}})}{2}\frac{0.926Gb}{2\pi\left(\sqrt{\pi}\frac{R}{\sqrt{f_{Al_3Ni}}}-2r\right)}\ln\left(\frac{r}{b}\right) \quad (6)$$

In Eq. (6), M is the Taylor factor, for aluminum M = 2.6 [20]; G is shear modulus on the slip plane, for aluminum G = 26.2 GPa; ν is Poisson's ratio, for aluminum ν = 0.362; b is Burger's vector, for aluminum b = 0.286 nm; and r is the average radius of the Al_3Ni rods.

The $Al_3(Zr_x,V_{1-x})$ precipitate particles have an ordered $L1_2$ crystal structure, and they contribute a strengthening increment, $\Delta\sigma_{order}$ given by Eq. (7) [21]:

$$\Delta\sigma_{order} = \mathrm{M}\frac{\gamma_{apb}}{2b}\left[\left(\frac{3\pi^2\gamma_{apb}f<r>}{32\Gamma}\right)^{\frac{1}{2}}-f\right] \quad (7)$$

In Eq. (7), γ_{apb} is the anti-phase boundary energy between the precipitate and the aluminum matrix, γ_{apb} = 0.185 J/m^2 [7]; f is the volume fraction of precipitate particles; <r> is the mean radius of the precipitate particles, which was determined to be 2.5 nm for the optimally aged Al-6Ni-0.4Zr-0.4V alloy; Γ is the line tension in a dislocation given

by eq. (8) [21]:

$$\Gamma = \frac{Gb^2}{4\pi}\left[\frac{1+\nu-3\nu sin^2\xi}{1-\nu}\right]\ln(\frac{\Lambda}{r_0}) \quad (8)$$

ξ is the angle between the dislocation line and the precipitate particle. It is usually assumed that edge dislocations dominate movement on the slip planes, so that $\xi = \pi/2$ [21]; r_0 is the inner-cut dislocation radius and $r_0 \cong 2b$ [21]. Λ is the outer-cut dislocation radius, and is given by Eq. (9) [22]:

$$\Lambda = \frac{4 < r >}{3f} - 2 < r > \quad (9)$$

Combing Eqs. (5) to (9) and substituting the appropriate values, the theoretical yield strength of the optimally aged Al-6Ni-0.4Zr-0.4V alloy is calculated to be 211 MPa; of which the Al_3Ni phase contributes 107 MPa and the $Al_3(Zr_x,V_{1-x})$ particles contribute 77 MPa. This calculated yield strength is in good agreement with the measured yield strength (187 MPa) considering that cast specimens invariably contain strength-reducing defects (e.g., pores, unwanted phases, etc.) that are not accounted for in the equations used to calculate strengthening increments.

5. CONCLUSIONS

1. With the addition of the Al-6Ni eutectic phase to an Al-0.4Zr-0.4V alloy, the typical dendritic structure of the alloy is completely replaced by an Al-Al_3Ni eutectic structure.

2. Zirconium and vanadium strongly segregate within the dendrites in the fast cooled Al-0.4Zr-0.4V alloy. The non-equilibrium partition coefficient of zirconium was measured to be 1.6 and that of vanadium was measured to be 2.0. Nevertheless, zirconium and vanadium are uniformly distributed in the α-Al eutectic phase of the Al-6Ni-0.4Zr-0.4V alloy.

3. Due to the significant segregation of zirconium and vanadium in the as-cast Al-0.4Zr-0.4V alloy and the lack thereof in the Al-6Ni-0.4Zr-0.4V alloy, the $Al_3(Zr_x,V_{1-x})$ precipitate particles that form in the Al-6Ni-0.4Zr-0.4V alloy tend to be more resistant to coarsening than those that form in the Al-0.4Zr-0.4V alloy. This difference in coarsening tendency is explained in view of Ostwald ripening, which favors coarsening of larger precipitate particles at the expense of smaller ones.

4. After aging the Al-6Ni-0.4Zr-0.4V alloy at 400°C for 32 hours, which is an optimum heat treatment for this alloy, its yield strength reaches a maximum of 187 MPa. The increased yield strength comes from the

eutectic Al_3Ni phase and the $Al_3(Zr_x,V_{1-x})$ precipitates. Theoretical calculations suggest that about 36% of the yield strength is contributed by the $Al_3(Zr_x,V_{1-x})$ precipitate and about 50% is contributed by the Al_3Ni eutectic phase.

REFERENCES

1. Ryum, N., *Precipitation and recrystallization in an A1-0.5 WT.% Zr-alloy.* Acta Metallurgica, 1969. **17**(3): p. 269-278.
2. Knipling, K.E., D.C. Dunand, and D.N. Seidman, *Nucleation and Precipitation Strengthening in Dilute Al-Ti and Al-Zr Alloys.* Metallurgical and Materials Transactions A, 2007. **38**(10): p. 2552-2563.
3. Knipling, K.E., D.C. Dunand, and D.N. Seidman, *Precipitation evolution in Al–Zr and Al–Zr–Ti alloys during isothermal aging at 375–425°C.* Acta Materialia, 2008. **56**(1): p. 114-127.
4. Y.C. Chen, M.E.F., J.R. Weertman, *Coarsening behavior of Ll_2 structured $Al_3(Zr_x\ V_{1-x})$ precipitates in rapidly solidified Al-Zr-V alloy.* Scripta Metallurgica, 1987. **21**(7): p. 1003-1008.
5. Y.C. Chen, M.E.F., J.R. Weertman, *Microstructural evolution and mechanical properties of rapidly solidified Al-Zr-V alloys at high temperatures.* Acta Metallurgica et Materialia, 1990. **38**(5): p. 771-780.

6. Zedalis, M. and M. Fine, *Precipitation and ostwald ripening in dilute AI Base-Zr-V alloys*. Metallurgical Transactions A, 1986. **17**(12): p. 2187-2198.

7. Fan, Y., *Alloying Aluminum with Transitional Metals, Ph.D. disseration* W.P. Institute, Editor. 2015.

8. Fujikawa, S.-I. *Impurity diffusion of scandium in aluminium*. in *Defect and Diffusion Forum*. 1997. Trans Tech Publ.

9. Marumo, T., S. Fujikawa, and K.-i. Hirano, *Diffusion of zirconium in aluminum*. J. Jap. Inst. Light Met., 1973. **23**(1): p. 17-25.

10. Bergner, D. and N. Van Chi, *Untersuchungen zur diffusion von 3d-metallen in Al*. Wissenschaftliche Zeitschrift der Padagogischen Hochschule, 1977. **15**(3).

11. Murray, J., A. Peruzzi, and J. Abriata, *The Al-Zr (aluminum-zirconium) system*. Journal of phase equilibria, 1992. **13**(3): p. 277-291.

12. Murray, J., *Al-V (aluminum-vanadium)*. Bulletin of Alloy Phase Diagrams, 1989. **10**(4): p. 351-357.

13. Robson, J.D., *A new model for prediction of dispersoid precipitation in aluminium alloys containing zirconium and scandium*. Acta Materialia, 2004. **52**(6): p. 1409-1421.

14. Eskin, D.G. and L. Katgerman, *A Quest for a New Hot Tearing Criterion.* Metallurgical and Materials Transactions A, 2007. **38**(7): p. 1511-1519.

15. Du, Y. and N. Clavaguera, *Thermodynamic assessment of the Al□ Ni system.* Journal of alloys and compounds, 1996. **237**(1): p. 20-32.

16. Smartt, H., L. Tu, and T. Courtney, *Elevated temperature stability of the Al− Al3Ni eutectic composite.* Metallurgical Transactions, 1971. **2**(9): p. 2717-2727.

17. Kerr, H. and W. Kurz, *Solidification of peritectic alloys.* International materials reviews, 1996. **41**(4): p. 129-164.

18. John, D.S. and L. Hogan, *Thermal analysis of peritectic alloys.* Journal of Materials Science, 1982. **17**(8): p. 2413-2418.

19. Frost, H.J. and M.F. Ashby, *Deformation mechanism maps: the plasticity and creep of metals and ceramics.* 1982.

20. Meyers, M.A. and K.K. Chawla, *Mechanical Metallurgy: Principles and Applications. 1984.* Paramus, NJ: Englewood Cliffs, 1982.

21. Ardell, A., *Precipitation hardening.* Metallurgical Transactions A, 1985. **16**(12): p. 2131-2165.

22. Nembach, E., *How the choice of the dislocations' outer cut-off radius affects the evaluation of precipitation hardening data.* Scripta Metallurgica, 1982. **16**(11): p. 1261-1265.

Chapter 6

Stabilizing the $Al_{12}Mn$ Precipitates in Al-Mn Alloys by Alloying with Tungsten

Yangyang Fan and Makhlouf M. Makhlouf *

Department of Mechanical Engineering, Worcester Polytechnic Institute, Worcester, MA 01609, USA

Keywords: aluminum alloys, precipitation strengthening, coarsening kinetics, thermal stability

ABSTRACT

The Al-Mn-W system has considerable potential as basis for lightweight aluminum alloys that are intended for use at temperatures approaching 350°C. In this ternary system, aluminum, manganese, and tungsten co-precipitate to form the meta-stable $Al_{12}(Mn_{(1-x)}W_x)$ phase, which is thermally stable and will not coarsen when held at elevated temperatures for extended periods of time. This enhanced thermal stability of the $Al_{12}(Mn_{(1-x)}W_x)$ phase in comparison to the $Al_{12}Mn$ phase which forms in binary Al-Mn alloys is explained in terms of the Gibbs free energy of the two phases. It is shown that co-precipitating tungsten with aluminum and manganese lowers the Gibbs free energy of the precipitated phase and by so doing it slows down its coarsening rate and

* Corresponding author
Tel.: (508) 831-5647 Fax: (508) 831-5992 e-mail: mmm@wpi.edu

enhances its thermal stability.

1. INTRODUCTION

Manganese has a relatively high solubility in aluminum compared to other transition metals (maximum solubility of manganese in aluminum is about 1.2 wt.% [1, 2]), and it also has a relatively low diffusivity in aluminum ($D_{Mn} = 2.16\times10^{-6}$ m^2/s at 450°C [3]). For these reasons, it is envisioned that lightweight aluminum alloys may be developed for high temperature applications on the basis of the Al-Mn system wherein an appropriate heat treatment leads to precipitation of a strength-inducing Al-Mn phase. Aging homogenized Al-Mn alloys at a temperature between 400°C to 500°C may lead to formation of one or more different precipitate phases including an orthorhombic phase with the chemical formula Al_6Mn, a body-centered cubic phase with the chemical formula $Al_{12}Mn$ (usually referred to as G), a simple cubic phase (usually referred to as G')[6], and a hexagonal phase (usually referred to as G") [4]. Of these precipitate phases, Al_6Mn is the equilibrium one and the others are all meta-stable phases. The G phase in particular is an attractive strength-inducer. It is semi-coherent with its surrounding aluminum matrix [5], and it tends to form with a prism-like morphology that is approximately 500 nm in length [5]. Unfortunately, the G phase is meta-stable, and

[6] The G' phase is believed to have the chemical formula $Al_{12}Mn_3Si$, and so it is not observed in Al-Mn alloys except when silicon is present [].

when it is subjected to elevated temperature for an extended period of time, it tends to coarsen and transform to the equilibrium Al_6Mn phase [2, 5]. This transformation is invariably accompanied by significant loss of strength. It has been shown that in many instances, it is possible to stabilize binary Al_xTM_y (TM ≡ transition metal) precipitates by alloying into them other transition metals so that they form as ternary co-precipitates of the composition $Al_x(TM1_yTM2_{1-y})$ [6, 7]. Examples of phase stabilization by co-precipitation includes co-precipitating zirconium with scandium to form $Al_3(Sc_xZr_{1-x})$ [8-11], and introducing rare earth elements into Ni_3Al [12]. These '*precipitate stabilizing*' elements usually have very low diffusivity in aluminum and thus the co-precipitated particles tend to resist coarsening. It is believed that adding tungsten to binary Al-Mn alloys may stabilize the G phase relative to the Al_6Mn equilibrium phase by co-precipitating with manganese to form $Al_{12}(Mn_xW_{1-x})$ particles. Co-precipitation of tungsten and manganese is envisioned because both the $Al_{12}W$ and the $Al_{12}Mn$ phases have the same crystal structure (BCC) and their lattice parameter differs from one another by only 1.47% ($a_{Al_{12}Mn}$ = 0.747 nm and $a_{Al_{12}W}$ = 0.758nm [13]). In this publication, we report on the effects of adding tungsten to binary Al-Mn alloys by measuring the alloy's ambient temperature tensile properties and correlating these measurements to the alloy's microstructure and to the coarsening kinetics of the strength-inducing

$Al_3(Mn_xW_{1-x})$ precipitate particles.

2. MATERIALS AND PROCEDURES

Al-2Mn and Al-2Mn-0.8W alloys were constituted from pure aluminum ingots (99.99% purity), Al-25wt.% Mn master alloy, and pure, 325 mesh tungsten powder. The alloys were melted in an induction furnace in clean silicon carbide crucibles coated with boron nitride. The melts were degassed with high purity argon gas by means of a rotating impeller degasser for 30 minutes, and they were poured at approximately 850°C into a water-chilled copper mold. The water-chilled copper mold produces standard ASTM sub-size tensile specimens with a uniform cooling rate of about 120°C/s. The specimens were isothermally aged in an electric furnace and then they were cooled from the aging temperature to room temperature in ambient air. Although precipitation hardenable aluminum casting alloys are solution heat treated and quenched before they are artificially aged, the Al-2Mn and Al-2Mn-0.8W alloys of this study were aged without solutionizing and quenching. This deviation from the norm is dictated by the fact that these alloys are based on peritectic systems wherein a solutionizing heat treatment is not possible without causing incipient melting of the cast part. For these alloys, it is submitted that the liquid is homogenized during melting and the fast cooling rate during solidification replaces the quenching step and

preserves the homogeneous super saturated solid solution. As seen in Fig. 1, microstructure analysis shows that this statement is indeed true. Samples from both alloys were prepared for scanning electron microscopy (SEM) by polishing according to standard metallographic methods. Samples used for transmission electron microscopy (TEM) were produced by thinning foils of the alloys to perforation by means of a twinjet electro-polisher (Fischione Instruments, model 120) operating at 12 volts and utilizing a solution of 10 vol.% perchloric acid in methanol maintained at -20°C. A JOEL-7000F scanning electron microscope operating at 200 kV and a JOEL-2010F transmission electron microscope were used for microstructure analyses.

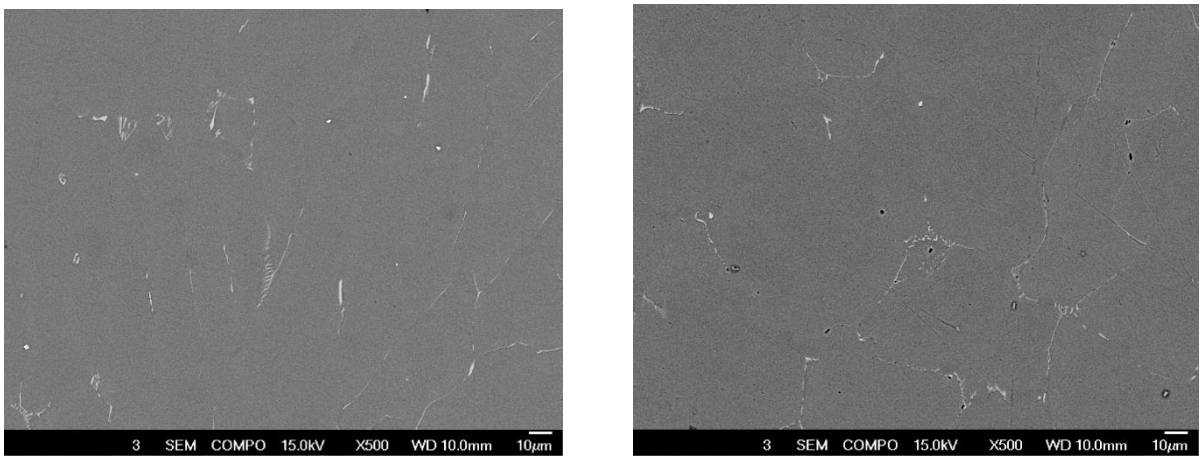

(a) (b)

Fig. 1 SEM photomicrographs of as-cast (a) Al-2Mn and (b) Al-2Mn-0.8W alloys.

Room temperature tensile properties of the alloys were measured by means of a Universal Testing machine (Instron model 5500R) at an

extension rate of 0.05 in/min. A 1-inch gage length extensometer (MTS model 634.25E-24) was used to measure extension. At least 3 specimens were used in each measurement and the results were averaged and the standard deviations were calculated. Fracture of all specimens took place within the gage length and specimens with severe porosity and/or oxides that would affect the results were excluded.

3. RESULTS

3.1 As-cast microstructure

Fig. 1 shows SEM photomicrographs of the as-cast Al-2Mn and Al-2Mn-0.8W alloys. Nearly all the manganese and tungsten are soulutionized in the α-Al matrix due to the high cooling rate during solidification. Only a small amount of manganese segregates to the grain boundary where it forms an Al-Mn compound as confirmed by Energy Dispersive Spectrometry (EDS).

3.2 Aging response of Al-2Mn and Al-2Mn-0.8W alloy

Fig. 2 shows the variation in measured yield strength of Al-2Mn and Al-2Mn-0.8W alloys with holding time at 450°C. The Al-2Mn alloy reaches its peak yield strength of 78 MPa after 4 hours and then its yield strength decreases quickly so that after 250 hours it drops by about 28% from its maximum value.

On the other hand, the measured yield strength of the Al-2Mn-0.8W alloy

reaches its maximum value of 76 MPa after 12 hours and stabilizes at this maximum value for the duration of the test (250 hours).

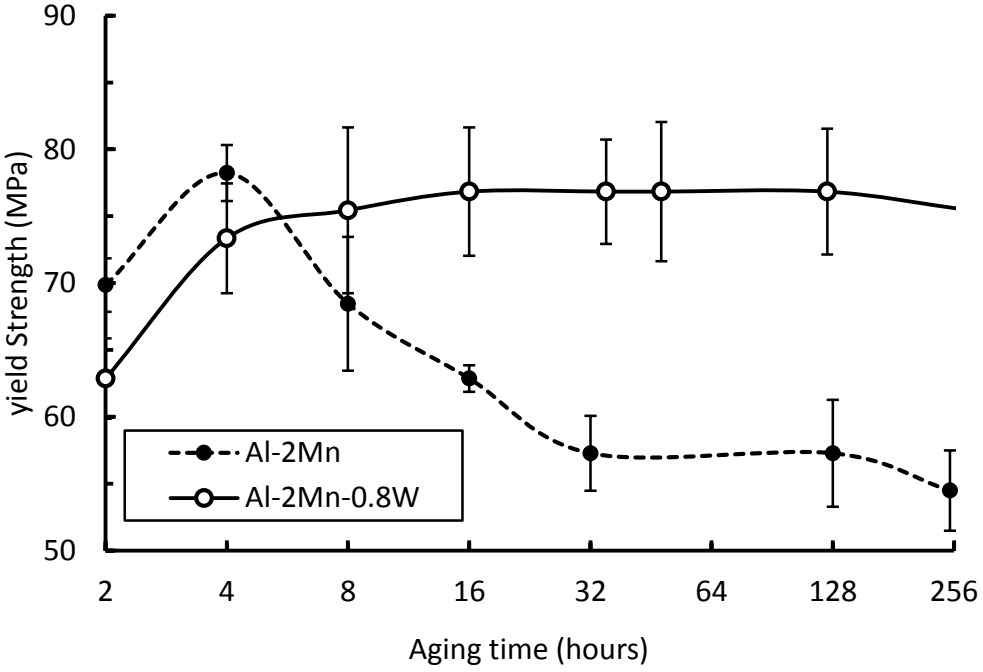

Fig. 2 Variation of measured yield strength of Al-2Mn and Al-2Mn-0.8W alloys with holding time at 450°C.

3.3 Microstructure of isothermally held (400°C) Al-2Mn and Al-2Mn-0.8W alloys

Fig. 3 shows typical TEM photomicrographs of Al-2Mn and Al-2Mn-0.8W alloy samples that were isothermally held at 400°C for 4 hours. The precipitates in both samples have the BCC crystal structure. Ens. [4] identified the precipitate in the Al-2Mn alloy as metastable $Al_{12}Mn$ and referred to it as G phase. He reported its lattice parameter to be 7.47 nm [13].

Fig.4 shows result of EDS line scan mapping performed on a typical Al-

2Mn-0.8W alloy sample that was isothermally held at 450°C for 4 hours. It was found that both the Mn and W element count increases in the precipitate particle relative to in the surrounding α-Al matrix, which suggests that Mn and W co-precipitate with aluminum forming $Al_3(Mn_xW_{1-x})$ precipitate.

Fig. 5 shows typical TEM photomicrographs of Al-2Mn and Al-2Mn-0.8W alloy samples that were isothermally held at 450°C for 128 hours. It is clear that after 128 hours at 450°C, the size of the precipitate particles is significantly increased in the Al-2Mn alloy compared with its size after 4 hours. On the other hand, the size of the precipitates particles in the Al-2Mn-0.8W alloy did not significantly. Moreover, and of equal importance, the precipitated phase in the Al-2Mn alloy transforms to the equilibrium Al_6Mn phase that has the orthorhombic crystal structure shown in the diffraction pattern inserted in Fig. 4(a).

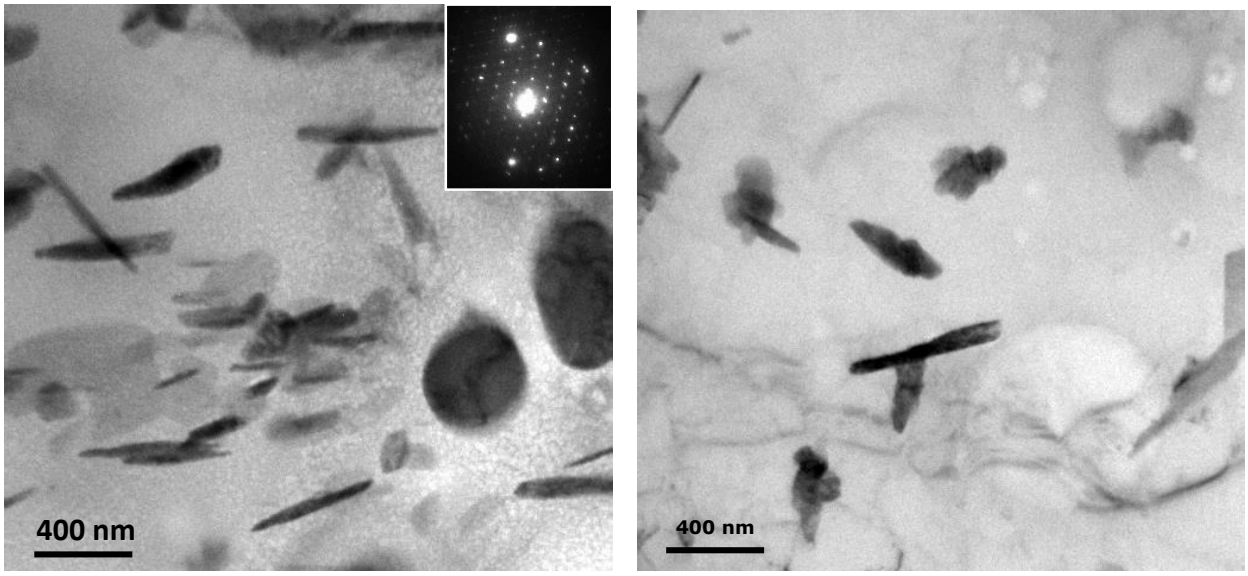

(a) (b)

Fig. 3 Typical TEM photomicrographs of (a) Al-2Mn alloy, and (b) Al-2Mn-0.8W alloy isothermally held at 400°C for 4 hours.

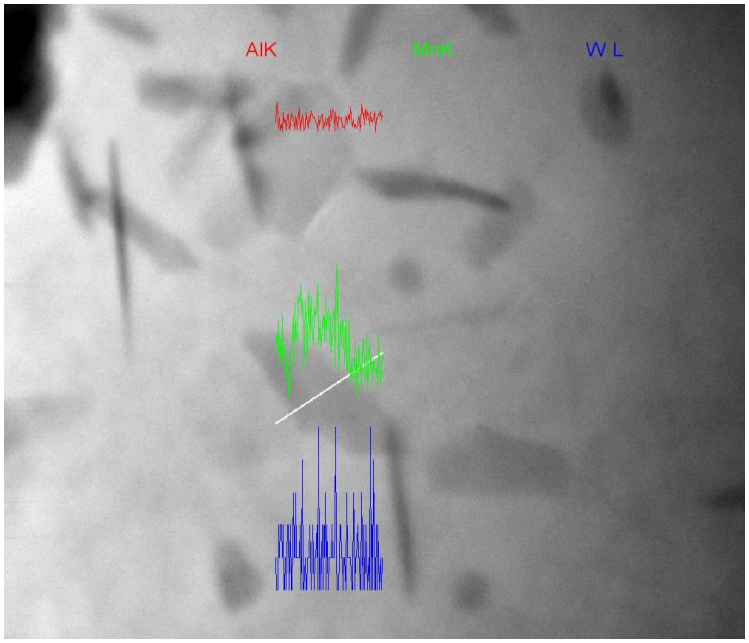

Fig. 4 EDS map on Al-2Mn-0.8W alloy which was isothermally held at 400°C for 4 hours.

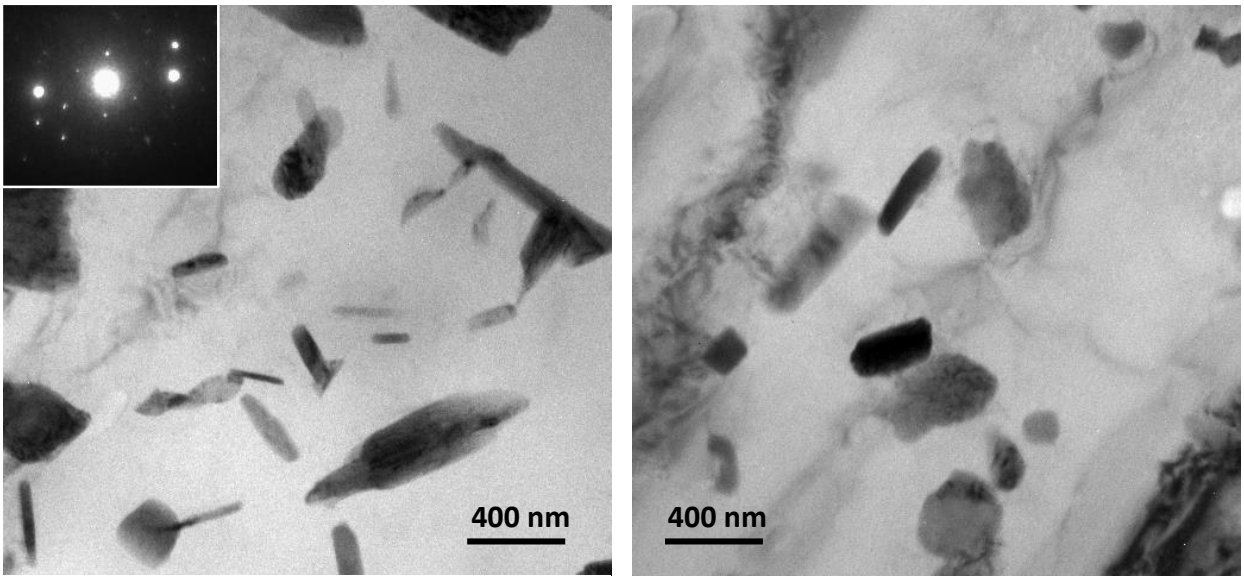

(a) (b)

Fig. 5 Typical TEM photomicrographs of (a) Al-2Mn alloy, and (b) Al-2Mn-0.8W alloy which were isothermally held at 450°C for 128 hours.

3.4 Thermal stability of precipitates in isothermally held (350°C) Al-2Mn and Al-2Mn-0.8W alloys

Typical Al-2Mn and Al-2Mn-0.8W alloy samples were aged at 450°C for 4 hours and then they were held at 350°C for up to 300 hours in order to investigate the thermal stability of the precipitates that form in both alloys. Figs. 6 and 7 show typical TEM photomicrographs of Al-2Mn and Al-2Mn-0.8W alloy samples that were isothermally held at 350°C for 100 hours and for 300 hours, respectively. It is clear from the Figs. that after both holding times, the precipitates in the Al-2Mn alloy become much larger than those in the Al-2Mn-0.8W alloy, and the size of the precipitates in the Al-2Mn alloy increases with the increased holding time. Moreover, the precipitate density of the Al-2Mn-0.8W alloy is

considerably higher than that of the Al-2Mn alloy.

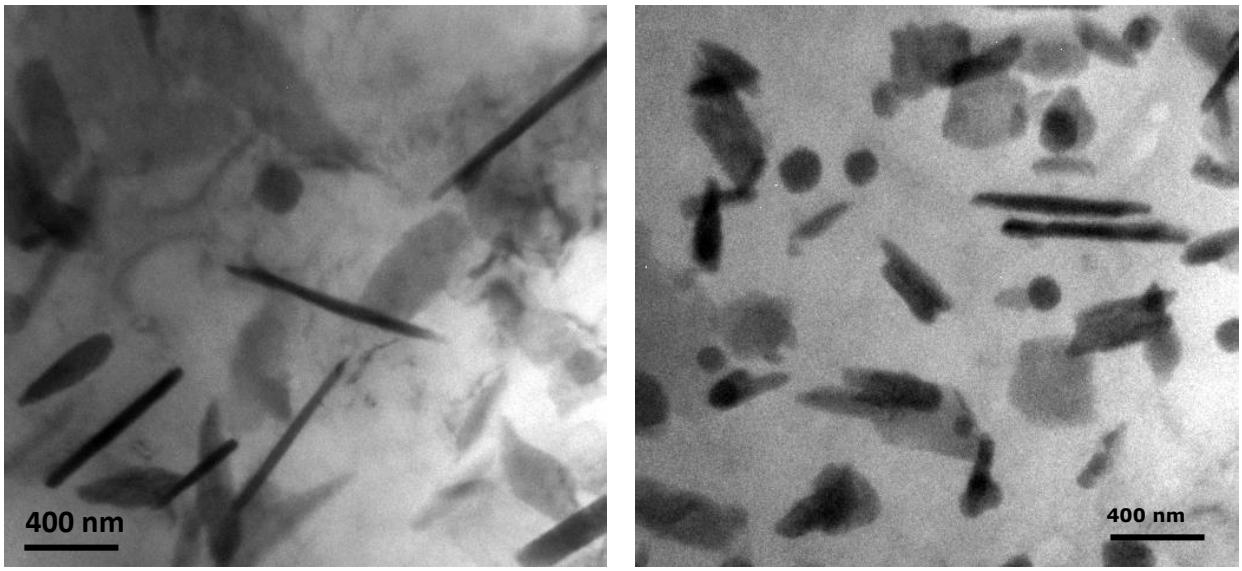

(a) (b)

Fig. 6 Typical TEM photomicrographs of (a) Al-2Mn alloy, and (b) Al-2Mn-0.8W alloy which were isothermally aged at 450°C and then isothermally held at 350°C for 100 hours.

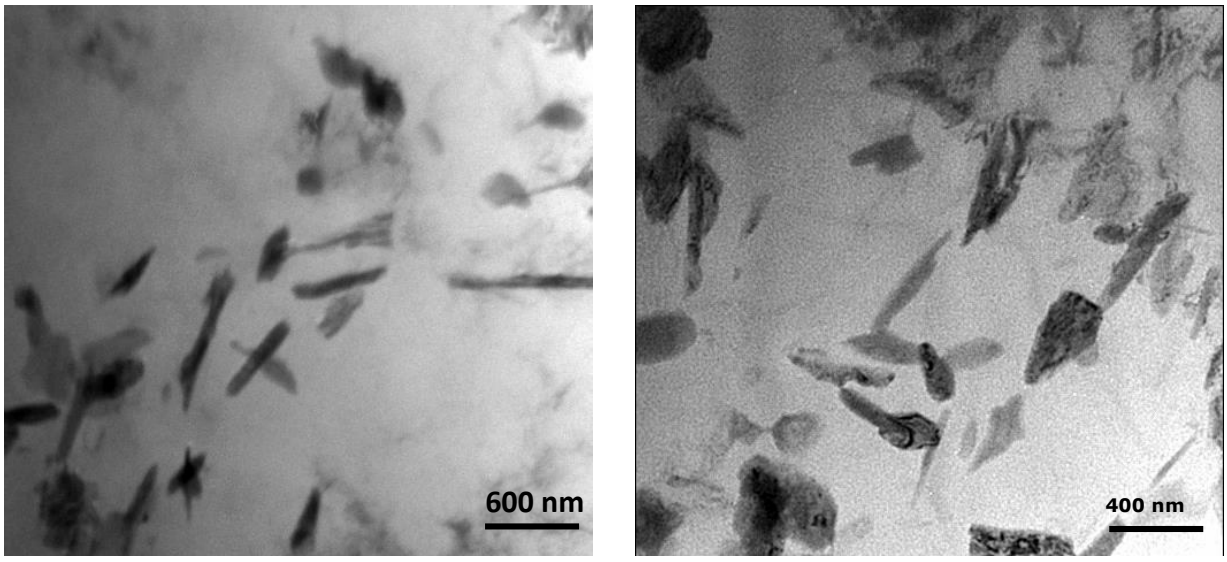

(a) (b)

Fig. 7 Typical TEM photomicrographs of (a) Al-2Mn alloy, and (b) Al-2Mn-0.8W alloy which were isothermally aged at 450°C and then isothermally held at 350°C for 300 hours.

Fig. 8 shows the variation in the average length of precipitate particles as function of holding time for the Al-2Mn and the Al-2Mn-0.8W alloys. More than 100 precipitate particles were measured to produce each data point. The average length of the precipitate particles in the Al-2Mn-0.8W alloy does not change significantly from its value in the as-aged condition, and remains constant at around 250 nm with holding time. On the other hand, the average length of the precipitate particles in the as-aged Al-2Mn alloy, which is equal to that of the as-aged Al-2Mn-0.8W alloy, rapidly increases and reaches 460 nm after 300 hours at 350°C. The coarsening rate of $Al_{12}Mn$ in Al-2Mn alloy is about 0.5 nm/hour. This result suggests that $Al_{12}(Mn_{(1-x)}W_x)$ precipitate is more stable than $Al_{12}Mn$ precipitate at 350℃.

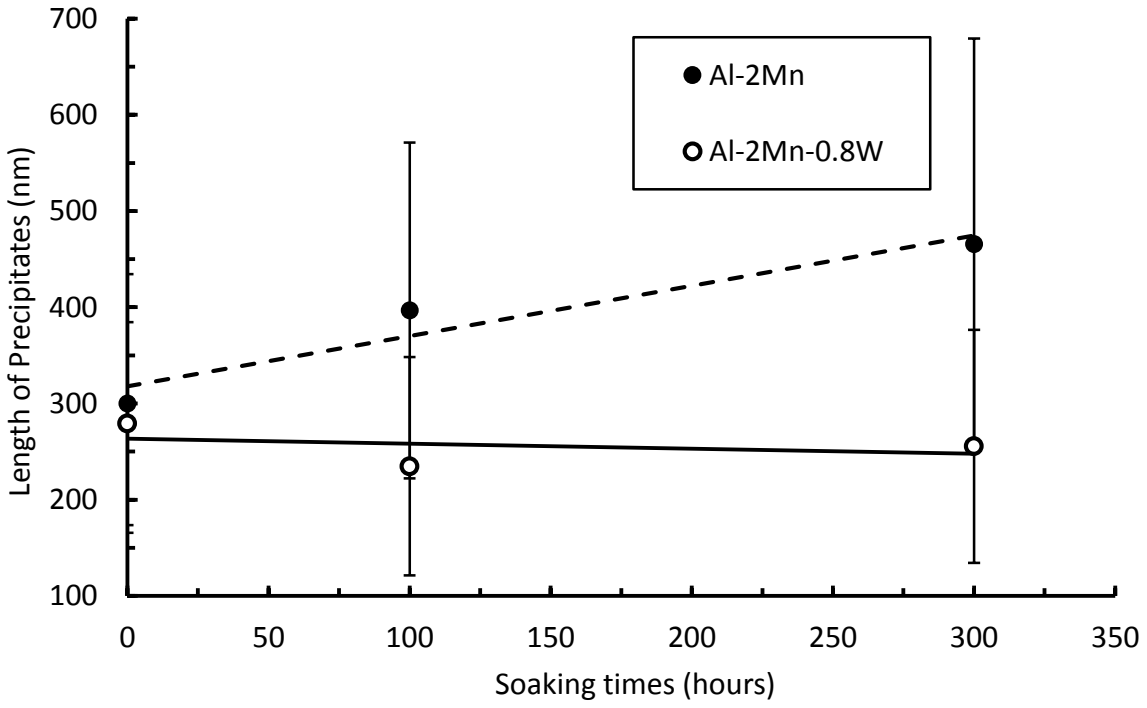

Fig. 8 Variation of the average length of the precipitate particles in the Al-2Mn and Al-2Mn-0.8W alloys with holding time at 350°C.

4. DISCUSSION

When precipitation strengthened aluminum alloys are subjected to high temperature, the metastable precipitates usually coarsen by the Gibbs-Thomason effect before they transform to the stable crystal structure and the alloy loses its strength. Therefore, precipitates that have a low coarsening rate have enhanced thermal stability; and alloys that employ such precipitates for strengthening have good tensile properties at high temperature. Lifchitz, Slyosov, and Wagner proposed equation (1) to describe the coarsening rate of precipitates [14]

$$\frac{d\bar{R}}{dt}=\frac{4}{27}\frac{X^i}{X^p-X^i}\frac{R_O D}{\bar{R}^2} \qquad (1)$$

In Eq. (1), $R_o=\frac{2\gamma v_{at}^P}{k_B T}$, and in the case of a stoichiometric binary precipitate of the general composition A_xB_y, R_o is multiplied by $\frac{(x+y)}{y}$.

When precipitates coarsen, the solute element(s) dissolve into the matrix alloy and diffuse from the smaller precipitate particles to the larger ones. Therefore, as Eq. (1) indicates, the coarsening rate is governed by the equilibrium solubility of the diffusing element(s) in the matrix, X^i, which can be determined from fundamental thermodynamic principles as follows.

As Fig. 9 shows, at equilibrium, the chemical potential of a given solute element is equal in both the matrix and the precipitate particle. Therefore, the concentration of the solute element in the matrix, X^i, can

be known once the Gibbs free energies of the matrix and the precipitate are known.

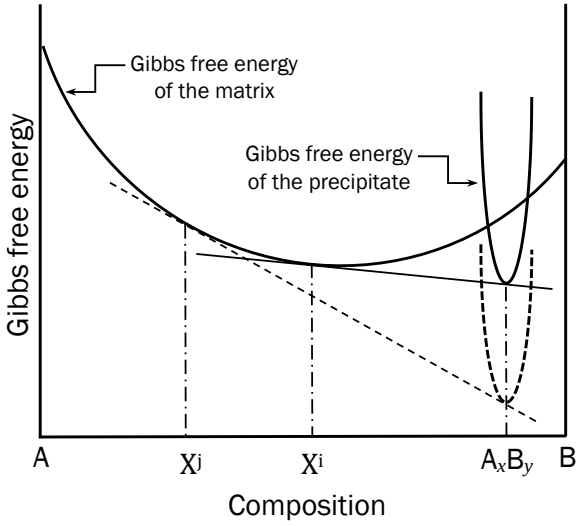

Fig. 9 Schematic diagram showing that by drawing a common tangent to the Gibbs free energy curves of the matrix and precipitate, it is possible to determine the equilibrium concentration of the solute element in the matrix at the matrix-precipitate interface; and by lowering the Gibbs free energy of formation of the precipitate (the dotted curve relative to the solid curve), it is possible to lower the amount of solute in the matrix from X^i to X^j.

The Regular Solution model [15] may be used to calculate the Gibbs free energy of the α-Al matrix in an aluminum alloy as shown in Eq. (2)

$$G_m = x_i^o G_i - TS_m^{ideal} + G_m^{ex} \quad (2)$$

The excess Gibbs free energy, G_m^{ex}, in a binary alloy may be expressed by

$$G_m^{ex} = X_A X_B [L^0 + L^1 (X_A - X_B)] \quad (3)$$

In this analysis, the precipitate is treated as a stoichiometric compound, and therefore it has a sharp Gibbs free energy curve as shown in Fig. 9.

The Gibbs free energy of the precipitate influences the concentration of the solute element in the matrix in the lower precipitate Gibbs free energy causes the concentration of the solute element in the matrix to shift towards the solute free regions, which effectively mitigates the coarsening process as suggested by Eq. (1). Alloying the precipitate is a possible means of decreasing its Gibbs free energy.

For an Al-Mn alloy, the major precipitate responsible for strengthening is the metastable $Al_{12}Mn$ particles that have the $Al_{12}W$ type crystal structure. Because the crystal structure of $Al_{12}Mn$ is similar to that of $Al_{12}W$, and because the lattice parameter of $Al_{12}Mn$ is close to that of $Al_{12}W$, W may be dissolved into $Al_{12}Mn$ to form Al_{12}(Mn,W) co-precipitates. The Gibbs free energies of formation of $Al_{12}Mn$ and $Al_{12}W$ in a one mole system are respectively [15],

$$\begin{aligned}\Delta G^{o}_{Al12Mn} = G^{o}_{Al12Mn} - 0.923H^{o}_{fcc-Al}(298.15\text{K}) \\ - 0.0769H^{o}_{fcc-Al}(298.15\text{K}) \\ = -9671.5 + 4.23\,\text{T} + 0.923\text{GHSER}_{\text{Al}} \\ + 0.0769\text{GHSER}_{\text{Mn}}\end{aligned} \qquad \text{(4-a)}$$

and

$$\Delta G^{o}_{Al12W} = G^{o}_{Al12W} - 0.923H^{o}_{fcc-Al}(298.15\text{K}) \quad (4\text{-b})$$
$$- 0.0769H^{o}_{fcc-Al}(298.15\text{K})$$
$$= -4800 + 0.73\text{T} + 0.923\text{GHSER}_{\text{Al}}$$
$$+ 0.0769\text{GHSER}_{\text{W}}$$

Where

$$\text{GHSER}_{\text{Al}} = -11276.2 + 223.027\text{T} \quad (5\text{-a})$$
$$- 38.58\text{TlnT} \quad (700\text{K} < T < 933\text{K})$$

$$\text{GHSER}_{\text{Al}} = -7976.15 + 137.09\text{T} \quad (5\text{-b})$$
$$- 24.37\text{TlnT} \quad (298\text{K} < T < 700\text{k})$$

$$\text{GHSER}_{\text{Mn}} = -8115.28 + 130.06\text{T} \quad (6\text{-a})$$
$$- 23.46\text{TlnT} \quad (298\text{K} < T < 1519\text{K})$$

$$\text{GFCC}_{\text{Mn}} = -3439.3 + 131.88\text{T} \quad (6\text{-b})$$
$$- 24.52\text{TlnT} \quad (298\text{K} < T < 1519K)$$

$$\text{GHSER}_{\text{W}} = -7646.31 + 130.4\text{T} \quad (6\text{-c})$$
$$- 24.1\text{TlnT} \quad (298\text{K} < T < 3695\text{K})$$

The sub-lattice model [15] may be used to calculate the Gibbs free energy of formation of the $Al_{12}(Mn_{(1-x)}W_x)$ compound as shown in Eq. (7)

$$\Delta G^{o}_{Al12Mn} = Y_W \Delta G^{o}_{Al12W} + (1 - Y_W)\ \Delta G^{o}_{Al12Mn} + G^{ex}_{m} + \text{RT}\,[Y_W ln Y_W + \quad (7)$$
$$(1 - Y_W)\ln(1 - Y_W)]$$

in which $Y_W = \frac{n_W}{n_W + n_{Mn}}$, $\Delta G^o_{Al12W} = \mathrm{GHSER_{Al}}$, and $\Delta G^o_{Al12Mn} = \mathrm{GFCC_{Mn}}$

Because data on the ternary Al-Mn-W alloy in the Al rich corner of the equilibrium diagram is lacking, it is not possible at this time to calculate the excess Gibbs free energy of the $Al_{12}(Mn_{(1-x)}W_x)$ compound. Instead, and as a reasonable approximation, we assume the excess Gibbs free energy of the $Al_{12}(Mn_{(1-x)}W_x)$ compound to be negligibly small; i.e., we assume that $Al_{12}Mn$ and $Al_{12}W$ are ideal. With this assumption, the Gibbs free energy of formation of $Al_{12}(Mn_xW_{(1-x)})$ is calculated for different temperatures and plotted in Fig. 10. As Figs. 10 (a) show dissolution of 40 atom pct. W or 60 atom pct. Mo in the $Al_{12}Mn$ phase lowers the Gibbs free energy of the Al_{12}(Mn,W) precipitates to their possible minimum. The Gibbs free energy of formation of the Al_{12}(Mn,W) and precipitates in an Al-2wt.%Mn-0.8wt.%W alloy at different temperatures is plotted in Fig. 10 (b). The discontinuity in the curves of Fig. 10 (b) is due to the fact that the heat capacity of Al is not continuous at 700K.

Because the solubility of W and Mo in α-Al is negligibly small, the α-Al matrix may be treated as a regular binary solution of Mn in Al; and therefore,

$$\Delta G_m^{fcc} = X_{Mn}\Delta G^o_{Mn} + (1 - X_{Mn})\Delta G^o_{Al} + RT[X_{Mn} ln X_{Mn} + (1 - X_{Mn}) \ln(1 - X_{Mn})] + G_m^{ex} \quad (8\text{-a})$$

Where

$$G_m^{ex} = X_{Mn}(1 - X_{Mn})[L^0 + L^1(1 - 2X_{Mn})] \quad (8\text{-b})$$

$$L^0 = -69300 + 25.0T \quad \text{(8-c)}$$

$$L^1 = 8800 \quad \text{(8-c)}$$

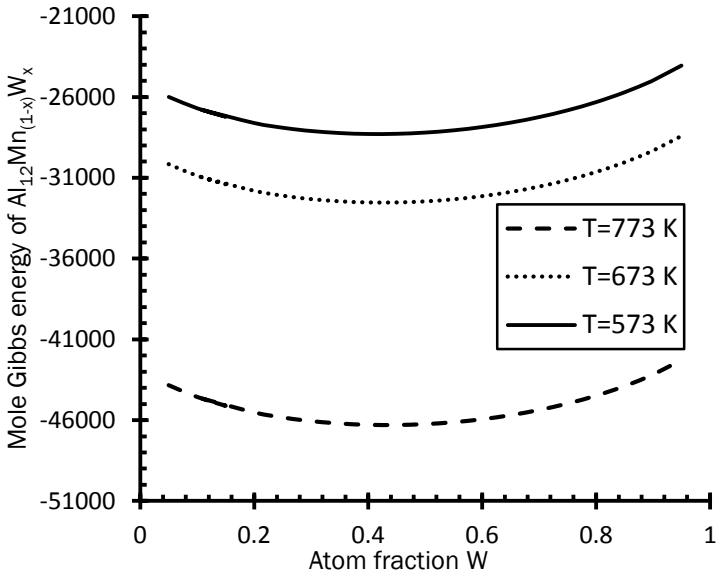

(a)

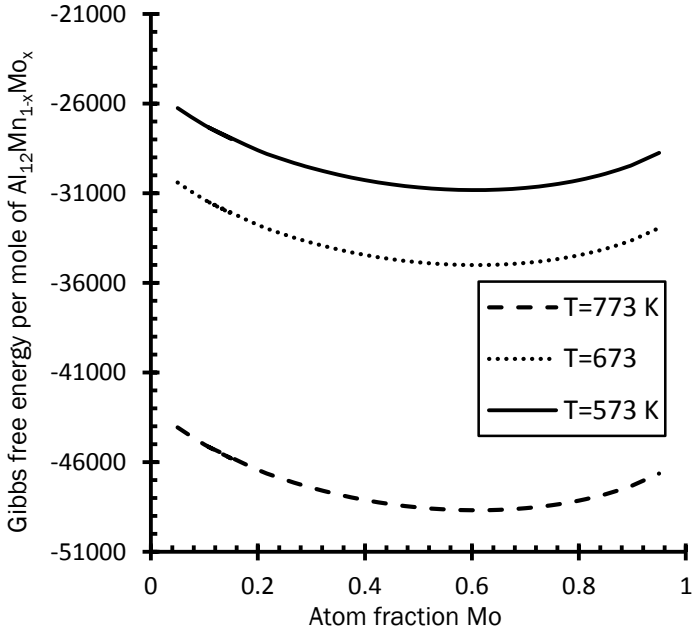

(b)

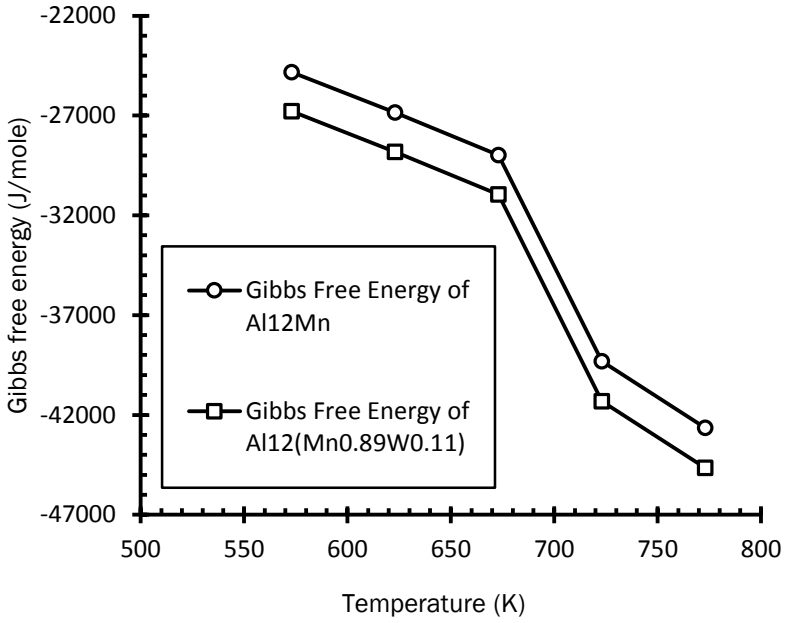

(c)

Fig. 10 Calculated Gibbs free energy of Al-Mn-W and Al-Mn-Mo alloys as function of (a) the amount of W and Mo in the $Al_{12}Mn$ phase at various temperatures. (b) The Gibbs free energy of formation of the $Al_{12}(Mn,W)$) precipitates in Al-2wt.%Mn-0.8wt.%W and Al-2wt.%Mn alloys as function of temperature.

Because the chemical potential of Mn must be equal in both the α-Al matrix and the precipitate, let

$$\frac{d\Delta G_m^{fcc}}{dX_{Mn}} = \frac{\Delta G^o_{Al_{12}Mn} - \Delta G_m^{fcc}}{0.0796 - X_{Mn}} \qquad (9)$$

Eq. (9) allows solving for X_{Mn}, which is plotted for different temperatures in Fig. 11(a). Fig. 11(b) shows the coarsening rate of Al-2wt.%Mn-0.8wt%W normalized relative to the coarsening rate of Al-2wt.%Mn. At 400°C, the coarsening rate of Al-2wt%Mn-0.8wt.%W is only 1% that of Al-2wt%Mn.

It is worth noting that the calculated equilibrium concentration of Mn in

the α-Al matrix of a binary Al-Mn alloy is very close to values found in the open literature [2].

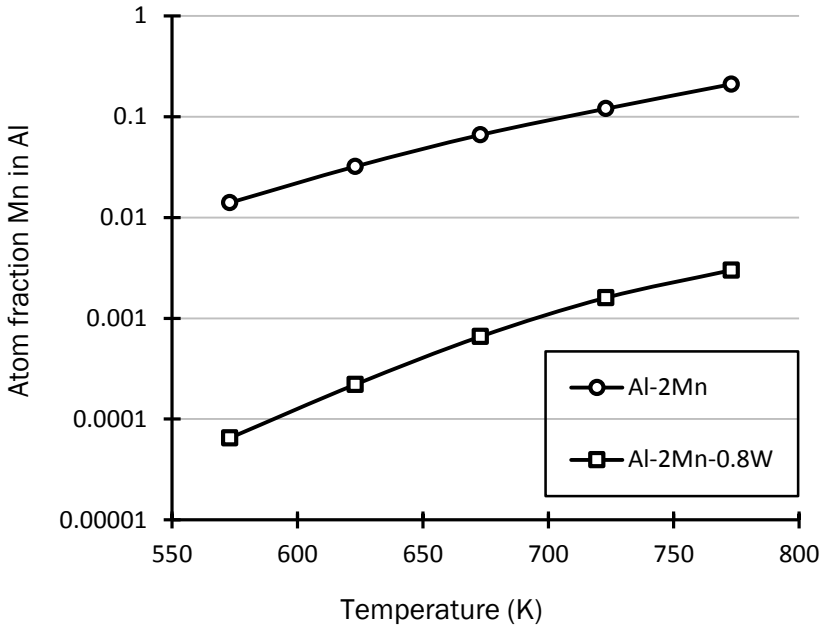

(a)

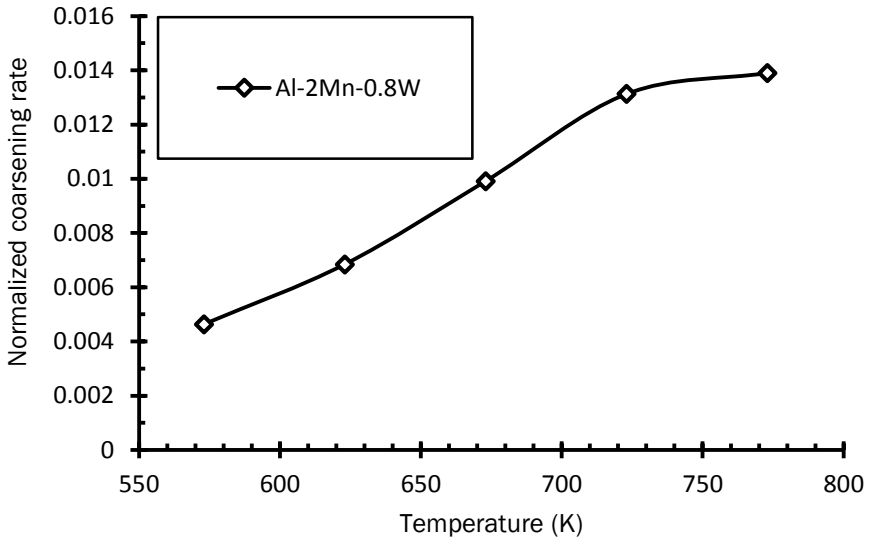

(b)

Fig. 11 (a) The Gibbs free energy of formation of Al-2wt%Mn at all temperatures is significantly decreased by adding W. (b) The normalized coarsening rate of Al-2wt.%Mn-0.8wt%W (normalized relative to the coarsening rate of Al-2wt.%Mn).

5. CONCLUSIONS

(1) Adding small amounts (< 1 wt. %) tungsten to binary Al-Mn alloys causes co-precipitation of aluminum, manganese, and tungsten and formation of the meta-stable $Al_{12}(Mn_{(1-x)}W_x)$ precipitate.

(2) The meta-stable $Al_{12}(Mn_{(1-x)}W_x)$ precipitate is thermally stable and will not coarsen when held at 350°C for extended periods of time (at least up to 250 hours, which was the test duration). This is in contrast to the $Al_{12}Mn$ precipitate, which coarsens when held at 350°C at a rate of 0.5nm/hour.

(3) The enhanced thermal stability of the $Al_{12}(Mn_{(1-x)}W_x)$ phase in comparison to the $Al_{12}Mn$ phase is explained in terms of the Gibbs free energy of the two phases. Co-precipitating tungsten with aluminum and manganese lowers the Gibbs free energy of the precipitated phase and by so doing it increases its thermal stability.

(4) While measurements were not performed with molybdenum, theoretical calculations similar to those performed with tungsten suggest that molybdenum may have a similar stabilizing effect on the $Al_{12}Mn$ phase to that caused by tungsten.

(5) It is envisioned that lightweight aluminum alloys may be developed for high temperature applications on the basis of the Al-Mn-W system wherein aging the alloy at 450°C for 8 hours leads to precipitation of

a thermally stable strength-inducing $Al_{12}(Mn_{(1-x)}W_x)$ phase.

6. REFERENCE

1. Murray, J., et al., *Stable and metastable phase equilibria in the Al-Mn system*. Metallurgical Transactions A, 1987. **18**(3): p. 385-392.
2. Liu, X., et al., *Thermodynamic assessment of the Aluminum-Manganese (Al-Mn) binary phase diagram*. Journal of phase equilibria, 1999. **20**(1): p. 45-56.
3. Rummel, G., et al., *Diffusion of implanted 3d-transition elements in aluminium. I: Temperature dependence*. Zeitschrift für Metallkunde, 1995. **86**(2): p. 122-130.
4. Nes, E., S. Naess, and R. Hoier, *Decomposition of an Aluminum-Manganese Alloy*. Zeitschrift fur Metallkunde, 1972. **63**(5): p. 248-252.
5. D. SHECHTMAN, R.J.S., and E S. BIANCANIELLO, *Precipitation in Rapidly Solidified AI-Mn Alloys*. METALLURGICAL TRANSACTIONS A, 1984. **15A**: p. 1987-1997.
6. Lefebvre, W., et al., *Precipitation kinetic of Al3(Sc,Zr) dispersoids in aluminium*. Journal of Alloys and Compounds, 2009. **470**(1-2): p. 107-110.

7. Zedalis, M. and M. Fine, *Precipitation and ostwald ripening in dilute AI Base-Zr-V alloys*. Metallurgical Transactions A, 1986. **17**(12): p. 2187-2198.

8. Forbord, B., et al., *Three dimensional atom probe investigation on the formation of Al3(Sc,Zr)-dispersoids in aluminium alloys*. Scripta Materialia, 2004. **51**(4): p. 333-337.

9. Fuller, C., J. Murray, and D. Seidman, *Temporal evolution of the nanostructure of Al(Sc,Zr) alloys: Part I – Chemical compositions of Al(ScZr) precipitates*. Acta Materialia, 2005. **53**(20): p. 5401-5413.

10. Fuller, C. and D. Seidman, *Temporal evolution of the nanostructure of Al(Sc,Zr) alloys: Part II-coarsening of Al(ScZr) precipitates*. Acta Materialia, 2005. **53**(20): p. 5415-5428.

11. Fuller, C.B., D.N. Seidman, and D.C. Dunand, *Mechanical properties of Al(Sc,Zr) alloys at ambient and elevated temperatures*. Acta Materialia, 2003. **51**(16): p. 4803-4814.

12. Povarova, K., et al., *Influence of rare-earth metals on the high-temperature strength of Ni3Al-based alloys*. Russian Metallurgy (Metally), 2011. **2011**(1): p. 47-54.

13. Pearson, W.B., *A handbook of lattice spacings and structures of metals and alloys*. 1967.

14. Perez, M., M. Dumont, and D. Acevedo-Reyes, *Implementation of classical nucleation and growth theories for precipitation.* Acta Materialia, 2008. **56**(9): p. 2119-2132.

15. Ansara, I., A. Dinsdale, and M. Rand, *COST 507 Definition of Thermochemical and Thermophysical Properties to Provide a Database for the Development of New Light Alloys: Thermochemical Database for Light Metal Alloys*. 1998: Office for Official Publications of the European Communities.